A New Experiment Run Group Proposal Submitted to Jefferson Lab PAC44

A Search for Hybrid Baryons in Hall B with CLAS12

Volker Burkert *(Spokesperson)*, Daniel S. Carman *(Spokesperson)*, Valery Kubarovsky, Victor Mokeev *(Spokesperson)*, Maurizio Ungaro, Veronique Ziegler
Thomas Jefferson National Accelerator Facility, Newport News, Virginia 23606, USA

Annalisa D'Angelo *(Contact Person, Spokesperson)*, Lucilla Lanza, Alessandro Rizzo
Università di Roma Tor Vergata and INFN Roma Tor Vergata, 00133 Rome, Italy

Gleb Fedotov, Boris Ishkhanov, Evgeny Isupov, Evgeny Golovach *(Spokesperson)*
Skobeltsyn Institute of Physics, Moscow State University, 119234 Moscow, Russia

Ralf W. Gothe *(Spokesperson)*, Iuliia Skorodumina
University of South Carolina, Columbia, South Carolina 29208, USA

Vincent Mathieu[†], Vladyslav Pauk, Alessandro Pilloni, Adam Szczepaniak[†]
Theory Center, Jefferson Laboratory, Newport News, Virginia 23606, USA
([†]*Joint with Indiana University, Bloomington, Indiana 47405, USA*)

Simon Capstick, Volker Crede
Florida State University, Tallahassee, Florida 32306, USA

Jan Ryckebusch
Ghent University, B-9000 Ghent, Belgium

Michael Döring
The George Washington University, Washington, DC 20052, USA

Philip Cole
Idaho State University, Pocatello, Idaho 83209, USA

Vincenzo Bellini, Francesco Mammoliti, Giuseppe Russo, Concetta Sutera, Francesco Tortorici
INFN, Sezione di Catania, 95125 Catania, Italy

Ilaria Balossino, Luca Barion, Giuseppe Ciullo, Marco Contalbrigo, Paola Lenisa, Aram Movsisyan, Luciano Pappalardo, Mateo Turisini
INFN, Sezione di Ferrara, 44100 Ferrara, Italy

Marco Battaglieri, Andrea Celentano, Raffaella De Vita, Erica Fanchini, Mikhail Osipenko, Marco Ripani, Elena Santopinto, Mauro Taiuti
INFN, Sezione di Genova, 16146 Genova, Italy

Alessandra Filippi
INFN, Sezione di Torino, 10125 Torino, Italy

César Fernández-Ramírez
Universidad Nacional Autónoma de México, 04510 Mexico City, Mexico

Inna Aznauryan
Yerevan Physics Institute, 375036 Yerevan, Armenia

and the CLAS Collaboration

Abstract

This proposal aims to establish a program to search for new excited baryon states in the mass range from 1.8 GeV to 3 GeV, as well as to explore for the first time the behavior of resonance electrocouplings over the full spectrum of excited proton states at photon virtualities Q^2 approaching the photon point ($Q^2 < 0.2$ GeV^2). This work focuses on measuring $K^+\Lambda$, $K^+\Sigma^0$, and $\pi^+\pi^- p$ exclusive final states in CLAS12 and detecting the scattered electrons in the angular range from 2.5° to 35° using the electron detection capabilities of the Forward Tagger and the CLAS12 detector. The experiment will use longitudinally polarized electron beams of 6.6 GeV and 8.8 GeV to cover the range of invariant mass W up to 3 GeV and Q^2 from 0.05 GeV^2 to 2 GeV^2. The experiment requests 100 days of new beam time, 50 days at 6.6 GeV and 50 days 8.8 GeV. The main aspects of this proposal are to:

- search for new hybrid baryon states with the glue as an extra constituent beyond the three constituent quarks by focusing on measurements at $Q^2 < 1.0$ GeV^2 where the expected magnitudes of the hybrid electroexcitation amplitudes are maximal;

- search for three-quark "missing" resonances in the electroproduction of different hadronic final states with the highest fluxes of virtual photons ever achieved in exclusive meson electroproduction experiments;

- study the structure of prominent nucleon resonances in the mass range up to 3 GeV in the regime of large meson-baryon cloud contributions and explore the N^* longitudinal electroexcitation approaching the photon point.

Exclusive events from KY and $\pi^+\pi^- p$ final states will be selected and the unpolarized differential cross sections will be obtained, complemented by measurements of the differential transverse-transverse and transverse-longitudinal interference cross sections, as well as induced and recoil hyperon polarizations. From these data the $\gamma_v p N^*$ electrocouplings will be determined for all possible new states with I=1/2 and I=3/2 and with all possible J^P quantum numbers, and the Q^2 evolution of their helicity amplitudes will then be determined in the low Q^2 range ($Q^2 < 2$ GeV^2) for the different reaction channels.

The hybrid baryons will be identified as additional states in the N^* spectrum beyond the regular three-quark states. Since spin-parities of hybrid baryons are expected to be the same as those for regular three-quark states, the hybrid-baryon signature will emerge from the distinctively different low Q^2-evolution of its electrocouplings, due to the additional gluonic component in their wave function.

This kinematic range also corresponds to the region of the largest contributions from the meson-baryon cloud, allowing us to improve our knowledge on this component, which is relevant to understand the structure of all N^* states studied so far, as well as to explore the longitudinal N^* electroexcitations as the photon virtuality goes to zero. This program adds an important new physics component to the existing CLAS12 N^* program at 11 GeV, which aims to measure the transition form factors for all prominent N^* states up to $Q^2 < 12$ GeV^2, the highest photon virtualities ever probed in exclusive reactions. The study of the spectrum and structure of excited nucleon states at distance scales from low to high Q^2, encompassing the regime where low-energy meson-baryon degrees of freedom dominate to the regime where quark degrees of freedom dominate, creates new opportunities to better understand how the strong interaction of dressed quarks and gluons gives rise to the spectrum and structure of excited nucleon states and how these states emerge from QCD.

Contents

1 Introduction

The ongoing program at Jefferson Lab and several other laboratories to study excitation of nucleons in the so-called nucleon resonance region with real-photon and electron beams has been very successful. Although only a fraction of the photoproduction data taken during the CLAS g8, g9, g11, and g12 run groups has yet been analyzed and published, the available data have allowed for very significant advances in light-quark baryon spectroscopy, and have led to strong evidence for several new nucleon excitations as documented in the PDG review of 2014 [1]. These discoveries were possible due to the very high meson production rates recently obtained for energy-tagged photoproduction processes. Furthermore, the use of meson electroproduction has led to completely new insights into the nature of several prominent baryon resonances, such as the $N(1440)\frac{1}{2}^+$ Roper resonance. For a long time this state defied an explanation of its properties, such as its mass, transition amplitudes, and transition form factors, within the constituent quark model (CQM). The analyses of the new electroproduction data from CLAS were crucial in dissecting its complex structure and providing a qualitative and quantitative explanation of the space-time evolution of the state [2]. The Roper was also considered as a candidate for the lowest mass hybrid baryon [3]. It was only due to the meson electroproduction data that this possibility could be dismissed [4, 5].

The theory of the strong interaction, QCD, not only allows for the existence of baryons with dominant gluonic contributions (hybrid baryons), but Lattice QCD calculations have now also predicted several baryon states with a dominant gluonic admixture to the wave function, and with the lowest mass hybrids approximately 1.3 GeV above the nucleon ground state [6], i.e. in the range of $W = 2.2$ GeV to 2.5 GeV. In the meson sector, exotic states (hybrid mesons) are predicted with quantum numbers that cannot be obtained in a pure $q\bar{q}$ configuration. The selection of mesons with such exotic quantum numbers provides a convenient way to identify candidates for gluonic mesons. In contrast to the meson sector, hybrid baryons have quantum numbers that are also populated by ordinary three-quark states. Hybrid baryons hence mix with these three-quark excited states or with dynamically generated states making the identification of gluonic baryons more difficult. An important question immediately arises, how we can distinguish gluonic excitations of baryons from their ordinary quark excitations?

Mapping out the nucleon spectrum and the excitation strengths of individual resonances is a powerful way to answer a central question of hadron physics: "What are the effective degrees of freedom as the excited states are probed at different distance scales?". Previous analyses of meson electroproduction have shown to be most effective in providing answers for several excited states including: $\Delta(1232)\frac{3}{2}^+$, $N(1440)\frac{1}{2}^+$, $N(1520)\frac{3}{2}^-$, $N(1535)\frac{1}{2}^-$, $\Delta(1620)\frac{1}{2}^-$, $N(1680)\frac{5}{2}^+$, $N(1675)\frac{5}{2}^-$, and $N(1710)\frac{1}{2}^+$ [7, 8, 9, 10].

The experimental program outlined in this proposal is meant to vastly improve upon the available information and to extend the reach of meson electroproduction to cover the nucleon resonance mass range up to 3 GeV and an extended low Q^2 range from 0.05 GeV^2 to 2 GeV^2, using electron beam energies of 6.6 GeV and 8.8 GeV. The unpolarized differential cross sections will be measured for the K^+Y and $\pi^+\pi^-p$ exclusive channels, complemented by measurements of the differential transverse-transverse and transverse-longitudinal interference cross sections, along with other polarization observables.

From these data the $\gamma_v pN^*$ electrocouplings will be determined employing the well known unitary isobar models and dispersion relation approaches that have proven very effective for the study of two-body final states such as πN [4, 11] and KY [12], as well as the JLab-Moscow (JM) meson-baryon reaction model for $\pi^+\pi^- p$ electroproduction [11, 13], the multi-channel partial wave techniques employing either the Bonn-Gatchina [14] or GWU [15] approaches, and approaches starting from the Veneziano model and Regge phenomenology [16] that are applicable at higher energies, where many hadron channels open in the final state interactions.

The proposed experimental program will search for all possible new states with isospin I=1/2 and I=3/2 and with all possible J^P quantum numbers. As new states are identified using the high event rates at very small Q^2 values ("quasi-real" photoproduction), the Q^2 dependence of their helicity amplitudes will be determined. The results at different values of Q^2 in the different exclusive channels will substantially enhance the discovery potential for new baryon states. Consistent results on the resonance masses and the $\gamma_v pN^*$ electrocouplings from the different exclusive decay channels, as well as Q^2-independent partial hadronic decay widths over the full Q^2 range, will offer convincing evidence for the existence of new states and the reliable extraction of their parameters. This approach has been highly effective in determining the Q^2 dependence of the $A_{1/2}$, $A_{3/2}$, and $S_{1/2}$ helicity amplitudes for several lower mass baryons, such as the $\Delta(1232)\frac{3}{2}^+$, $N(1440)\frac{1}{2}^+$, and $N(1535)\frac{1}{2}^-$ [4, 7]. These and many other results are included in the review of the N^* and Δ^* states in the latest edition of the PDG [17].

The hybrid baryons will be identified as additional states in the N^* spectrum beyond the regular three-quark states as has been predicted in recent LQCD studies of the baryon spectrum [6]. Since spin-parities of hybrid baryons are expected to be the same as those for regular three-quark states, information on the $\gamma_v pN^*$ electrocoupling evolution with Q^2 becomes critical in the search for hybrid baryons. A distinctively different Q^2 evolution of the hybrid-baryon electrocouplings is expected considering the different color-multiplet assignments for the quark-core in a regular versus a hybrid baryon, i.e. color singlet versus octet, which also calls for low photon virtualities as the preferential regime for studies of the hybrid-baryon electrocouplings. In conjunction with experiment E12-09-003 [18], which focuses on the highest Q^2, as well as E12-06-108A [19], which explores KY production, the proposed experiment will complement the existing program of nucleon resonance electroexcitation.

2 Theoretical Studies of Hybrid Baryons

2.1 Model Projections

In an extension of the MIT bag model, gluonic excitations of the nucleon, to states where a constituent gluon in the lowest energy transverse electric mode combines with three quarks in a color octet state to form a colorless state in the mass range of 1.600 ± 0.100 GeV, have been broadly discussed since 1983 [3].

The gluon flux-tube model applied to hybrid baryons [20, 21] came up with similar quantum numbers of the hybrid states, but predicted considerably higher masses than the bag model. For the lowest mass flux-tube hybrid baryon a mass of 1.870 ± 0.100 GeV was found. In all cases the lowest mass hybrid baryon was predicted as a $J^P = 1/2^+$

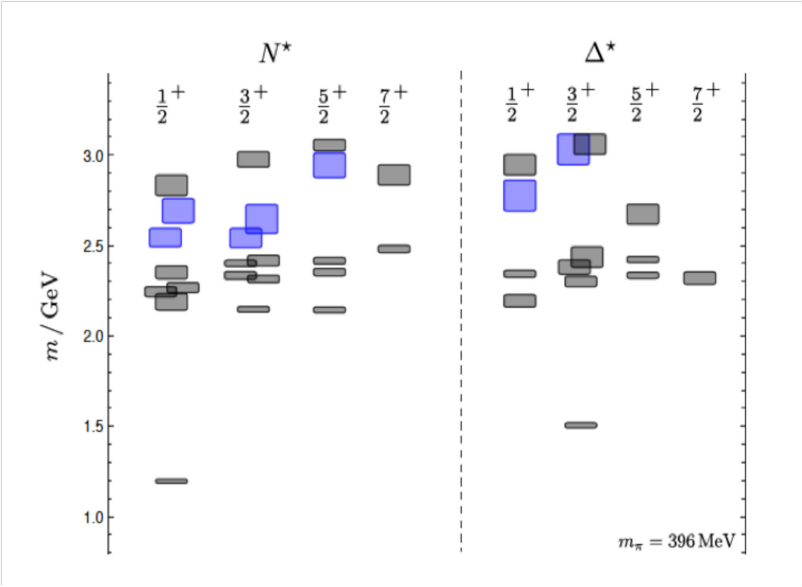

Figure 1: The light-quark baryon spectrum predicted in Lattice QCD at a pion mass of 396 MeV [6]. The blue shaded boxes indicate states with dominant gluonic contributions. Note that both the mass of the nucleon ground state and of the $\Delta(1232)$ are shifted by nearly 300 MeV to higher masses.

state, i.e. a nucleon- or Roper-like state. Hybrid baryons were also discussed in the large N_c approximation of QCD for heavy quarks [22], which also led to the justification of the constituent glue picture used in the models. The high energy behavior of hybrid baryons was discussed in Ref. [23]. However, in contrast to hybrid meson production, which has received great attention both in theory and in experiments, the perceived difficulties of isolating hybrid baryon states from ordinary quark states led this part of the field to remain dormant for several years.

2.2 Lattice QCD Predictions

The first quenched calculations on the lattice came in 2003 [24], when the lowest gluonic three-quark hybrid system was projected at a mass of 1 GeV above the nucleon mass, placing the lowest hybrid baryon at a mass of ∼2 GeV. The first LQCD calculation of the full light-quark baryon spectrum with unquenched quarks that occurred in 2012 included the projections of the hybrid isospin-1/2 N_G states and isospin-3/2 Δ_G states [6]. Fig. 1 shows the projected light quark baryon spectrum in the lower mass range.

At the pion mass of 396 MeV used in this projection, the prediction for the nucleon mass is shifted by nearly 300 MeV to higher masses. In the following we take this shift into account by subtracting 300 MeV from the masses of the excited states shown in Fig. 1. As stated in Ref. [6], the lowest hybrid baryons, shown in Fig. 1 in blue, were identified as states with leading gluonic contributions. If hybrid baryons are not too wide, we might expect the lowest hybrid baryon to occur at masses of about 1.3 GeV above the ground state, i.e. in a mass range of 2.2 GeV to 2.5 GeV, and a few hundred MeV above the band of radially excited $J^P = \frac{1}{2}^+$ three-quark nucleon excitations of isospin 1/2, and thus possibly well separated

from other states.

In this computation the lowest $J^P = \frac{3}{2}^+$ gluonic states are nearly mass degenerate with the corresponding $J^P = \frac{1}{2}^+$ gluonic states, generating a glue-rich mass range of hybrid nucleons. If these projections hold up with LQCD calculations using near physical pion masses, one should expect a band of the lowest mass hybrid baryon states with spin-parity $\frac{1}{2}^+$ and $\frac{3}{2}^+$ to populate a relatively narrow mass band of 2.2 GeV to 2.5 GeV. Note, that these states fall into a mass range where no three-quark nucleon excitations are predicted to exist in these calculations. The corresponding negative parity hybrid states, which are expected to occur at much higher masses, are not included in Fig. 1, and are not further considered here. However, they may be the subject of analysis should they appear within the kinematic range covered by this proposal.

2.3 Hadronic Couplings

Very little is known about possible hadronic couplings of hybrid baryons B_G. One might expect an important role for final states with significant gluonic admixtures, e.g. $B_G \to N\eta'$ [25], or final states containing $s\bar{s}$ contributions due to the coupling $G \to s\bar{s}$, e.g. $B_G \to K^+\Lambda$, $B_G \to N^*(1535)\pi \to N\eta\pi$, $B_G \to N\pi\pi$, $B_G \to \phi(1020)N$, and $B_G \to K^*\Lambda$. Quark-model estimates of the hadronic couplings would be helpful in selecting the most promising final states for the experimental evaluation. As long as such estimates are not available we will use a range of assumptions on the hadronic couplings to estimate the sensitivity required for definitive measurements. Assuming hadronic couplings of a few percent in the less complex final states, e.g. $K^+\Lambda$, $K^*\Lambda$, or $N\pi\pi$, we should be able to identify these states and proceed to experimentally establish their electromagnetic couplings and Q^2 dependences. We focus in this proposal on measurements of those decay channels that have already been successfully analyzed from CLAS data and that will be further investigated in data from CLAS12, i.e. $K^+\Lambda$, $K^+\Sigma^0$ and $\pi^+\pi^-p$. These studies can be extended by the exploration of other electroproduction channels such as $\phi(1020)N$ or $K^*\Lambda$.

2.4 Electromagnetic Couplings

The study of excited nucleon state electrocouplings in a wide range of photon virtualities is a proven effective tool for establishing the active degrees of freedom that contribute to the N^* structure at different distance scales [4, 7, 26, 27, 28]. The information on the $\gamma_v NN^*$ electrocoupling evolution with Q^2 becomes critical in the search for hybrid baryons. A distinctively different Q^2 evolution of the hybrid-baryon electrocouplings is expected considering the different color-multiplet assignments for the quark-core in a regular versus a hybrid baryon, i.e. color singlet versus octet. Electromagnetic couplings have been studied within a non-relativistic constituent quark-gluon model, but only for two possible hybrid states, the Roper $N_G(1440)\frac{1}{2}^+$ and the $\Delta_G(1600)\frac{3}{2}^+$. In Ref. [29] the photoexcitation of the hybrid Roper resonance $N(1440)\frac{1}{2}^+$ was studied, and in Ref. [30] the electroproduction transition form factors of a hybrid Roper state were evaluated. The latter was essential in eliminating the Roper resonance as a candidate for a hybrid state, both due to the Q^2 dependence of its transverse helicity amplitude and the prediction of $S_{1/2}(Q^2) = 0$ at all Q^2 (see Fig. 2). It also showed that the hybrid Roper $A_{1/2}$ transition amplitude should behave like $A_{1/2}$ for the

ordinary $\Delta(1232)$. Clearly the $S_{1/2}$ amplitude behaves differently and $A_{3/2}$ does not exist for the Roper. Both amplitudes exhibit a Q^2 dependence that is distinctively different from the hybrid baryon prediction, especially the scalar amplitude $S_{1/2}(Q^2)$ which was found to be large, while it is predicted to be suppressed in leading order for the lowest mass $\frac{1}{2}^+$ hybrid state.

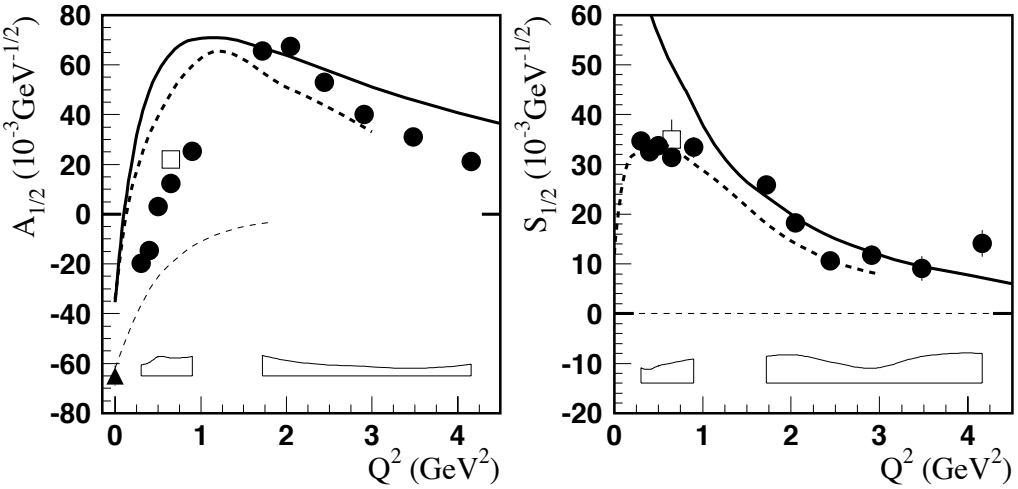

Figure 2: Electrocoupling amplitudes of the Roper resonance $N(1440)\frac{1}{2}^+$ [5]. The thin dashed lines are the constituent quark-glue model predictions for the gluonic Roper [25].

The aforementioned predictions should apply to each lowest mass hybrid state with $J^P = \frac{1}{2}^+$ and $\frac{3}{2}^+$. One may ask about the model-dependence of this prediction. The transverse amplitude has model sensitivity in its Q^2 dependence and it depends on the model ingredients, however, there are no ordinary three-quark model predictions that would come even close to the predictions of the hybrid quark-gluon model. The radial excitation of the Roper resonance gives a qualitatively different prediction for $A_{1/2}(Q^2)$ compared to the hybrid excitation, where the three-quark component remains in the ground state with only a spin-flip occurring (just as for the $N \rightarrow \Delta(1232)$ transition). The suppression of the longitudinal coupling, which is a property of the γqG vertex, is largely independent of specific model assumptions.

The $\Delta(1600)\frac{3}{2}^+$ was the other state considered as a hybrid candidate, specifically for the lowest mass gluonic Δ_G. A result similar to that for the hybrid Roper is found in Ref. [30] for a hybrid $\Delta_G(1600)\frac{3}{2}^+$, i.e. a fast falling $A_{1/2}(Q^2)$ and $S_{1/2}(Q^2) \approx 0$. The amplitudes at the photon point are not inconsistent with the ordinary three-quark model calculation but are inconsistent with the hybrid baryon hypothesis. On the other hand this result is also in line with the expectation that the lowest mass hybrid states should have considerably higher masses than the first radially excited quark states. Note that there are currently no experimental results for the Q^2 dependence of the $A_{1/2}$ and $S_{1/2}$ amplitudes of this state.

Based on constituent counting rules [31], we expect that the electrocouplings of hybrid baryons should decrease faster with increasing photon virtuality Q^2 than for regular three-quark nucleon resonances because of the extra constituent. Therefore, low photon virtualities are the preferential region to study hybrid baryons and we are proposing to explore the $Q^2 < 2.0$ GeV^2 range with a particular focus on the hybrid baryon search at $Q^2 < 1.0$ GeV^2.

In order to identify hybrid baryons, we are looking to map out their electrocoupling behavior, which should have distinctively different features in comparison with already established states from the CLAS results [7]. Electrocouplings of three-quark resonances for $J^P = \frac{1}{2}^+$ are shown in Figs. 2 and 3 and for $J^P = \frac{3}{2}^+$ in Figs. 4, 5, and 6. If hybrid baryons will be established in the proposed experiment, further studies of their electrocouplings can be extended towards higher photon virtualities from the data of the approved CLAS12 experiments [18, 19].

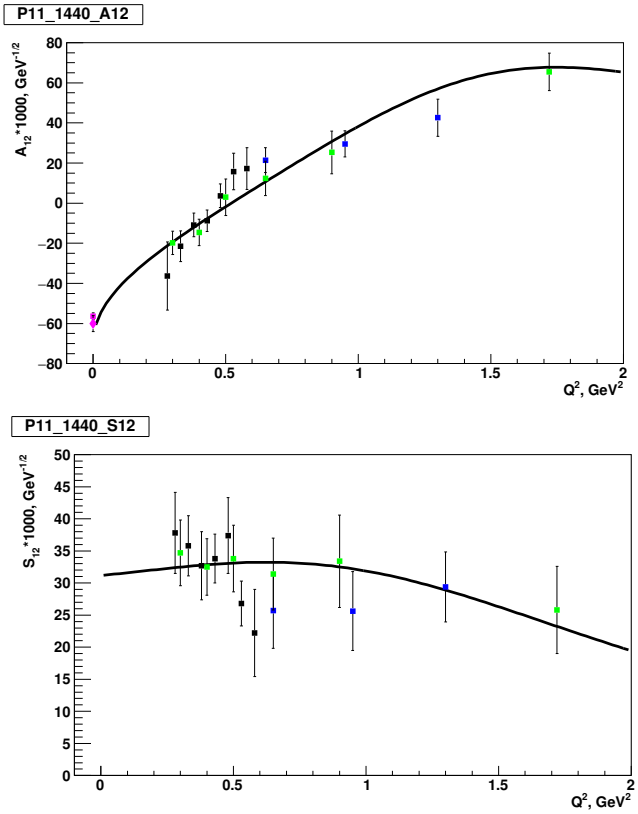

Figure 3: Electrocouplings of the $N(1440)\frac{1}{2}^+$ from the CLAS data on $N\pi$ (green circles) [5] and $\pi^+\pi^- p$ [13, 28] (black and blue squares) exclusive electroproduction off the proton. The results at the photon point are taken from Refs. [1, 32].

3 Strategies for Identifying New Baryon States

Advanced studies of the data for exclusive meson photoproduction off the proton carried out within the framework of the global multi-channel amplitude analysis developed by the Bonn-Gatchina group [35, 36, 37] have revealed many new baryon states in the mass range from 1.7 GeV to 2.5 GeV. These states were included in the PDG [1] with statuses from one to three stars. Notably, the most prominent signals for new states came from analyses of the CLAS [38, 39, 40, 41], ELSA [42], MAMI [43] and GRAAL [44, 45] data on KY photoproduction. However, studies of the KY as well as the $\pi^+\pi^- p$ exclusive electroproduction channels considerably extend our understanding of the excited nucleon state spectrum, including both regular three-quark and exotic hybrid states.

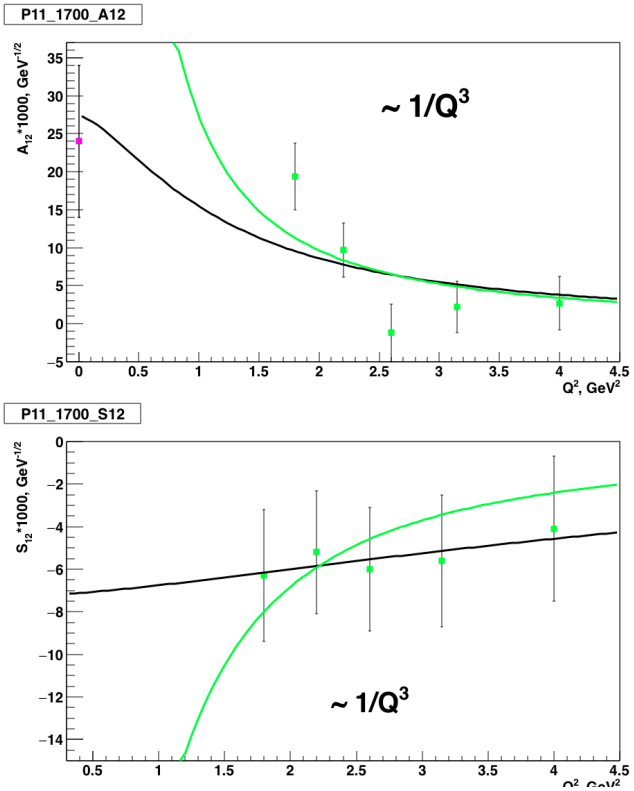

Figure 4: Electrocouplings of the $N(1720)\frac{3}{2}^+$ from the CLAS data on $\pi^+\pi^- p$ [33] exclusive electroproduction off the proton [34]. The results at the photon point are taken from Refs. [32, 33].

The new baryon states, if they are excited in the s-channel should be seen in exclusive reactions both with real and virtual photons in the same final states. Furthermore, their masses, total decay widths, and partial decay widths to different final states, should be Q^2 independent. The values of the $\gamma_v pN^*$ electrocouplings obtained independently from analyses of different exclusive channels with completely different non-resonant contributions should be the same. Consistent results over the full covered Q^2 range on resonance masses, $\gamma_v pN^*$ electrocouplings for all exclusive decay channels under study, and Q^2-independent partial hadronic decay widths, will offer convincing evidence for the existence of new states. These studies offer a model-independent way to prove not only the existence of new excited nucleon states, but also their nature as s-channel resonances, eliminating alternative interpretations for the structures observed in the kinematic dependencies of the observables as complex coupled-channel effects, dynamical singularities for the non-resonant amplitudes, kinematic reflections, etc.

The studies of the exclusive KY and $\pi^+\pi^- p$ electroproduction channels at $Q^2 < 2.0$ GeV^2 with the highest virtual photon flux ever achieved in exclusive electroproduction will allow us to solidify the results on the spectrum of excited nucleon states, confirming or ruling out the signal of "missing" resonances observed in exclusive photoproduction. Furthermore, for the first time the information on the $\gamma_v pN^*$ electrocouplings of new baryon states will become available, offering access to the structure of "missing" resonances and elucidating

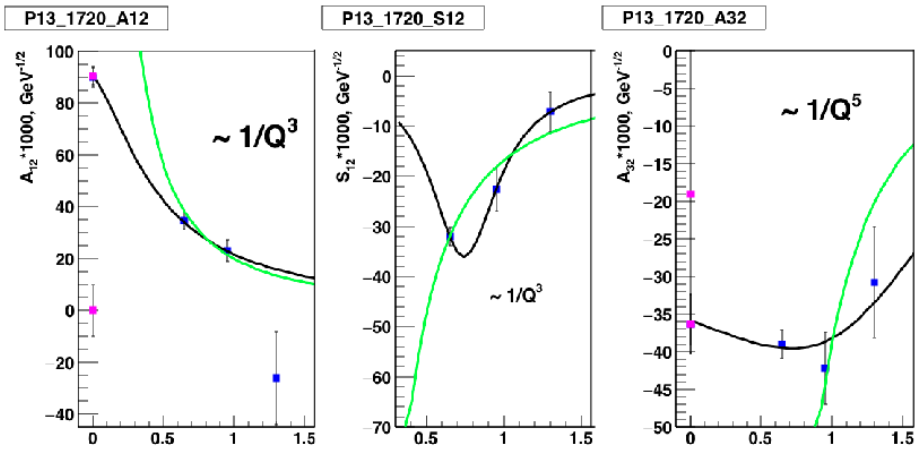

Figure 5: Electrocouplings of the $N(1720)\frac{3}{2}^+$ $A_{1/2}$ (left), $S_{1/2}$ (middle), and $A_{3/2}$ (right) from the CLAS data on $\pi^+\pi^- p$ [33] exclusive electroproduction off the proton [34]. The results at the photon point are taken from Refs. [32, 33].

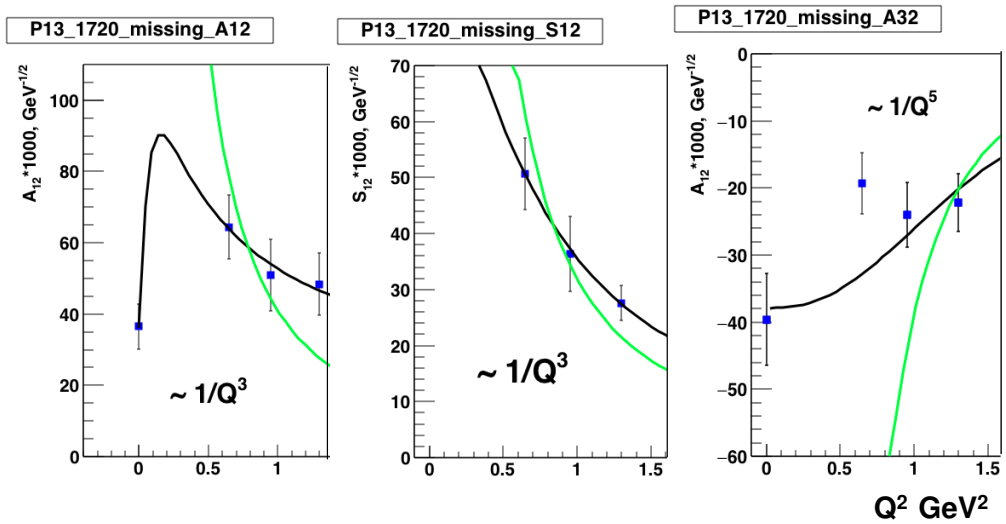

Figure 6: Electrocouplings of the $N'(1720)\frac{3}{2}^+$ $A_{1/2}$ (left), $S_{1/2}$ (middle), and $A_{3/2}$ (right) electrocouplings from the CLAS data on $\pi^+\pi^- p$ [33] exclusive electroproduction off the proton [34]. The results at the photon point are taken from Refs. [32, 33].

any differences from the conventional resonances. Finally, in this general introduction to our strategies for identifying new baryon states, we want to note that studies of the two major exclusive $N\pi$ and $\pi^+\pi^- p$ electroproduction channels with CLAS have revealed the relative growth of the resonant contributions with Q^2 in both channels. Therefore the use of the high-intensity virtual photon fluxes in the proposed experiment is preferential for a new baryon state search in comparison to photoproduction. It still remains to be seen which range of photon virtualities is the most suitable for the discovery of new excited nucleon states.

In this section we address the question of how gluonic hybrid baryons are distinct from ordinary three quark baryon excitations and we will also elucidate additional opportunities offered by studies of exclusive electroproduction processes at different photon virtualities for the search of new baryon states, both hybrid baryons and regular three-quark states.

3.1 Search for Hybrid Baryon States

As discussed in Section 2.2 the lowest hybrid baryons should have isospin $I = \frac{1}{2}$ and $J^P = \frac{1}{2}^+$ or $J^P = \frac{3}{2}^+$. Their masses should be in the range from 2.2 GeV to 2.5 GeV. This mass range will be further refined once LQCD calculations with physical pion masses become available, since masses may shift toward lower values with more realistic pion masses. Four regular states with $I = \frac{1}{2}$ and $J^P = \frac{1}{2}^+$ are predicted with dominant three-quark contributions and with masses below the mass of the lowest LQCD hybrid states. Of these four states two are the well known $N(1440)\frac{1}{2}^+$ and $N(1710)\frac{1}{2}^+$, and two are the less well established $N(1880)\frac{1}{2}^+$ and $N(2100)\frac{1}{2}^+$ with 2^* and 1^* ratings, respectively. Another state, the $N(2300)$, has a 2^* rating and falls right into the lowest hybrid mass band predicted by LQCD. This state, if confirmed, could be a candidate for the predicted lowest mass LQCD hybrid state.

In order to address this question, it is necessary to confirm (or refute) the existence of the 2^* state $N(1880)$ and of the 1^* state $N(2100)$, and to measure the electromagnetic couplings of the $N(2300)$ and their Q^2 dependences. Improved information on the lower mass states should become available in the next one or two years when the new high-statistics single- and double-polarization data from CLAS have been fully included into the multi-channel analysis frameworks such as the Bonn-Gatchina and the Jülich/GWU approaches. Should these two states be confirmed, then any new nucleon state with $J^P = \frac{1}{2}^+$, which happens to be in the right mass range, should be a candidate for the lowest mass hybrid baryon. Another $N(2300)\frac{1}{2}^+$ state has only been seen at BES III in the invariant mass $M(p\pi^0)$ of $\Psi(2S) \to p\bar{p}\pi^0$ events [46]. In this case the production of the $N(2300)$ occurs at very short distances as it emerges from heavy quark flavor $c\bar{c}$ decay. Hence this state may even be observed in single pion electroproduction $ep \to e'\pi^+ n$ and $ep \to e'p'\pi^0$ if it couples to photons with sufficient strength to be measurable.

In the $J^P = \frac{3}{2}^+$ sector the situation is more involved. There are two hybrid states predicted in the mass range 2.2 GeV to 2.4 GeV, with masses above five quark model states at the same J^P. Of the five states, two are the well known 4^* and 3^* states, the $N(1720)\frac{3}{2}^+$ and the $N(1900)\frac{3}{2}^+$, respectively, and one state, the $N(2040)\frac{3}{2}^+$, has a 1^* rating. Here we will have to confirm (or refute) the 1^* star state and find two or three (if the $N(2040)$ does not exist) more quark model states with the same quantum numbers in the mass range 1.7 GeV to 2.1 GeV. There is one candidate $\frac{3}{2}^+$ state near 1.72 GeV seen in $p\pi^+\pi^-$ electroproduction

[47], whose status will be pinned down with the expected very high statistics data.

Possible signatures of the lowest mass hybrid baryons are:

- Resonance masses in the range of 2.2 GeV $< W <$ 2.5 GeV with $I = \frac{1}{2}$, $J^P = \frac{1}{2}^+$ or $J^P = \frac{3}{2}^+$, and almost degenerate masses where no regular three-quark states are observed
- Q^2 dependence of the $A_{1/2}(Q^2)$ transverse helicity amplitude similar to that for the $\Delta(1232)\frac{3}{2}^+$ but different from the three-quark excited states with the same J^P, and
- A strongly suppressed helicity amplitude $S_{1/2}(Q^2) \approx 0$ in comparison to other ordinary three-quark states or meson-baryon excitations.

This list of expected hybrid signatures may provide some initial guidance when examining new baryon states for possible large gluonic components. However, they are not sufficient to firmly establish the hybrid nature of a state. To achieve this goal, improved modeling of other degrees-of-freedom, such as meson-baryon contributions and direct calculations of electrocouplings from LQCD, will be needed. The expected high statistics data will be used to identify any new or poorly known state, whether or not it is a candidate for a hybrid baryon state. This will aid in the identification of the effective degrees of freedom underlying the resonance excitation of all states that couple to virtual photons.

3.2 Known and New Three-Quark Baryon States

Besides the search for hybrid baryon states, there are many open issues in our knowledge of the structure of ordinary baryon excitations that can be addressed with the data taken in parallel from the proposed experiment. As an example we show in Fig. 7 the electrocouplings of the $N(1680)\frac{5}{2}^+$ resonance [48], the strongest state in the third nucleon resonance region. With the exception of the real photon point, the data are quite sparse for $Q^2 \leq 1.8$ GeV^2 and the high statistics data expected from this experiment would remedy the lack of experimental information and address similar situations for other states as well. Note that the high-Q^2 part will be covered by the approved JLab experiment E12-09-003 [18].

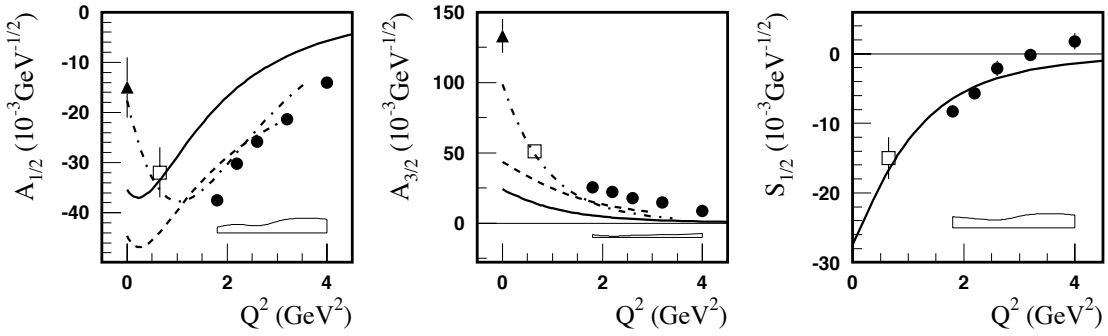

Figure 7: Electrocoupling amplitudes $A_{1/2}$ (left), $A_{3/2}$ (middle), and $S_{1/2}$ (right) of the $N(1680)\frac{5}{2}^+$ resonance [48].

An even more compelling example is the $N(1675)\frac{5}{2}^-$ state, where data at $Q^2 > 1.8$ GeV^2 have been published recently by the CLAS Collaboration [48]. Fig. 8 shows the measured helicity amplitudes. Low Q^2 data are very important here, as for this state the quark transitions are strongly suppressed by the Moorhouse selection rule, and therefore, any non-zero value of the electrocoupling amplitudes will directly measure the strength of the meson-baryon contributions. The main data needed are single pion production $ep \to e'\pi^+ n$ and $ep \to e'\pi^0 p$. These processes can be accumulated with sufficiently high event rates, even with a pre-scale factor of 10 on the Forward Tagger, should the overall event rate be too high in this two-prong topology.

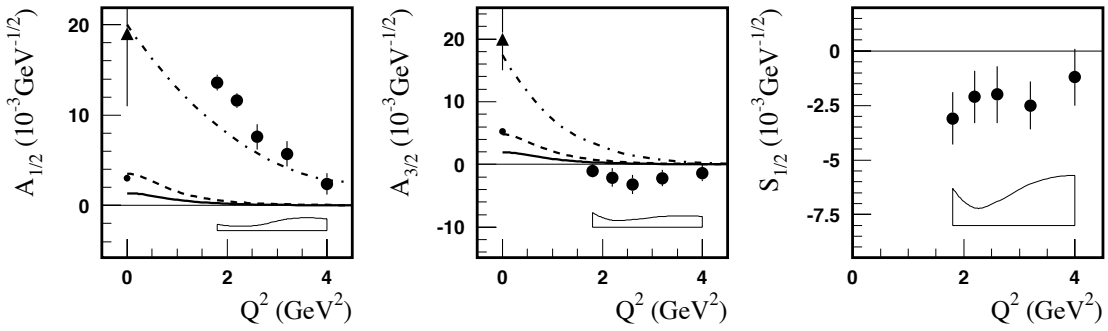

Figure 8: Electrocoupling amplitudes $A_{1/2}$ (left), $A_{3/2}$ (middle), and $S_{1/2}$ (right) of the $N(1675)\frac{5}{2}^-$ resonance [48]. Quark models predict the transverse amplitudes to be suppressed. The significant deviation of the $A_{1/2}$ amplitude from zero is consistent with meson-baryon contributions to the excitation strength (dashed-dotted lines).

The recent combined analysis [33] of the CLAS $\pi^+\pi^- p$ photoproduction [49] and electroproduction [47] data revealed further convincing evidence for a new $N'(1720)\frac{3}{2}^+$ baryon state. This state has the same spin-parity and almost the same mass and total decay width as the conventional $N(1720)\frac{3}{2}^+$, but a distinctively different Q^2 evolution of the resonance electrocouplings (see Figs. 5 and 6) and partial hadronic decay widths to the $\pi\Delta$ and ρp final states. The electrocouplings of the new $N'(1720)\frac{3}{2}^+$ state are available at the photon point and in the limited Q^2 range from 0.5 GeV^2 to 1.5 GeV^2. As shown in Figs. 5 and 6, the $A_{1/2}(Q^2)$ electrocouplings of the $N(1720)\frac{3}{2}^+$ and $N'(1720)\frac{3}{2}^+$ states evolve for $Q^2 < 0.5$ GeV^2 in a completely different manner. The $A_{1/2}(Q^2)$ amplitude of the conventional $N(1720)\frac{3}{2}^+$ baryon state decreases with Q^2, while it increases for the new $N'(1720)\frac{3}{2}^+$ state in the range of $Q^2 < 0.5$ GeV^2. Therefore, the future results on the $N(1720)\frac{3}{2}^+$ and $N'(1720)\frac{3}{2}^+$ state electrocouplings from the data on exclusive $\pi^+\pi^- p$ electroproduction off the proton at small Q^2 will shed light on the differences in the structure of the conventional and the "missing" baryon states.

In general, the studies of resonance electrocouplings at small photon virtualities in the proposed experiment will, for the first time, allow us to explore their Q^2 evolution at distance scales where the meson-baryon cloud contributions are expected to be largest, offering preferential conditions for exploration of this component of N^* structure. Recent advances in the studies of nucleon structure using QCD-based Dyson-Schwinger equations have provided strong indications that quark-gluon confinement in the real-world is a dynamical process

and point to an intimate connection between confinement and Dynamical Chiral Symmetry Breaking (DCSB) [50, 51]. Moreover, in providing a clear explanation of the dichotomous nature of pions, as both bound-states of massive constituents and Nambu-Goldstone bosons, these studies force a realization that baryons constituted from fully-dressed confined-quarks must also be surrounded by a complex meson-baryon cloud, generated by a sequence of meson-baryon final-state interactions. A detailed understanding of the interplay between the dressed-quark core in a diverse array of nucleon excited states and the associated meson-baryon clouds is crucial to developing a quantitative picture of the dynamical confinement mechanism; and this requires a systematic investigation of resonance electrocouplings at low virtuality. The studies proposed herein will therefore address a critical open problem in hadron physics; namely, exposing those features of the hadronization process which control the transition from the quark-gluon color-confinement regime to the asymptotic domain of strong interactions between color-neutral mesons and baryons.

3.3 Amplitude Analyses in the Search for New Baryon States

In our studies of the experimental data we will start from the extraction of the resonance parameters from the independent analyses of the KY and $\pi^+\pi^-p$ final states carried out within the framework of the reaction models for the description of these exclusive channels. Eventually we will employ the amplitude analysis methods for the resonance search and extract the resonance parameters in a global fit of all exclusive channels studied with CLAS12. Consistent results on the resonant parameters determined from independent analyses of different exclusive meson electroproduction channels and extracted from a global multi-channel fit of all available data will offer strong and almost model independent evidence for the existence of any new states and the reliable extraction of their parameters. Note, that in order to apply the coupled-channel approaches to the analyses of KY and $\pi^+\pi^-p$ exclusive electroproduction data, information on $N\pi$ electroproduction is also needed. The $N\pi$ exclusive channels dominate at $W < 1.6$ GeV. These cross sections remain much larger in comparison with the KY channels over our entire kinematics area. The events from the $N\pi$ exclusive channels will be collected simultaneously in CLAS12 with those for the KY and $\pi^+\pi^-p$ channels.

The advanced amplitude analysis approach for extraction of the nucleon resonance parameters from the global analysis of the photoproduction data, which includes almost all relevant exclusive γp meson production channels in the nucleon resonance region, has been developed by the Bonn-Gatchina group [35, 36, 37]. In this approach, the production amplitudes are decomposed over the set of partial waves. The partial wave amplitudes are parameterized fully accounting for the restrictions imposed by the general unitarity and analyticity conditions, employing the K- and D-matrix approaches for the final hadron rescattering, while for the photoproduction amplitudes, the P-vector approach is used. In the case of pronounced t-channel contributions, Reggeized t-exchanges are incorporated into the photoproduction amplitudes. The resonance parameters were determined from the global fit of all available exclusive photoproduction data augmented by the fit of the final state hadroproduction. Application of the Bonn-Gatchina approach to the global analysis of the dominant part of the exclusive meson photoproduction data measured with CLAS and elsewhere has provided information on masses, widths, photocouplings, and hadronic decay

parameters for most excited nucleon states in the mass range up to 3 GeV. These analyses have revealed evidence for ∼10 new baryon states, reported in the PDG [1] with status from one to three stars (see Fig. 9).

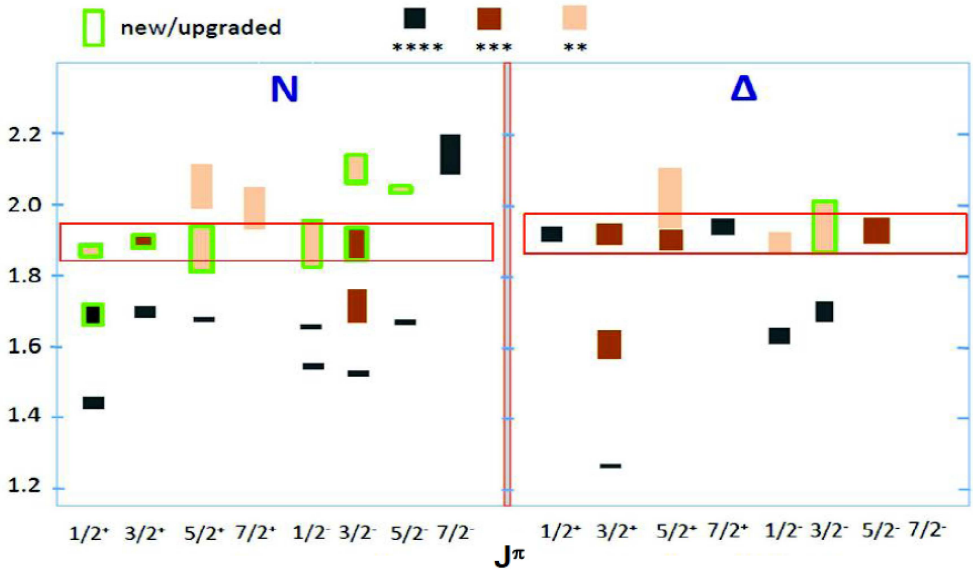

Figure 9: Recent results on the spectrum of excited nucleon states [1]. Signals from the states shown in the green boxes were observed in a global multi-channel analysis of exclusive meson photoproduction data carried out within the framework of the Bonn-Gatchina approach [35, 36, 37].

An extension of this approach for the description of the exclusive electroproduction channels represents a future commitment of the Bonn-Gatchina group [52]. The Bonn-Gatchina approach extended for the analysis of the exclusive electroproduction channels will be used for the extraction of the resonance parameters and the search for new baryon states in the proposed experiment. This extension will be vital in order to check the signals from new baryon states observed in the exclusive meson photoproduction independently in the exclusive electroproduction processes, confirming or rejecting the candidate states.

An advanced dynamical coupled-channel (DCC) model has been developed by the Argonne-Osaka Collaboration for the combined analysis of the world data for $\pi N, \gamma N \to \pi N$, ηN, $K\Lambda$, $K\Sigma$, and $N\pi\pi$ photo-, electro-, and hadroproduction with a goal of extracting resonance parameters [53, 54]. The DCC approach incorporates tree level diagrams derived from an effective Lagrangian for the resonant and non-resonant contributions to photo- and electroproduction, as well as to the final state hadronic interactions. The amplitudes for all exclusive channels are fully consistent with the restrictions imposed by the general unitarity and analyticity conditions. This is the only coupled-channel approach capable of describing the $N\pi\pi$ data in accord with the general unitarity condition. In order to fulfill the unitarity restrictions, the meson-baryon interactions present in the non-resonant amplitudes of the included exclusive channels are incorporated into the electromagnetic and hadronic vertices of nucleon resonances, together with the direct resonance decays to the $\gamma_{r,v}p$ and meson-baryon final states. The former generate the so-called meson-baryon cloud contributions to the bare verticies for the resonance electromagnetic and/or hadronic decays. Analysis of

the observables within the framework of the DCC approach allows us not only to extract the fully dressed resonance electromagnetic and hadronic decay amplitudes, but also to disentangle the contributions from the meson-baryon cloud and the bare vertices associated with the quark core in the nucleon resonance structure. In this way, the DCC approach is capable of providing valuable insight into the structure of excited nucleon states. The DCC model currently is the only available coupled-channel approach that has provided results on the structure of excited nucleon states from analysis of the CLAS $N\pi$ electroproduction data [5], including the $N \to \Delta(1232)\frac{3}{2}^+$ transition form factors at Q^2 up to 7 GeV^2 [7] and the $N(1440)\frac{1}{2}^+$ electrocouplings at Q^2 up to 3 GeV^2 [55].

The Argonne-Osaka DCC model will be employed in the analysis of the data of the proposed experiment with the goal to observe manifestations of the new excited nucleon states and to extract the $\gamma_v pN^*$ electrocouplings of the established and new baryon states. This model will allow us to fully account for the impact of the final state interactions in the extraction of the $\gamma_v pN^*$ electrocouplings from the KY channels with the $N\pi$, and $N\pi\pi$ open channels for which the electroproduction cross sections are much larger.

The $N\pi$ data have been analyzed within the framework of two conceptually different approaches: a unitary isobar model (UIM) and dispersion relations (DR) [5, 48]. The UIM describes the $N\pi$ electroproduction amplitudes as a superposition of N^* electroexcitations in the s-channel, non-resonant Born terms, and ρ and ω t-channel contributions. The latter are Reggeized, which allows for a better description of the data in the second- and third-resonance regions. The final-state interactions are treated as πN rescattering in the K-matrix approximation [5]. In the DR approach, the dispersion relations relate the real to the imaginary parts of the invariant amplitudes that describe the $N\pi$ electroproduction. Both approaches provide a good and consistent description of the $N\pi$ data in the range of $W < 1.7$ GeV and $Q^2 < 5.0$ GeV^2, resulting in $\chi^2/d.p. < 2.9$. In this proposal, this approach will be used for the evaluation of the $N\pi$ electroproduction amplitudes needed as the input for the aforementioned global multi-channel analyses of the KY and $\pi^+\pi^- p$ exclusive electroproduction data.

The $\pi^+\pi^- p$ electroproduction data from CLAS [34, 56] provide for the first information on nine independent single-differential and fully-integrated cross sections binned in W and Q^2 in the mass range $W < 2.0$ GeV and at photon virtualities of 0.25 GeV$^2 < Q^2 < 1.5$ GeV^2. The analysis of the data have allowed us to develop the JM reaction model [11, 13, 28] with the goal of extracting the resonance electrocouplings, as well as the $\pi\Delta$ and ρp hadronic decay widths. This model incorporates all relevant reaction mechanisms in the $\pi^+\pi^- p$ final-state channel that contribute significantly to the measured electroproduction cross sections off the proton in the resonance region, including the $\pi^-\Delta^{++}$, $\pi^+\Delta^0$, $\rho^0 p$, $\pi^+ N(1520)\frac{3}{2}^-$, $\pi^+ N(1685)\frac{5}{2}^+$, and $\pi^-\Delta(1620)\frac{3}{2}^+$ meson-baryon channels, as well as the direct production of the $\pi^+\pi^- p$ final state without formation of intermediate unstable hadrons. In collaboration with JPAC [57], a special approach has been developed allowing us to remove the contributions from the s-channel resonances to the Reggeized t-channel non-resonant terms in the $\pi^-\Delta^{++}$, $\pi^+\Delta^0$, and $\rho^0 p$ electroproduction amplitudes. The contributions from well established N^* states in the mass range up to 2 GeV were included into the amplitudes of the $\pi\Delta$ and ρp meson-baryon channels by employing a unitarized version of the Breit-Wigner ansatz [13]. The JM model provides a good description of the $\pi^+\pi^- p$ differential cross sections at $W < 1.8$ GeV and 0.2 GeV$^2 < Q^2 < 1.5$ GeV^2 with $\chi^2/d.p. < 3.0$. The

achieved quality of the CLAS data description suggests an unambiguous and credible separation between the resonant and non-resonant contributions [28]. The credible isolation of the resonant contributions makes it possible to determine the resonance electrocouplings and the $\pi\Delta$ and ρN decay widths from the resonant contributions employing for their description the amplitudes of the unitarized Breit-Wigner ansatz [13] that fully accounts for the unitarity restrictions on the resonant amplitudes. This model will be used in the proposed experiment for the analysis of exclusive $\pi^+\pi^- p$ electroproduction, allowing us to determine the electrocouplings of most excited nucleon states, since almost all nucleon resonances have substantial hadronic decays to the $N\pi\pi$ channel. The capability of the JM model to pin down new baryon states was demonstrated in the combined studies of exclusive $\pi^+\pi^- p$ photo- and electroproduction [33], which provided convincing evidence for a new $N(1720)\frac{3}{2}^+$ baryon state.

The model employed for the description of the KY exclusive photo- and electroproduction channels is the "Regge-Plus-Resonance" (RPR) approach developed by the Ghent group [12, 58]. In this model the full production amplitude is described by the superposition of eight resonances and the non-resonant contribution. The non-resonant amplitudes represent the sum of t-channel exchanges by K- and K^*-Regge trajectories. The model provided a good description of KY photoproduction data. However, the RPR model only is able to produce the gross features of the available electroproduction data. The world's database for $K^+\Lambda$ and $K^+\Sigma^0$ electroproduction in the nucleon resonance region ($1.6 < W < 3.0$ GeV) in the domain of momentum transfer $0.5 < Q^2 < 4$ GeV^2 is completely dominated by the measurements of the CLAS program. These include measurements of beam-recoil transferred polarization [59, 60] and induced recoil polarization [61]. Also extensive measurements of the separated structure functions $\sigma_U = \sigma_T + \epsilon\sigma_L$, σ_{LT}, σ_{TT}, and $\sigma_{LT'}$ [62, 63, 64] have been published. Finally, the first Rosenbluth separation from CLAS data at beam energies of 2.5 and 4 GeV allowed for a separation of σ_T and σ_L [62, 65]. We are planning to use the RPR model for the extraction of the resonance electrocouplings from exclusive KY electroproduction data after the model has been refit and upgraded to be able to describe the available data. The development in this direction was presented in Ref. [66].

4 The Experimental Program

4.1 The CLAS12 Detector

The experimental program will use the CLAS12 detector, shown in Fig. 10, for the detection of the hadronic final states. CLAS12 consists of a Forward Detector (FD) and a Central Detector (CD). The Forward Detector is comprised of six symmetrically arranged sectors defined by the six coils of the superconducting torus magnet. Charged particle tracking is provided by a set of 18 drift chambers with a total of 36 layers in each sector. Additional tracking at $5^\circ - 35^\circ$ is achieved by a set of 6 layers of micromesh gas detectors (micromegas) immediately downstream of the target area and in front of the High Threshold Cherenkov Counter (HTCC). Particle identification is provided by time-of-flight information from two layers of scintillation counter detectors (FTOF). Electron, photon, and neutron detection are provided by the triple layer electromagnetic calorimeter, PCAL, EC(inner), and EC(outer). The heavy gas Cherenkov Counter (LTCC) provides separation of high momentum pions

from kaons and protons. The Central Detector consists of 6 to 8 layers (depending on the configuration) of silicon strip detectors with stereo readout and 6 layers of micromegas arranged as a barrel around the target, a barrel of scintillation counters to measure the particle flight time from the target (CTOF), and a scintillation-counter based Central Neutron Detector (CND). Further details on all CLAS12 components (magnets, detectors, data acquisition, software) are given in Ref. [67].

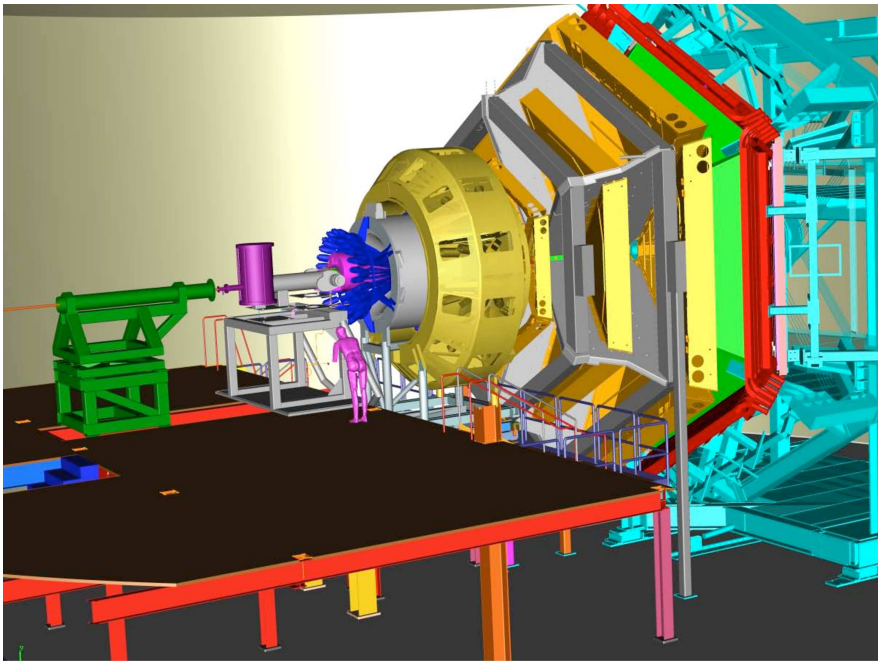

Figure 10: A model view of the CLAS12 detector that was designed to have high hermeticity and to allow for reconstruction of high multiplicity final states. This detector was designed to operate at a nominal luminosity of $\mathcal{L} > 10^{35}\text{cm}^{-2}\text{s}^{-1}$.

A longitudinally polarized electron beam will be scattered off a liquid-hydrogen target. The scattered electrons will be detected in the Forward Detector of CLAS12 for scattering angles greater than about 5° and in Forward Tagger for angles from 2.5° to 4.5°, which allows us to cover the Q^2 range of interest between 0.05 GeV^2 and 2 GeV^2. Charged hadrons will be measured in the full polar angle range from 5° to 130°. At an operating luminosity of $\mathcal{L} = 1 \times 10^{35}$ cm^{-2}s^{-1} the total hadronic rate is expected to be 5×10^6 s^{-1}.

4.2 The Forward Tagger

An essential component of the hadron spectroscopy program with CLAS12 is the Forward Tagger (FT) shown in Fig. 11. The FT uses a high resolution crystal calorimeter composed of 324 lead-tungstate crystals to measure the scattered electrons in the polar angle range from 2.5° to 4.5° and with full coverage in azimuthal angle. The calorimeter measures electron and photon energies with an energy resolution of $\sigma(E)/E \leq 0.02/\sqrt{E(\text{GeV})} + 0.01$. The fine granularity of the calorimeter also provides good polar angle resolution. A two-layer tiled scintillator hodoscope is located in front of the calorimeter for the discrimination of photons. An additional four-layer micromegas tracker, located in front of the hodoscope, is used for precise electron tracking information. Electron detection in the FT will allow us to probe

the crucial low Q^2 range where hybrid baryons may be identified due to their fast dropping $A_{1/2}(Q^2)$ amplitude and the expected suppression of their scalar $S_{1/2}(Q^2)$ amplitude.

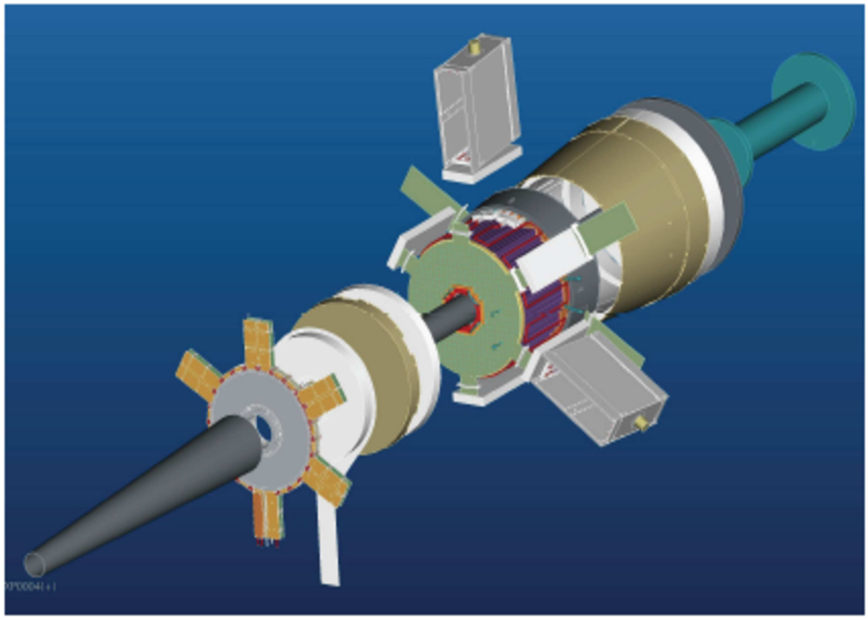

Figure 11: The Forward Tagger (FT) system. The FT provides electron and high energy photon detection in a range of CLAS12 polar angles $\theta = 2.5^\circ - 4.5^\circ$.

The construction of the FT was completed by a collaboration of INFN/Genova (Italy), CEA/Saclay (France), and the University of Edinburgh (UK). The FT is now undergoing cosmic ray testing at JLab and will be installed into CLAS12 in summer 2016.

4.3 Kinematic Coverage of Electron Scattering in CLAS12

The CLAS12 detector acceptance for inclusive electron scattering events has been studied using a fast Monte Carlo program (FASTMC), which includes a simplified version of the full CLAS12 reconstruction code. The event reconstruction takes into account the high efficient fiducial areas of the detector and provides smearing of the final state charged particle momenta. The optimal beam energies and torus current settings have been studied with the goal to maximize the scattered electron acceptance in Q^2 and W.

The virtuality of the emitted photon Q^2 is related to the scattered electron energy E'_e and polar angle θ_e through the relation $Q^2 = 4E_eE'_e\sin^2\frac{\theta_e}{2}$. Reaching the lowest Q^2 requires detecting the electrons emitted with the smallest scattering angle in the FT and using relatively low electron beam energies.

If a positive torus current is applied, the scattered electrons are forced to bend inward toward the beam axis, which causes an increase in the minimum detectable Q^2 value in CLAS12. On the contrary, a negative torus current forces the scattered electrons to bend outward, lowering the value of the minimum accessible Q^2. Fig. 12 shows scatterplots of Q^2 vs. W for the detected electrons in CLAS12 for torus currents of $I = +3375$ A and $I = -3375$ A (the nominal maximum supply operating current) at E_b=11 GeV, the maximum electron beam energy available in Hall B. The empty region corresponds to the gap between

the FT and the minimum polar angle accepted in the CLAS12 Forward Detector calorimeters. This coverage gap is clearly minimized operating the torus magnet at negative polarity. The corresponding electron acceptances vs. Q^2 are also shown in Fig. 12. The electrons that are detected in the FT at E_b=11 GeV correspond to an accessible Q^2 range from 0.2 GeV^2 to 0.6 GeV^2. The electrons detected in the CLAS12 Forward Detector calorimeters have a lower geometrical efficiency due to the defined fiducial areas of these detectors and cover a higher Q^2 range that starts from 0.8 GeV^2 or 1.4 GeV^2 for the negative and positive torus currents, respectively.

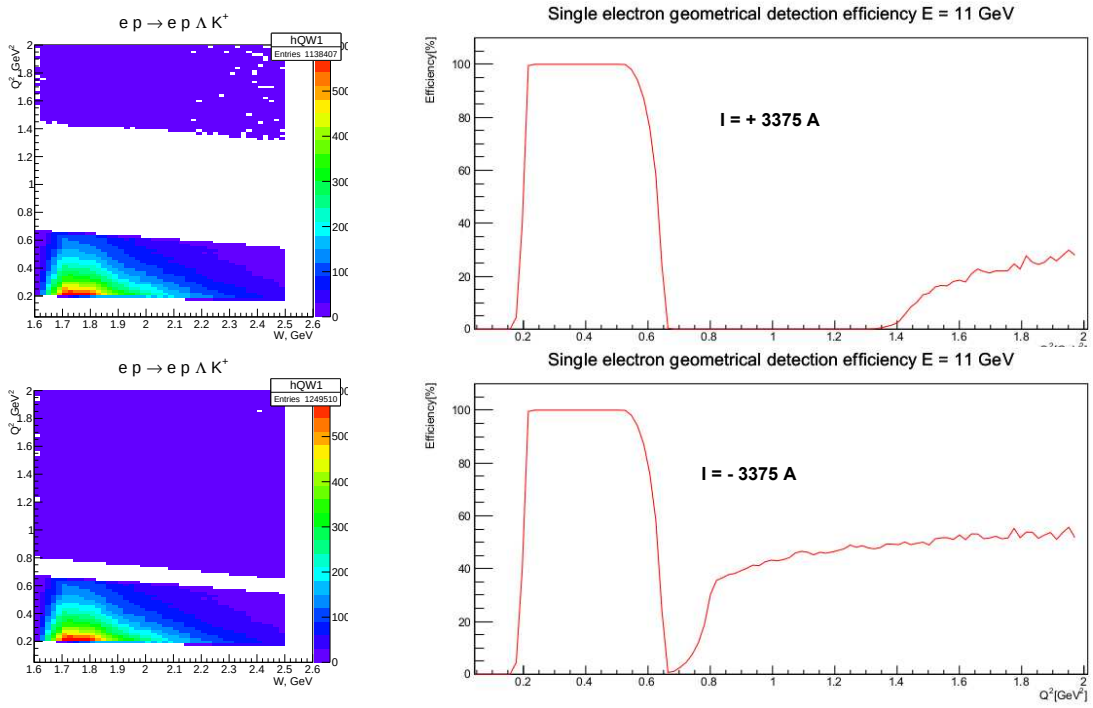

Figure 12: (Left) Q^2 vs. W scatterplots of the detected electrons in CLAS12 for the $ep \rightarrow e'K^+\Lambda$ reaction for torus currents $I = +3375$ A (top) and $I = -3375$ A (bottom) for $E_e = 11$ GeV. (Right) The corresponding electron acceptances as a function of Q^2.

Reaching the low-Q^2 region desired for this proposal requires lowering the electron beam energy. Fig. 13 shows a scatterplot of Q^2 vs. W for the detected electrons in CLAS12 for a torus current of $I = -3375$ A at electron beam energies of E_e=6.6 GeV and E_e=8.8 GeV. The corresponding electron acceptances vs. Q^2 at these energies are also shown in Fig. 13. At E_e=6.6 GeV the minimum accepted Q^2 value is as low as 0.05 GeV^2 and the accessible Q^2 range extends up to 2 GeV^2, with a gap between 0.15 GeV^2 and 0.3 GeV^2. This gap may be covered if an electron beam energy of E_e=8.8 GeV is used, as shown in the bottom plots of Fig. 13. In this case the Q^2 threshold is 0.1 GeV^2 and the acceptance gap appears in the interval from 0.35 GeV^2 to 0.5 GeV^2, providing a nicely complementary range of measurable photon virtualities.

We conclude that the optimal experimental settings for the present proposal require beam time at both E_e=6.6 GeV and E_e=8.8 GeV with operation of the CLAS12 torus at $I = -3375$ A, corresponding to negative polarity with the current set to its maximum nominal value. Detailed simulations for the $\pi^+\pi^-p$ final state are described in Section 5 and for the KY final states in Section 6.

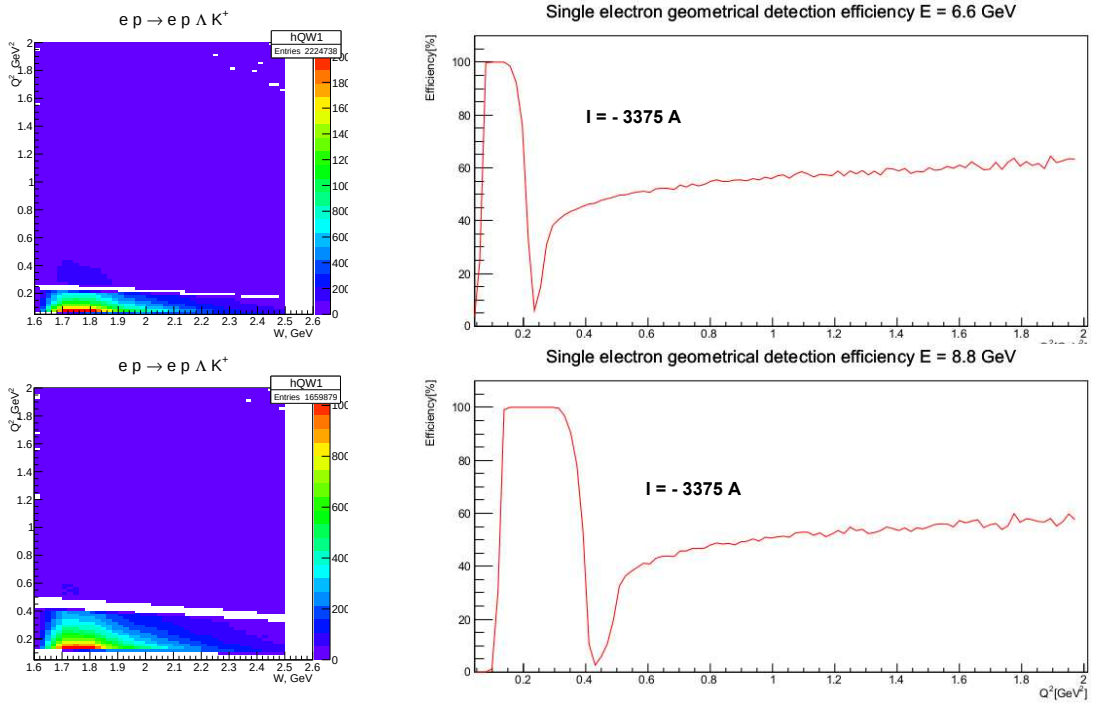

Figure 13: (Left) Q^2 vs. W scatterplots of the detected electrons in CLAS12 for the $ep \to e'K^+\Lambda$ reaction for torus current $I = -3375$ A for $E_e = 6.6$ GeV (top) and $E_e = 8.8$ GeV (bottom). (Right) The corresponding electron acceptances as a function of Q^2.

5 Simulations for the $ep \to e'p\pi^+\pi^-$ Final State

5.1 Event Generator for $ep \to e'p\pi^+\pi^-$

The standard 2π event generator for CLAS was a modified version of GENEV employing the $\pi^+\pi^-p$ differential cross sections from the older JM05 version of the JM model [34, 68, 69]. During the past several years the JM model has been further developed and significantly improved [11]. Furthermore, the two-pion part of the old GENEV event generator was only applicable up to $W \approx 2$ GeV and $Q^2 < 0.3$ GeV^2, which excludes most of the region of interest (high W and low Q^2) for this proposal. Therefore a new generator for $\pi^+\pi^-p$ electroproduction was developed for our studies.

The new event generator employs the five-fold differential cross sections from the recent version of the JM15 model fit to all results on the charged double pion photo- and electroproduction cross sections from CLAS (both the published and preliminary [13, 47, 49, 56]). In the areas covered by CLAS data, the new event generator successfully reproduces the available integrated and single differential 2π cross sections. The quality of the description is illustrated in Fig. 14 for several Q^2 bins in comparison with the available data [13, 47, 56].

In order to extend the event generator to areas not covered by the existing CLAS data, a special extrapolation procedure was applied that included additional available world data on the W dependencies of the integrated 2π photoproduction cross sections [70, 71]. The new approach allows for the generation of 2π events at extremely low Q^2 (less than 0.1 GeV^2) and high W (up to 3 GeV). On the left side of Fig. 15 the W dependence of the integrated cross section for quasi-real Q^2 (0.0015 GeV^2) is shown in comparison with the available data

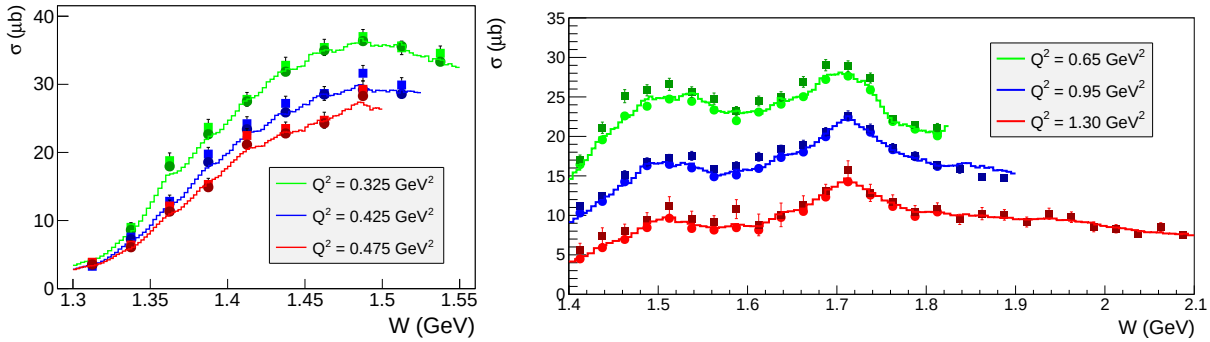

Figure 14: Comparison between the event distributions of the new two-pion event generator (curves) with the integrated cross sections from the JM model (circles) and data (squares). (Left) The W dependence of the total cross section in comparison with the model [13] and data [56] for three Q^2 points at 0.325 GeV^2, 0.425 GeV^2, and 0.475 GeV^2. (Right) The W dependence of the total cross section in comparison with the model [11] and data [47] for three Q^2 points at 0.65 GeV^2, 0.95 GeV^2, and 1.3 GeV^2.

[49, 70, 71]. The right side of Fig. 15 illustrates a typical example of the Q^2 dependence of the total cross section for one W bin in comparison with JM15 [11] for E_b=8.8 GeV.

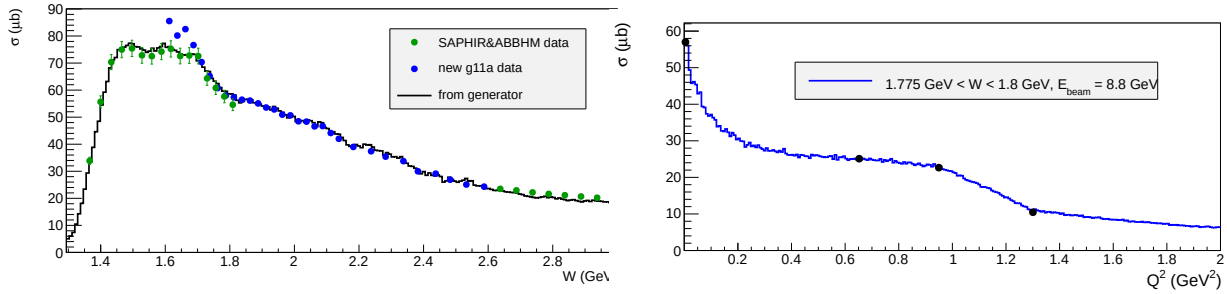

Figure 15: (Left) The W dependence of the integrated cross section for quasi-real Q^2 (0.0015 GeV^2) in comparison with the available data [49, 70, 71]. (Right) A typical example of the Q^2 dependence of the total cross section for one W bin in comparison with JM15 [11] at W = 1.7875 GeV for E_b=8.8 GeV.

The new 2π event generator has several advantages compared to the GENEV code. First it generates phase space distributions and applies a multi-dimensional cross section as a weight for each event. This method allows for a significantly faster generation process, especially in the areas with sharp cross section dependencies. The new generator also makes it possible to obtain cross sections from the generated distributions, which is helpful to predict the cross section in areas not covered by the experiment. The new 2π event generator is written in C++. It includes inclusive radiative effects according to the approach described in Ref. [72] and produces an output compatible with the new CLAS12 reconstruction software.

Exclusive events for $\pi^+\pi^-p$ electroproduction off the proton were generated in the range of W from the two-pion production threshold to 3 GeV and at Q^2 from 0.01 GeV^2 to 2.0 GeV^2 (see Fig. 16).

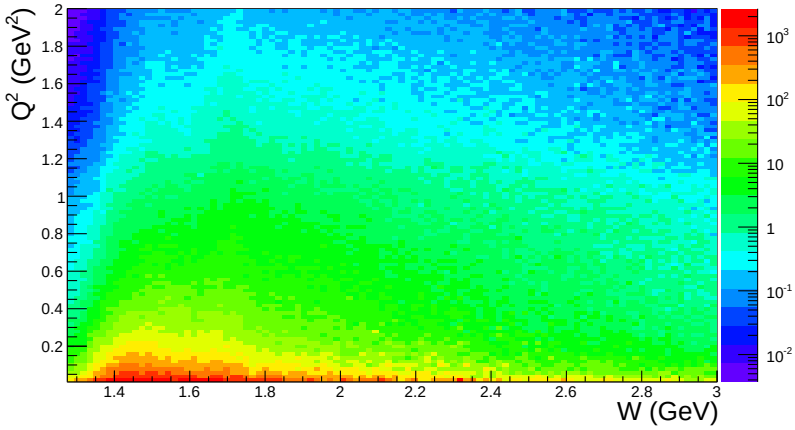

Figure 16: Q^2 versus W distribution for the generated $\pi^+\pi^- p$ events for E_b=6.6 GeV.

5.2 Acceptance Estimates for $ep \rightarrow e'p\pi^+\pi^-$

For the event reconstruction a simplified version of the CLAS12 event reconstruction software called FASTMC was employed to filter the generated events to determine the CLAS12 acceptance. The accepted $\pi^+\pi^- p$ events in Q^2 vs. W are shown in Fig. 17 at E_b=6.6 GeV and 8.8 GeV for the torus current set to $I = +3375$ A, which forces negatively charged particles to bend toward the beamline. Similar to the results obtained in Section 4.3, areas of zero acceptance can be seen in the plots, representing the gap between the Forward Tagger and the minimum polar angle accepted in the CLAS12 Forward Detector calorimeters. For the hybrid baryon search, the area of small photon virtuality is of particular interest. The size of the gap depends on the torus current setting and the momentum of the scattered electrons. For a negative torus current, i.e. outbending electrons, the gap is simply given by the geometrical acceptance of CLAS12 and is largely independent of the particle momentum, while for inbending particles the acceptance depends on scattering angle, particle momentum, and magnetic field strength. The acceptance for electron scattering angles from 2.5° to 4.5°, which is covered by the FT, is independent of the torus current settings. A simulated $ep \rightarrow e'p\pi^+\pi^-$ event in CLAS12 using the GEANT-4 simulation suite GEMC [73] is shown in Fig. 18.

With a beam energy of 6.6 GeV, the influence of the magnetic field polarity on the accessible kinematic coverage for $\pi^+\pi^- p$ electroproduction was further studied. The Q^2 versus W distributions for reconstructed $\pi^+\pi^- p$ events are shown in Fig. 19 for torus settings of $I = +3375$ A and $I = -3375$ A. A wide area of zero acceptance for the positive torus polarity setting of $I = +3375$ A is clearly seen in Fig. 19 (left). Reversing the magnetic field allows us to substantially decrease the inefficient area, as shown in Fig. 19 (right). Therefore, as anticipated in Section 4.3, the reversed magnetic field setting represents the best configuration for the proposed experiment.

We also examined the evolution of counting rates as a function of the magnetic field strength. The Q^2 versus W distributions for the accepted $\pi^+\pi^- p$ events are shown in Fig. 20 for torus currents $I = -3375$ A (left) and $I = -1500$ A (right). Comparing the reconstructed event rates shown in Fig. 20, we expect the counting rate to increase by almost a factor of two at half strength of the magnetic field because of the improved acceptance for the detection

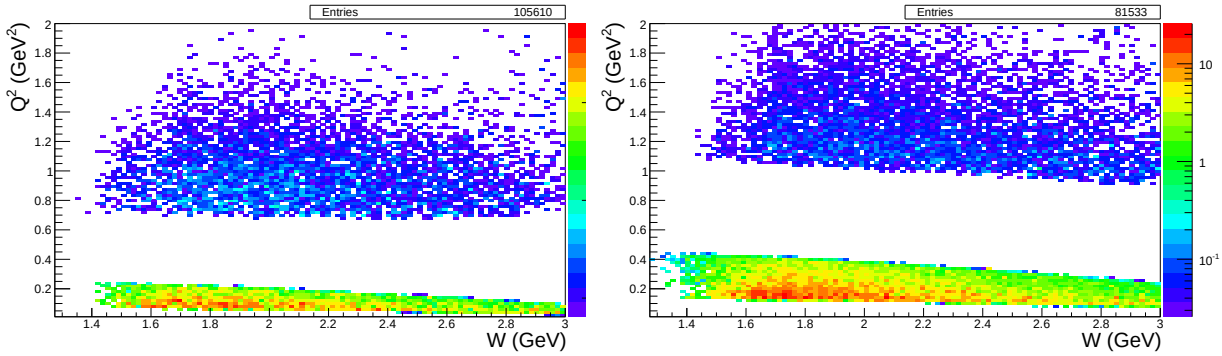

Figure 17: Q^2 versus W distributions for the reconstructed $\pi^+\pi^-p$ events (all particles in final state are registered). The left and right plots correspond to E_b=6.6 GeV and 8.8 GeV, respectively. The torus current is set to $I = +3375$ A.

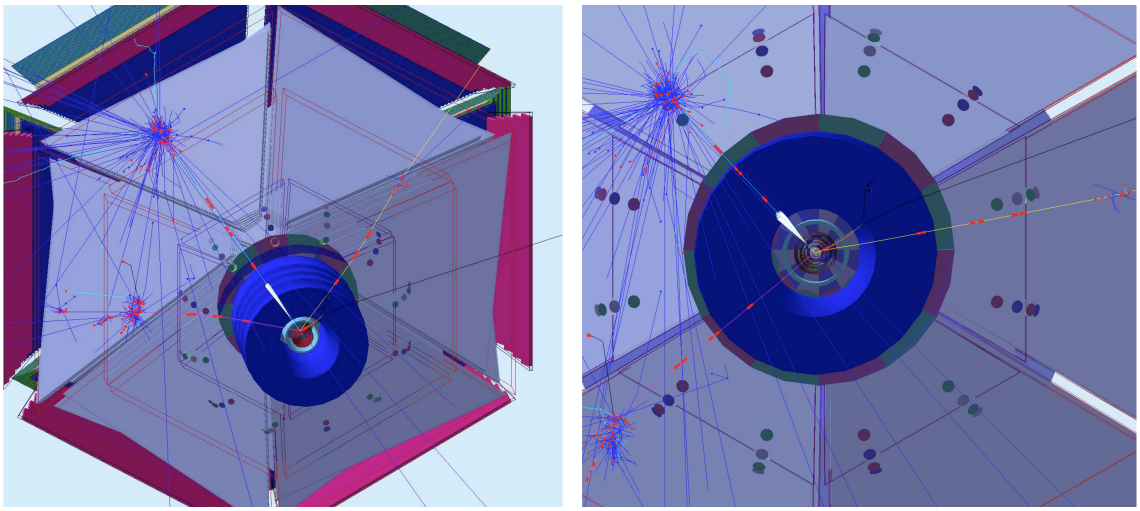

Figure 18: A GEANT-4 $ep \rightarrow e'p\pi^+\pi^-$ event as seen in CLAS12. (Left) The scattered electron (cyan) generates Cherenkov light in the HTCC, leaves track segments in the 3 drift chamber regions, hits in the FTOF planes, and finally showers in the PCAL & EC calorimeters. The two pions π^+ (purple line) and π^- (yellow line) are tracked in the DCs and leave hits in the FTOFs and calorimeters. The proton (short orange line) is tracked at large angles inside the solenoid magnet in the four SVT regions and leaves hits in the CTOF. (Right) A close-up view of the same event from a different angle. The torus magnet in this illustration was set at 50% of full current.

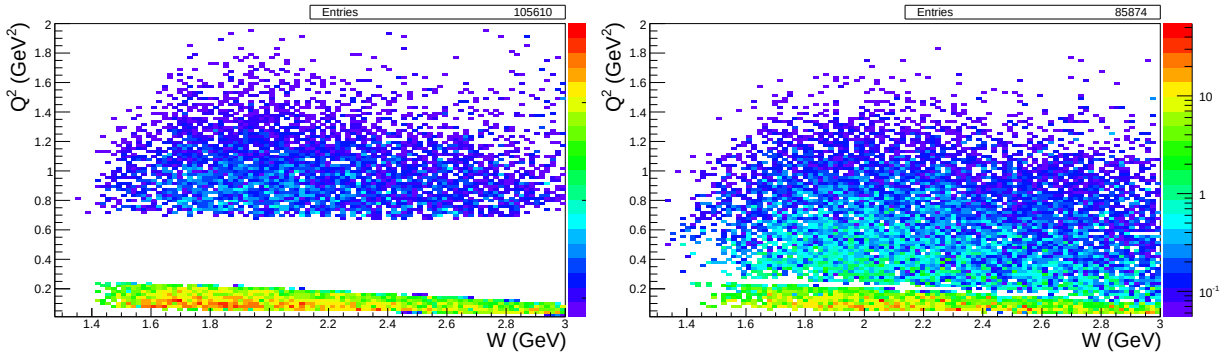

Figure 19: Q^2 versus W distributions at E_b=6.6 GeV for reconstructed $\pi^+\pi^-p$ events (all particles in final state are registered) for torus settings of $I = +3375$ A (left) and $I = -3375$ A (right). The reversed magnetic field closes the gap between the Forward Tagger and the CLAS12 Forward Detector calorimeters.

of all three particles (π^+, π^-, p) in the final state and the scattered electron. On the other hand, decreasing the torus current will negatively affect the charged particle momentum resolution, so the maximum negative torus current is optimal for this proposal.

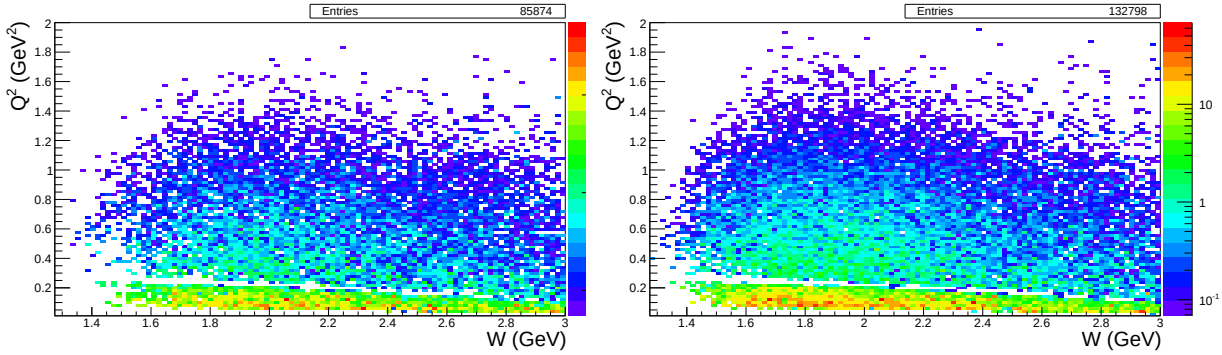

Figure 20: Q^2 versus W distributions at E_b=6.6 GeV for reconstructed $\pi^+\pi^-p$ events (all final state particles are registered) for torus settings of $I = -3375$ A (left) and $I = -1500$ A (right). With lower torus current more events are reconstructed.

5.3 Hadronic Mass Reconstruction for $ep \to e'p\pi^+\pi^-$

The hadronic mass resolution is of particular importance in studies of excited nucleon states, since this quantity determines the ability to reliably extract the resonant contributions in exclusive cross sections. For a credible separation between the resonant and the non-resonant contributions, the resolution in W should be much smaller than the N^* decay width. Typical values for the decay widths of nucleon resonances with masses > 2.0 GeV are in the range from 250 MeV to 400 MeV. Hence a mass resolution of ≈ 30 MeV is sufficient for the reliable isolation of contributions from hybrid baryons that are expected in the mass range from 2.0 GeV to 3.0 GeV. The resolution in W for the reconstructed $\pi^+\pi^-p$ events was studied

by computing for each reconstructed event the difference between the exact W_{gen} and the reconstructed W_{rec}. We compared two different ways of determining the invariant mass of the final hadronic system: a) from the difference between the four-momenta of the initial and the scattered electrons that is added to the four-momentum of the target proton (electron scattering kinematics) and b) from the sum of the four-momenta of the final state π^+, π^-, and p (hadron kinematics). The reconstructed $W_{gen} - W_{rec}$ event distributions provide the necessary information on the invariant mass resolution.

The aforementioned distributions for the electron scattering and hadron kinematics are shown in Fig. 21. The beam energy is set to 6.6 GeV and the torus current to $I = -3375$ A. For both ways of determining W_{rec}, the resolution over the full W range is better than 30 MeV and sufficient for the separation of the resonant and non-resonant contributions. If W_{rec} is computed from the hadron kinematics, the resolution is significantly better than in the case of the electron scattering kinematics. However, the hadron kinematics requires the registration of all final state hadrons with a detection efficiency lower than in the inclusive case where the value of W_{rec} is determined.

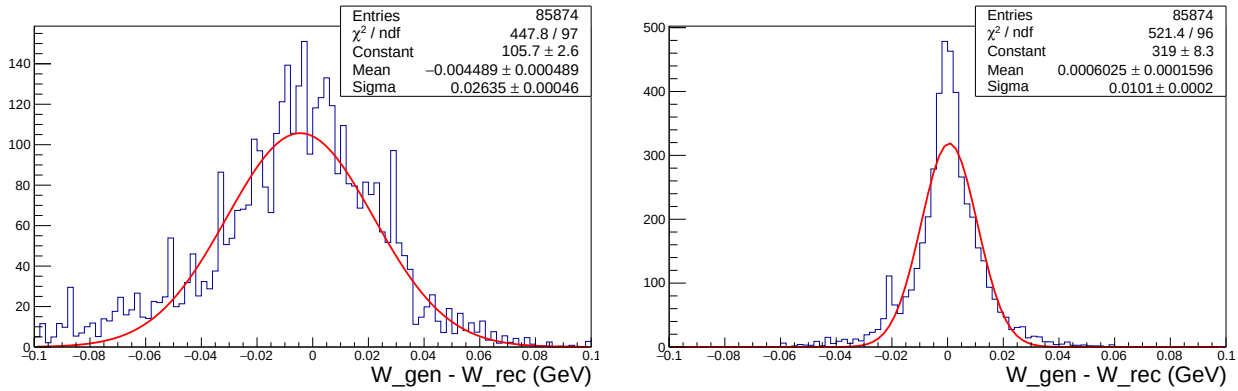

Figure 21: The $W_{gen} - W_{rec}$ distributions for $\pi^+\pi^-p$ events where W_{rec} is determined by electron scattering (left) and hadron (right) kinematics. See text for explanation of both kinematics.

The studies of charged double pion electroproduction with the CLAS detector [47, 56] demonstrated that the topology where the final π^- is not detected and its four-momentum is reconstructed from energy-momentum conservation provides the dominant part of the statistics. Hence topologies in which one of the final state hadrons is not detected will also provide the dominant statistics in the proposed experiment. We are planning to select the $\pi^+\pi^-p$ events by employing exclusivity cuts on the missing mass squared distributions of any of the final hadrons. The contribution from other exclusive channels (exclusive background) to the events within the exclusivity cuts was evaluated in the Monte Carlo simulation. Most of the exclusive background events come from the $ep \to e'p'\pi^+\pi^-\pi^0$ channel. Both $\pi^+\pi^-p$ and $\pi^+\pi^-\pi^0p$ events were generated for $W > 2$ GeV. The cross sections for the 2π and 3π channels were assumed comparable in this kinematic region. A phase space distribution is assumed for the 3π events. With this mixture of generated events, we reconstructed the $\pi^+\pi^-p$ events and determined their distribution over the relevant missing mass squared range for π^+ and π^-. The blue curves in Fig. 22 show the 2π event contributions and the green curves represent the 3π event contributions. The exclusivity cuts provide good isolation of

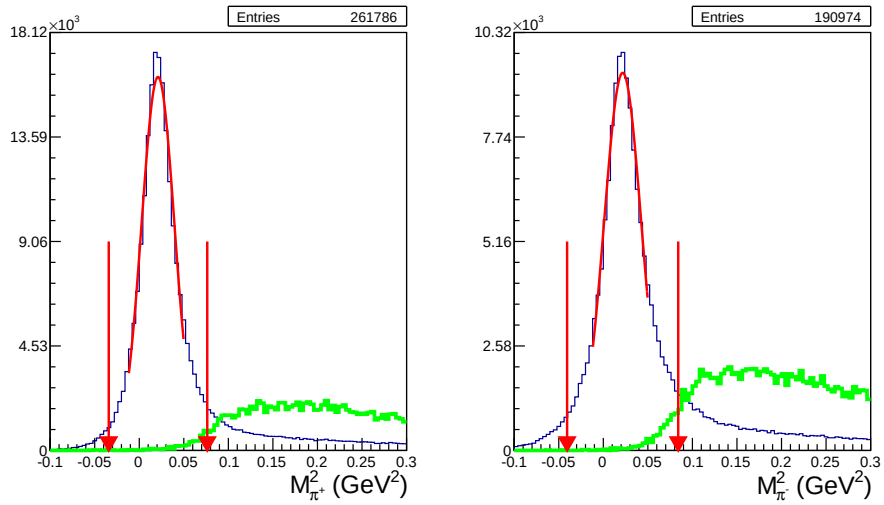

Figure 22: The reconstructed $\pi^+\pi^-p$ event distributions of the missing masses squared of π^+ (left) and π^- (right) for the generated $\pi^+\pi^-p$ events with an admixture of 3π events. The distributions were plotted for $W > 2$ GeV. The cross sections for the 2π and 3π channels were assumed comparable in this kinematic region. The contributions from the $\pi^+\pi^-p$ and the $\pi^+\pi^-\pi^0p$ events are shown in blue and green, respectively. The red arrows indicate the applied exclusivity cuts.

the $\pi^+\pi^-p$ events with the following contributions from the 3π events: $\sim 3\%$ for the missing π^+ topology and $\sim 4\%$ for the missing π^- topology.

5.4 Summary of $ep \to e'p\pi^+\pi^-$ Experimental Conditions Study

The summary of the run conditions studied in the $\pi^+\pi^-p$ simulations described above is given in Table 1. The bold rows correspond to the optimal set-up for the proposed experiment at E_b=6.6 GeV and 8.8 GeV with a torus setting of $I = -3375$ A. The columns labeled "Eff. %" represent the CLAS12 acceptance factors for different particles detected in the final state). The table also lists the minimum Q^2 possible. Finally the columns labeled $\sigma(W_e)$ and $\sigma(W_h)$ represent the hadron mass resolution for the electron scattering and hadron kinematics, respectively, detailed in Section 5.3.

The kinematic coverage in terms of the ϕ versus θ distributions for the final state hadrons is shown in Fig. 23 for all final state hadrons detected, a beam energy of 6.6 GeV, and a torus current $I = -3375$ A. The vertical strips at $\theta \sim 35°$ in all plots of Fig. 23 correspond to the detector gap between the CLAS12 Forward Detector and Central Detector. Since a reversed torus magnetic field was chosen, the low angle area is better populated for negatively charged particles (π^-).

Energy) (GeV)	Torus (A)	Eff. (%) all rec.	Eff. (%) π^+ miss	Eff. (%) π^- miss	Eff. (%) p miss	Q^2_{min} (GeV^2)	$\sigma(W_e)$ (MeV)	$\sigma(W_h)$ (MeV)
8.8	+3375	8.2	9.8	10.3	8.6	0.13	35	11
8.8	**-3375**	**8.3**	**12.7**	**10.6**	**12.1**	**0.13**	**33**	**10**
8.8	+1500	11.5	12.9	11.9	11.6	0.13	35	11
8.8	-1500	12.8	16.8	13.5	16.0	0.13	36	11
6.6	+3375	10.6	13.0	14.1	11.4	0.05	27	11
6.6	**-3375**	**8.7**	**13.8**	**11.5**	**13.1**	**0.05**	**26**	**10**
6.6	+1500	15.0	17.3	16.3	15.7	0.05	25	11
6.6	-1500	13.4	18.4	14.8	17.7	0.05	29	10

Table 1: Comparison of run conditions for the $\pi^+\pi^-p$ channel. The bold rows represent the optimal run conditions for E_b=6.6 GeV and 8.8 GeV with the torus setting of $I = -3375$ A.

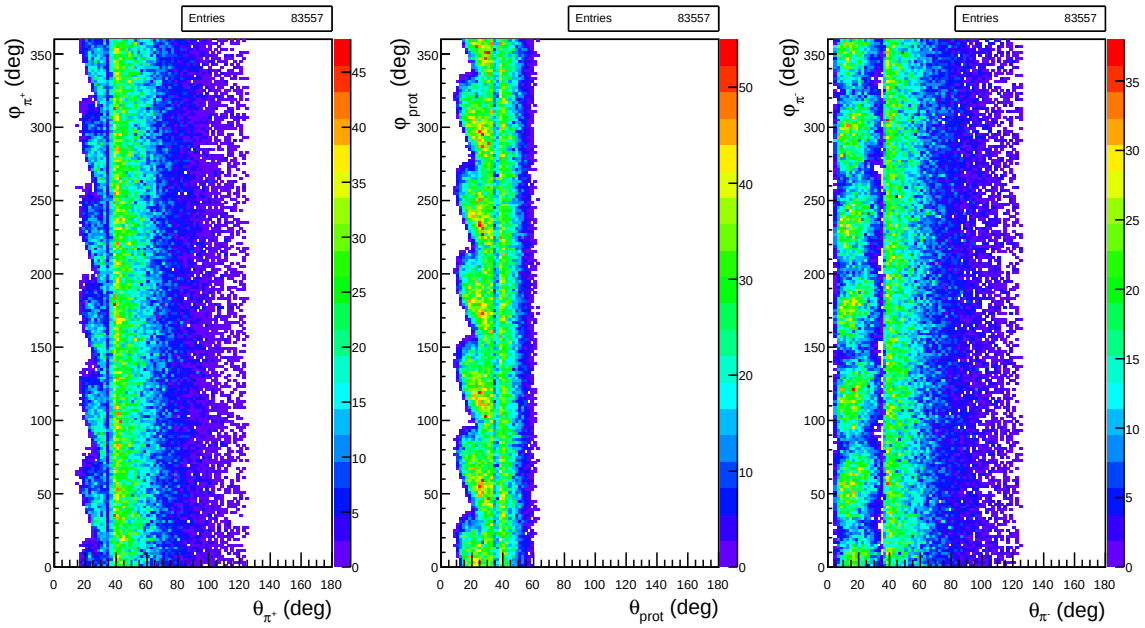

Figure 23: Laboratory ϕ vs θ distributions for the final state hadrons: π^+ (left), p (middle), and π^- (right).

6 Simulations for the $K^+\Lambda$ and $K^+\Sigma^0$ Final States

6.1 K^+Y Event Generator

The $ep \to e'K^+Y$ event generator is based on model cross sections. The models for the $K^+\Lambda$ [12] and $K^+\Sigma^0$ [58] channels describe KY electroproduction in the framework of a Regge-Plus-Resonance (RPR) approach developed by the Ghent group. The resonance contributions in the s-channel are described with the help of an effective-Lagrangian approach and the background part of the amplitude is modeled in terms of t-channel Regge-trajectory exchanges.

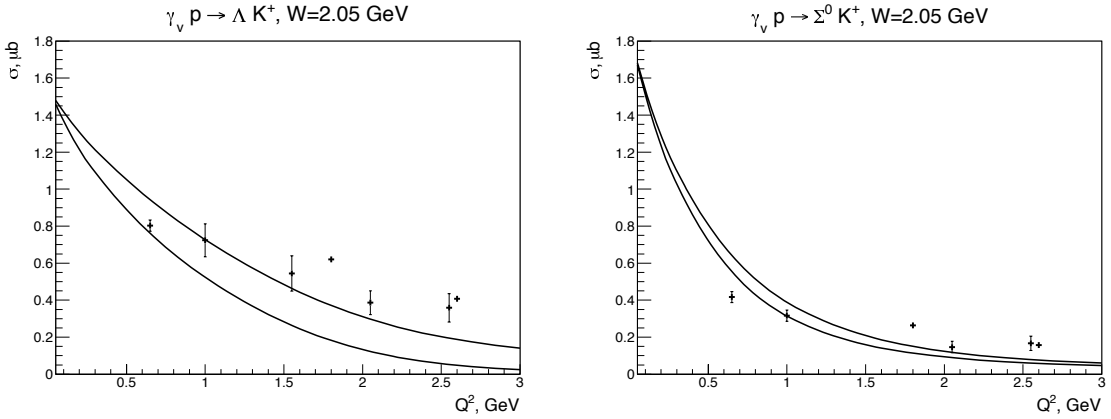

Figure 24: Integrated cross section for $K^+\Lambda$ (left) and $K^+\Sigma^0$ (right) from CLAS measurements as a function of Q^2 at $W = 2.05$ GeV [62, 64]. The cross sections at $Q^2 = 0.65$ GeV^2 are measured at a beam energy of 2.567 GeV and the cross sections at $Q^2 = 1.8$ GeV^2 and 2.6 GeV^2 are measured at a beam energy of 5.5 GeV. All other Q^2 points correspond to a beam energy of 4.056 GeV. The RPR model calculations [12, 58] are shown for E_b=2.567 GeV (upper curve) and E_b=5.5 GeV (lower curve).

A comparison of the fully integrated model cross section with data from CLAS is shown in Fig. 24. The cross sections are presented as a function of Q^2 for a given W bin centered at $W = 2.05$ GeV. The differential cross sections for representative bins of Q^2 and W are shown in Figs. 25 and 26. The model reproduces the experimental data for 0.65 GeV^2 $< Q^2 <$ 1.5 GeV^2, while it considerably underestimates the cross section for $Q^2 >$ 1.5 GeV^2. This underestimation is especially notable in the $K^+\Sigma^0$ channel for high Q^2 and low W. This discrepancy is not of serious concern since kinematic region of interest for this proposal is at low Q^2. However, we do have to rely solely on a model for the low Q^2 K^+Y cross sections as there are no experimental data available below Q^2=0.65 GeV^2. We can see in Figs. 25 and 26 that the model reasonably reproduces the general features of the sharp cross section growth at large $\cos\theta_K$ for $Q^2 >$ 1.5 GeV^2 and $W >$ 2.0 GeV. The data included in Figs. 25 and 26 are CLAS results from Refs. [62, 64]. The RPR model predictions shown here are based on the RPR-2011 version for the $K^+\Lambda$ final state and the RPR-2007 version for the $K^+\Sigma^0$ final state. More detailed comparisons of these models with the available CLAS data for the differential cross sections, separated structure functions, and induced and transferred polarizations are given in Refs. [60, 61, 62, 63, 64].

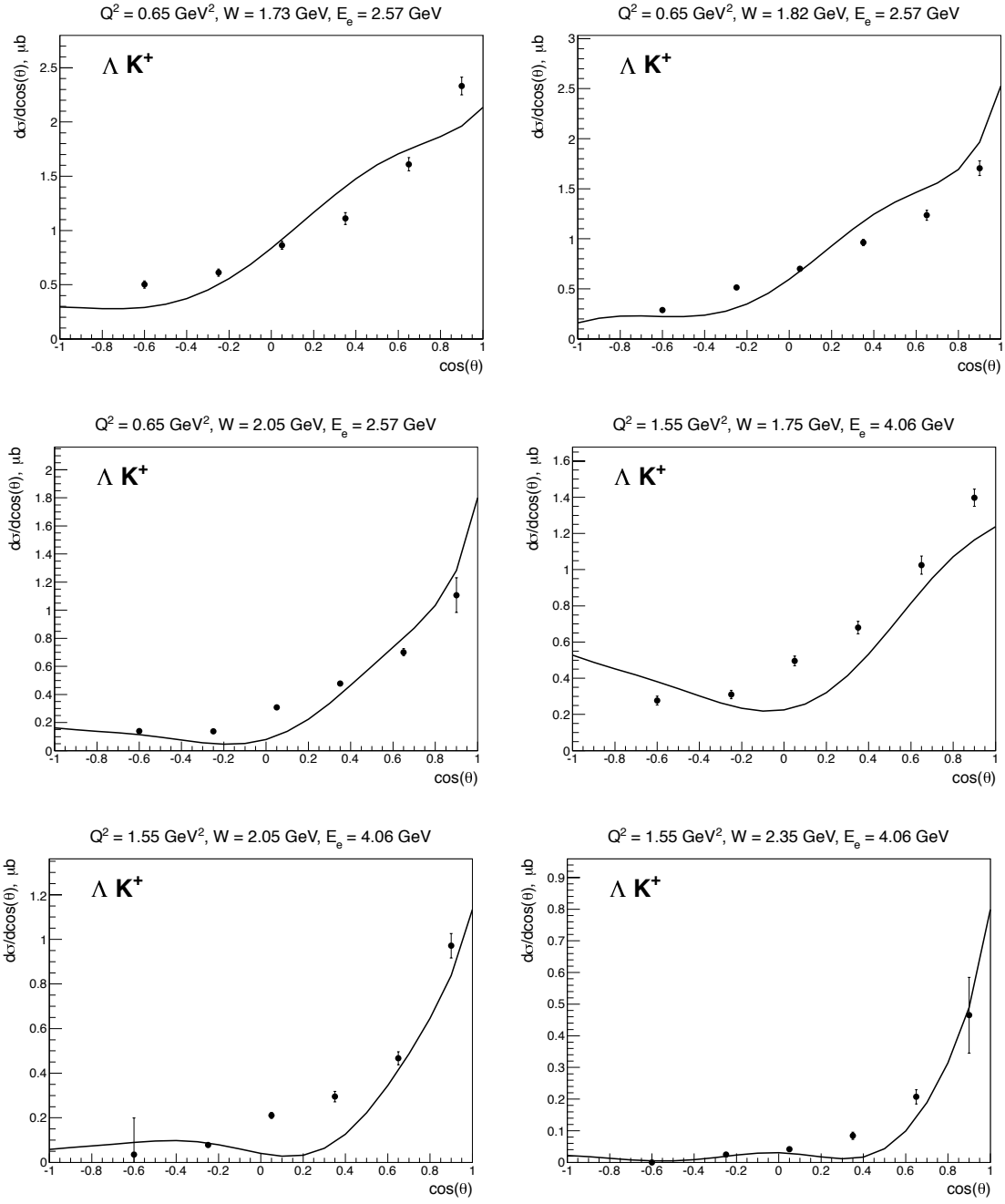

Figure 25: Differential cross sections for the $K^+\Lambda$ channel as a function of $\cos\theta_K$ from CLAS measurements in various Q^2 and W bins for two beam energies (E_b=2.57 GeV and 4.06 GeV) [62, 64] compared to the RPR-2011 model predictions [12].

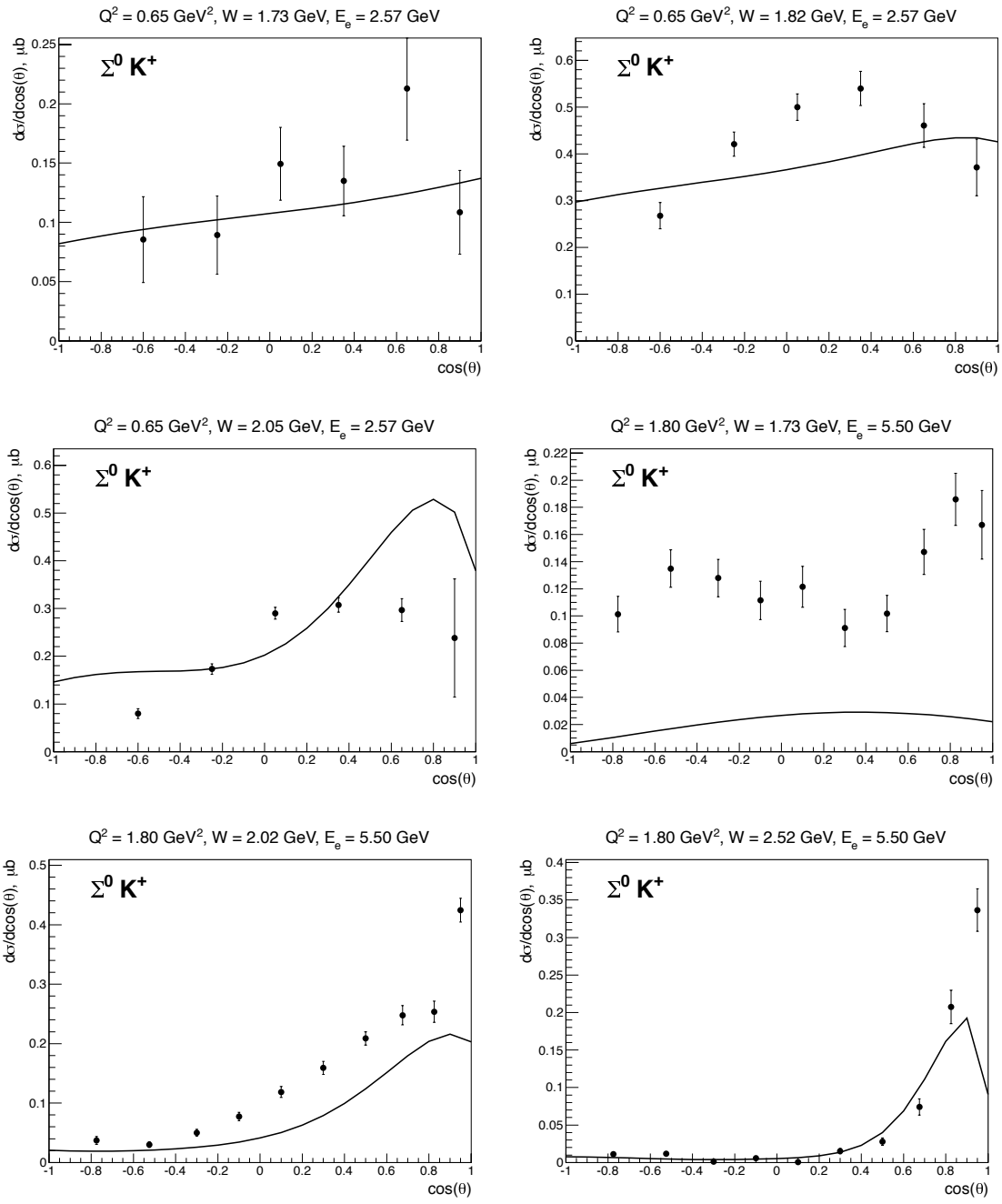

Figure 26: Differential cross sections for for $K^+\Sigma^0$ channel as a function of $\cos\theta_K$ from CLAS measurements in various Q^2 and W bins for two beam energies (E_b=2.57 GeV and 5.5 GeV). [62, 64] compared to the RPR-2007 model predictions [58].

6.2 Acceptances for $ep \rightarrow e'K^+\Lambda$

In Figs. 27 and 28 we compare the angular distributions of all final state particles for E_b=6.6 GeV obtained with a torus current of $I = +3375$ A to those with $I = -3375$ A. We see qualitatively the same behavior for the K^+Y distributions as for the $p\pi^+\pi^-$ final state (see Fig. 23), namely that outbending electrons generated in a W interval from the $K^+\Lambda$ threshold at 1.6 GeV to 3.5 GeV and scattering angles $\theta_e \geq 2^\circ$ are detected in the FT and then in the CLAS12 Forward Detector calorimeters starting at about 5°. Fig. 28 shows that the acceptances for outbending electrons result in a significantly reduced polar angle gap between the FT and the CLAS12 Forward Detector calorimeters compared to the acceptances for inbending electrons shown in Fig. 27. As a result, the event acceptance for this configuration is almost a factor of two larger than for the inbending field configuration. We also note that for both configurations there exists a polar-angle band at $\theta \approx 35^\circ$ where the acceptance is depleted due to the partially blind transition region between the CLAS12 Forward and Central Detector systems. The twisting pattern seen in the accepted p and K^+ plots is due to the azimuthal motion of the charged tracks in the strong central solenoid field that generates an azimuthal "kick" that depends on the production angle and particle momentum. The pattern for the π^- is different as they have on average much lower momenta and their migration in ϕ is larger and more diffuse.

6.3 Run Conditions

We are proposing to search for hybrid states at low Q^2, where the accessible range of Q^2 depends on the beam energy and torus current. Another issue that affects the selection of the optimal run condition is that we need good particle momentum resolution to be able to separate the $K^+\Lambda$ and $K^+\Sigma^0$ electroproduction channels and the best resolution is achieved with larger torus currents. The $K^+\Lambda$ and $K^+\Sigma^0$ channel separation is based on cuts on the reconstructed $e'K^+$ missing mass. For this purpose the final state K^+ must be detected. The detection of the p or π^- from the Λ decay is required in order to measure the induced and transferred polarizations of the hyperons. Thus, we have to use topologies where the final state electron, the K^+, and at least one of the other hadrons (p or π^-) is detected. Previous measurements of these hyperon polarization components extracted from CLAS data are given in Refs. [59, 60].

The run condition studies were performed with the CLAS12 FASTMC program. Table 2 summarizes the minimum Q^2 coverage for the K^+Y final states at E_b=6.6 GeV and 8.8 GeV for different torus field settings and polarities. As already mentioned in Section 4.3, the optimal running conditions correspond to data collection with a large negative torus current, where the maximal $K^+\Lambda$ and $K^+\Sigma^0$ separation is achieved and the gap in the Q^2 coverage between the FT and the CLAS12 Forward Detector calorimeters is the smallest. Studies of the reconstructed $e'K^+$ missing mass combining the data for the $K^+\Lambda$ and $K^+\Sigma^0$ channels for different beam energies and different torus field and polarity conditions are shown in Figs. 29 and 30. Clearly the data collection at the highest possible torus field settings, corresponding to the best charged particle momentum resolution, is optimal for separation of the KY reaction channels.

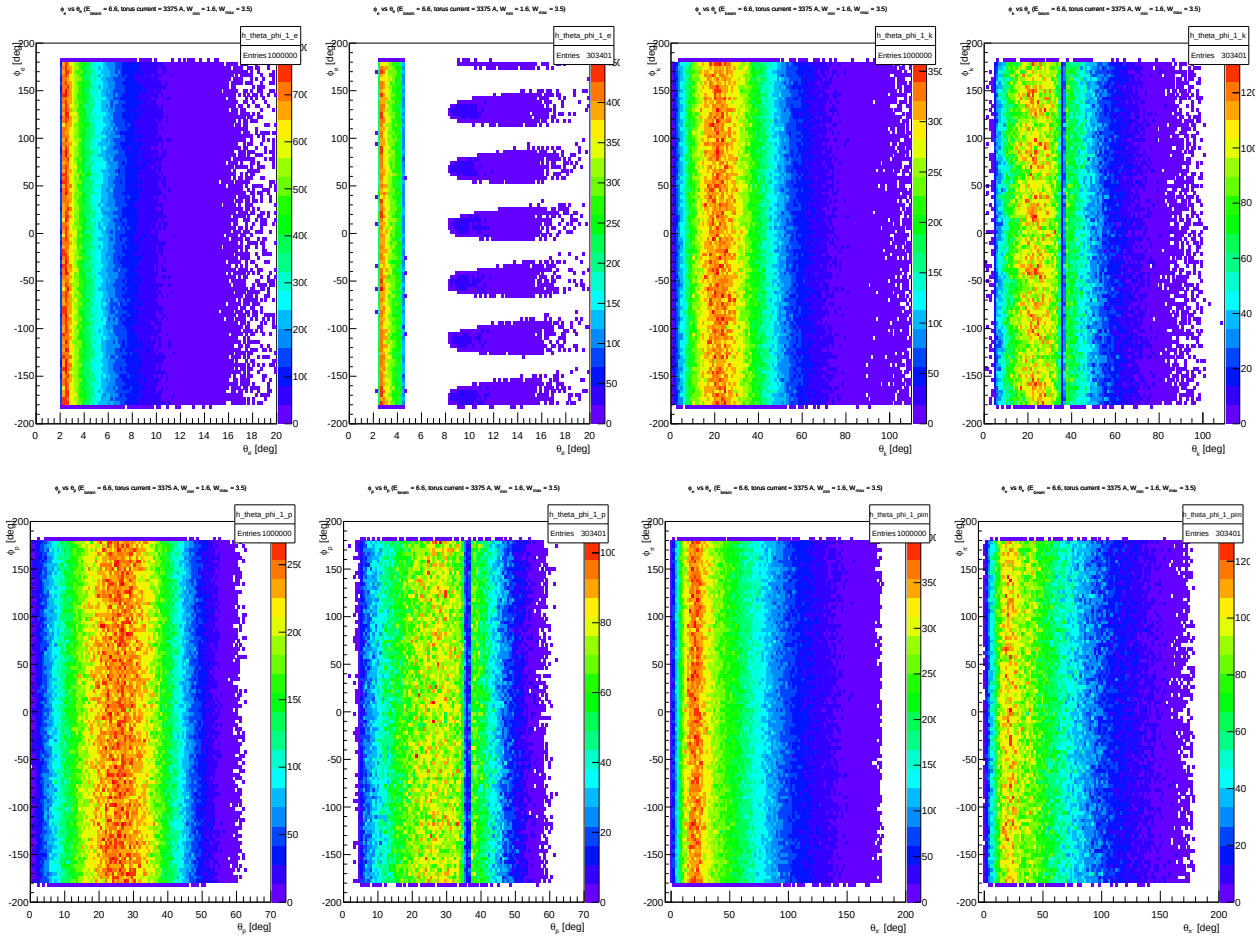

Figure 27: Azimuthal versus polar angles of generated (first, third columns) and accepted events (second, fourth columns) for electrons (upper left), K^+ (upper right), p (lower left), and π^- (lower right). The events were generated for E_b=6.6 GeV in a W range from 1.6 GeV to 3.5 GeV. The torus current was set to I = +3375 A, which bends negatively charged particles inward toward the beamline.

E_b, GeV	Torus Current, A	Q^2_{min}, GeV^2
6.6	+1500	0.05
6.6	−1500	0.05
6.6	+3375	0.05
6.6	**−3375**	0.05
8.8	+1500	0.1
8.8	−1500	0.1
8.8	+3375	0.1
8.8	**−3375**	0.1

Table 2: Minimal achievable Q^2 (Q^2_{min}) for different torus currents and polarities at E_b=6.6 GeV and 8.8 GeV for the $K^+\Lambda$ and $K^+\Sigma^0$ final states.

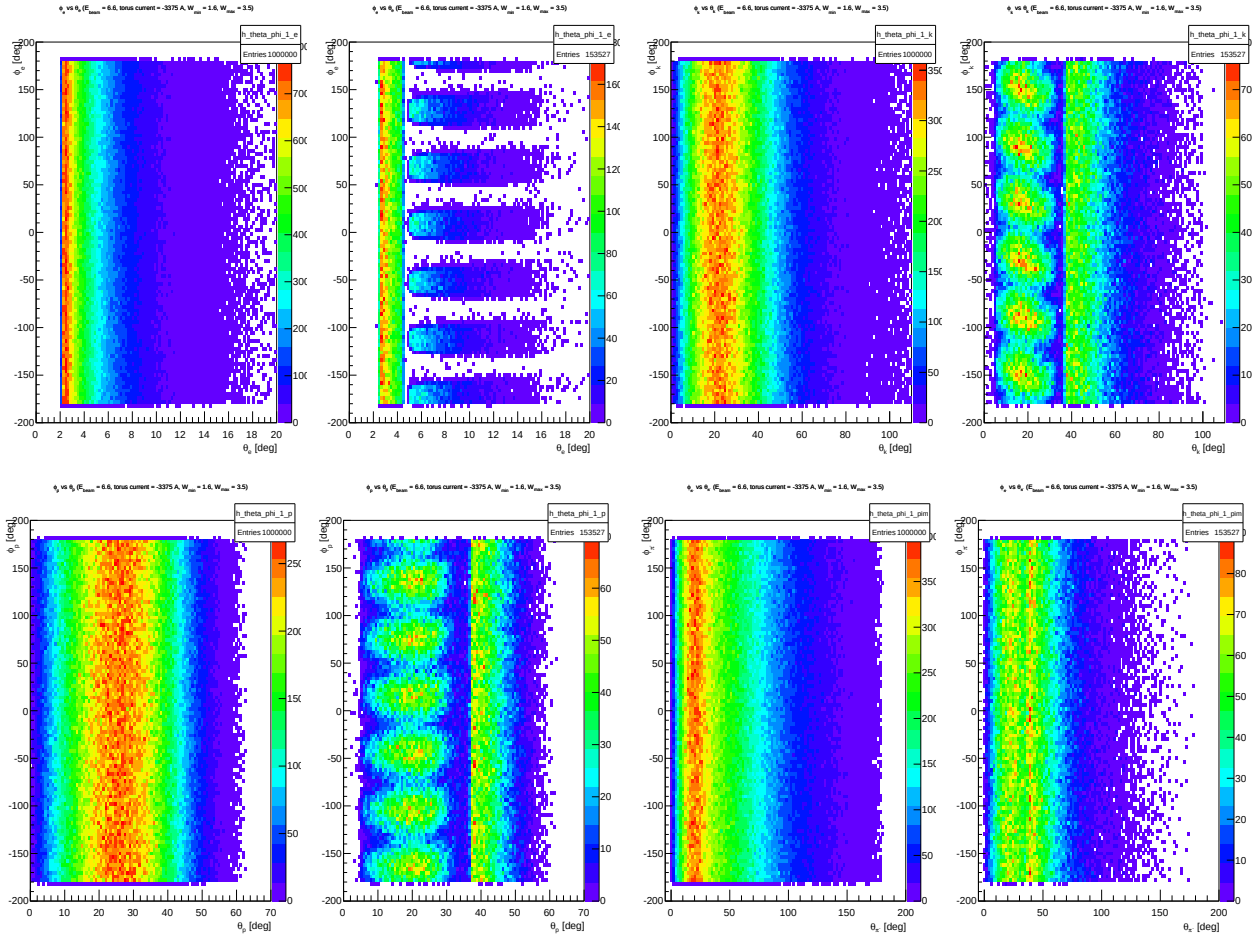

Figure 28: Azimuthal versus polar angles of generated (first, third columns) and accepted events (second, fourth columns) for electrons (upper left), K^+ (upper right), p (lower left), and π^- (lower right). The events were generated for E_b=6.6 GeV in a W range from 1.6 GeV to 3.5 GeV. The torus current was set to $I = -3375$ A, which bends negatively charged particles away from the beamline.

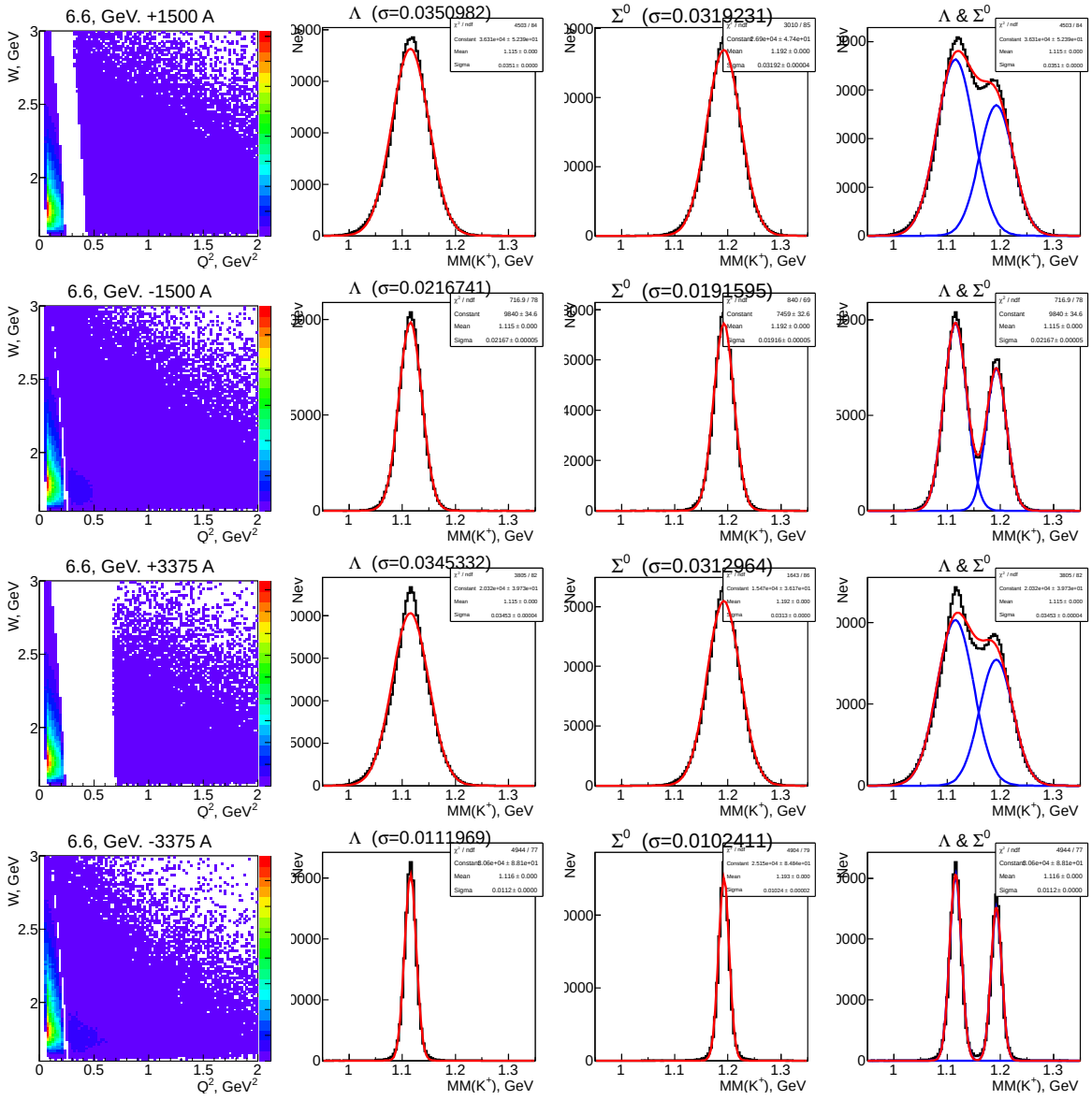

Figure 29: The left column shows the W versus Q^2 distributions at different torus currents for $Q^2 < 2$ GeV^2 for E_b=6.6 GeV. The next three columns show the distributions of the $e'K^+$ missing mass for the different torus currents. The right column shows the combined $K^+\Lambda$ and $K^+\Sigma^0$ overlap histograms (no background included) demonstrating the advantage of high CLAS12 torus currents.

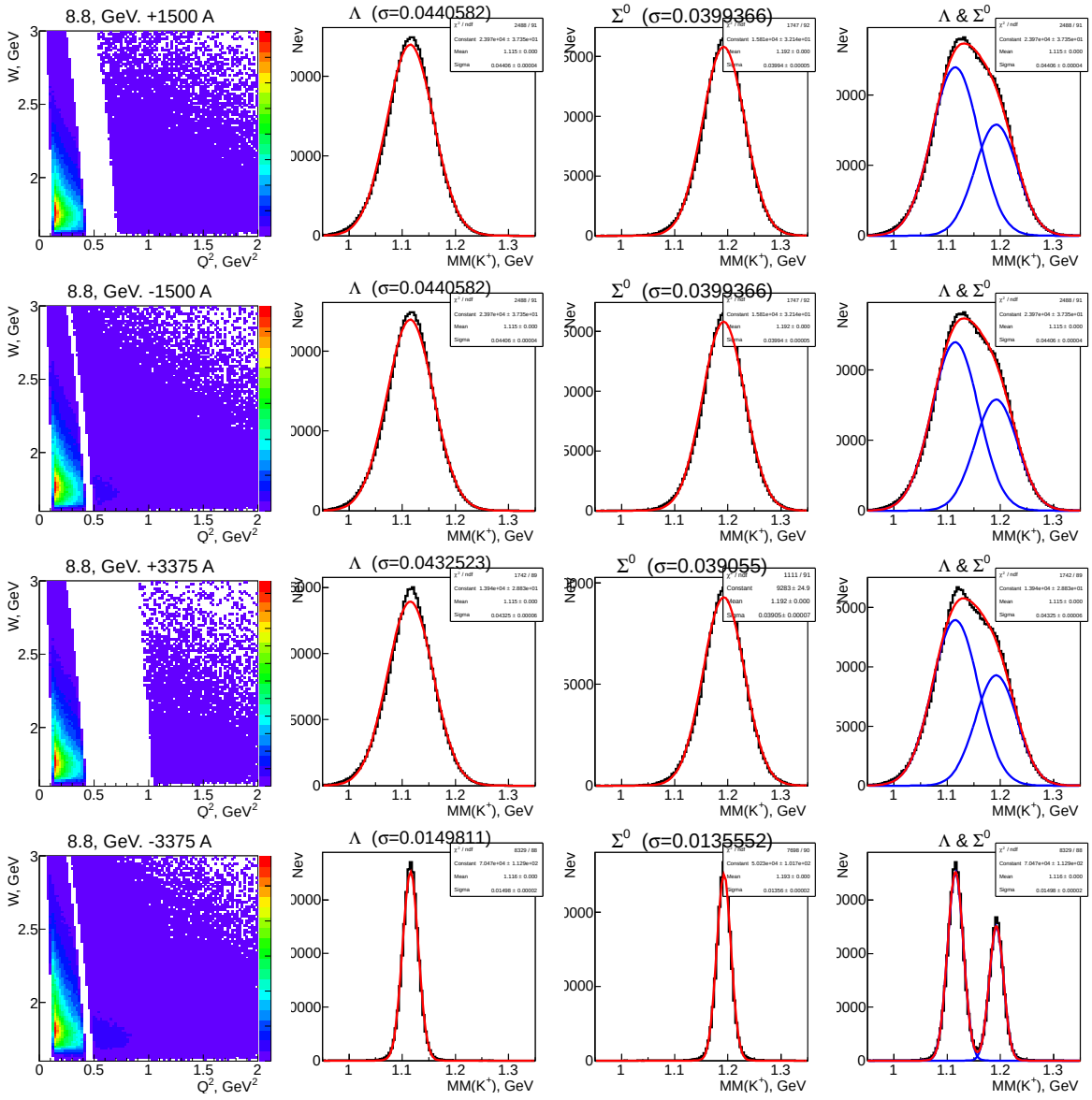

Figure 30: The left column shows the W versus Q^2 distributions at different torus currents for $Q^2 < 2$ GeV^2 for E_b=8.8 GeV. The next three columns show the distributions of the $e'K^+$ missing mass for the different torus currents. The right column shows the combined $K^+\Lambda$ and $K^+\Sigma^0$ overlap histograms (no background included) demonstrating the advantage of high CLAS12 torus currents.

6.4 Count Rates for K^+Y

The expected total number of K^+Y electroproduction events in the reaction $ep \to e'K^+Y$ can be written as:

$$N = \mathcal{L} \cdot t \cdot \int \frac{d^5\sigma}{dE_e d\Omega_e d\Omega_K} dE_e d\Omega_e d\Omega_K, \tag{1}$$

where

- $\mathcal{L} = 1 \times 10^{35}$ cm^{-2}s^{-1} is the expected CLAS12 operating luminosity
- t is the expected run time, and
- $\frac{d^5\sigma}{dE_e d\Omega_e d\Omega_K}$ is the cross section from Eq.(23) in Appendix A.

The integration in Eq.(1) is performed over the entire kinematic space and the event rate R is defined as $\frac{N}{t}$.

The integration in Eq.(1) can be done numerically. We use the same model cross sections for $d^2\sigma/d\Omega_K^*$ as was used in the event generator (see Section 6.1). The minimum achievable value of Q^2 in CLAS12 is determined by the forward hole, where high energy electrons cannot be detected. For both beam energies Q^2 is greater than 0.05 GeV^2 (see Table 2), so we can integrate in Eq.(1) given that $Q^2 > 0.05$ GeV^2. The calculated event rates R_Λ and R_{Σ^0} are presented in Table 3.

E_{beam}, GeV	R_Λ, Hz	R_{Σ^0}, Hz
6.6	1500	1200
8.8	1400	1100

Table 3: Estimated production rates for events with $Q^2 > 0.05$ GeV^2.

To account for the acceptance of CLAS12, a detailed simulation is needed. As we need to generate events in the entire kinematic space with $Q^2 > 0.05$ GeV^2, the ratio of reconstructed to generated events gives the averaged acceptance. Multiplying the event rates from Table 3 by that ratio, we obtain the event rates that account for the CLAS12 acceptance. An $ep \to e'K^+\Lambda \to e'K^+p\pi^-$ event is considered to be reconstructed if the electron and at least two hadrons have been detected. A trigger condition requiring at least two charged hadrons and an electron would select our channels of interest.

The accepted event rate calculations are presented in Table 4 for different torus currents and polarities for E_b=6.6 GeV and 8.8 GeV, taking into account the branching ratio for the Λ decay into $p\pi^-$ (64%). A rough estimate suggests that the KY exclusive channel contribution is about 1% with respect to the two and three pion events, which are expected to dominate the events that have an electron and at least two charged hadrons in the final state. The maximal total event rate is therefore expected to be $\approx$ 25 kHz for the trigger condition described above.

E_{beam}, GeV	Torus Current A	R_Λ, Hz
6.6	+1500	144
6.6	-1500	154
6.6	-3375	91
8.8	+1500	108
8.8	-1500	108
8.8	-3375	58

Table 4: Estimated event rates for the $ep \to e'K^+\Lambda \to e'K^+p\pi^-$ channel for E_b=6.6 GeV and 8.8 GeV, and for different torus currents and polarities for the trigger condition where the electron and two hadrons are required to be detected in CLAS12.

6.5 Expected K^+Y Total Event Rates

At the very forward electron scattering angles, electron rates will be very high and may exceed the capabilities of the data acquisition system. Therefore additional constraints are needed to define an optimal trigger configuration to enrich the sample with final state topologies that might be expected for the hybrid baryon candidates and to reduce the total acquisition rate. For our initial running program, we therefore consider a trigger for the hadronic final states with at least two charged particles. This will cover final states such as $K^+\Lambda \to K^+p\pi^-$, $p\pi^+\pi^-$, $p\phi \to pK^+K^-$, and $p\eta' \to p\pi^+\pi^-\eta$. For realistic rate estimates, projections of the hadronic coupling strengths of the hybrid baryons are needed, which are currently not available. In addition, a single charged hadron trigger will be incorporated with a pre-scaling factor for the FT, which in parallel will collect events with a single charged hadron in the final state, i.e. π^+n, $p\pi^0$, $K^+\Lambda$, and $K^+\Lambda$, among others.

The nominal operating luminosity of CLAS12 is expected to be $\mathcal{L} = 1 \times 10^{35}$ cm^{-2}s^{-1}. This corresponds to a production rate of 70 Hz (for $K^+\Lambda$) and about 50 Hz (for $K^+\Sigma^0$) for E_b=6.6 GeV at a torus current of $I = -3375$ A. For a 50 day run at the nominal luminosity, the total number of $K^+\Lambda$ events is estimated to be 3.0×10^8 and the number of $K^+\Sigma^0$ events to be 2.2×10^8. The lowest event rate is expected for high Q^2 and high W. For the kinematics with the lowest statistics, e.g. $2.0 \leq Q^2 \leq 2.5$ GeV^2 and $2.675 \leq W \leq 2.700$ GeV, a total number of 3.3×10^5 $K^+\Lambda$ events and 1.8×10^5 $K^+\Sigma^0$ events is expected. While these rates seem to be very large, it is shown in Section 7 and Section 8 that they are necessary for the positive identification of potential hybrid baryon states. This high statistics is thus essential, and the transverse and longitudinal photon polarization that is inherent in electron scattering will provide amplitude interference that could be expected to enhance the resonant signal.

7 Data Analysis and Quasi-Data

7.1 Event Selection

Electrons will be detected both in the Forward Tagger (FT) and in the CLAS12 Forward Detector (FD). Electrons measured in the FD can be identified at scattering angles above 5° in the High Threshold Cherenkov Counter (HTCC) and in the PCAL and EC calorimeters.

Due to the higher Q^2 for electrons detected at larger scattering angles in CLAS12 compared to the FT region, the FD electron rate is comparatively much lower than the hadronic rate, which ensures good electron identification. For electrons detected in the FT at low Q^2, the electron rate is very high and completely dominates the event rate in the FT calorimeter and hodoscope. To keep the trigger rate low enough to be compatible with the data acquisition capabilities, a coincidence between a signal in the FT and two hadrons in CLAS12 may be used in addition to the main CLAS12 trigger, where at least two charged particles are detected.

Charged hadrons ($\pi^{\pm}$, $K^{\pm}$, and p) will be tracked in the drift chambers and micromegas in the FD, and in the silicon tracker and barrel micromegas at large angles in the CD. At all angles, charged particle identification is provided in the CLAS12 time-of-flight detector systems. Photons and neutrons are detected at forward angles in the electromagnetic calorimeters (PCAL, EC, FT) and neutrons at large angles are detected in the Central Neutron Detector (CND).

7.2 Event Reconstruction

The event reconstruction software has been designed and developed to be deployed within the so-called `ClaRA` framework, a Service Oriented Architecture framework for data processing. The reconstruction software suite consists of a chain of services that can be deployed within `ClaRA`. The services for each detector component are compiled as java archive (JAR) plugins that are included in the complete CLAS12 software release package `coatjava`. The CLAS12 reconstruction software reconstructs, on an event-by-event basis, the raw data coming from either simulation or the detectors to provide physics analysis output such as track parameters and particle identification. The package provides scripts that can be launched on the farm to process the data, as well as a framework to do event analysis using the flexible scripting language `Groovy`. The documentation for the `coatjava` package can available on the CLAS12 webpage [74]. For acceptance and efficiency studies, events are generated using the GEANT-4 Monte Carlo simulation application GEMC. Detailed documentation of the detectors included in the simulation and of the various settings used to set the simulation parameters according to physics, backgrounds, and magnetic field configurations is available from the GEMC webpage [73]. An example of a simulated event for the reaction $ep \to e'K^+\Lambda$ is shown in Fig. 31.

The studies for this proposal were carried out using FASTMC. These studies will be redone when the reconstruction software and GEMC development are sufficiently advanced, which is anticipated before the end of summer 2016. However, comparisons of simulation studies carried out with the FASTMC program and the present version of the GEMC and reconstruction software package show more than reasonable correspondence. This comparisons provide us with confidence in the veracity of our acceptance and rate studies for this proposal.

7.3 Extracting Cross Sections and Normalized Yields

After the raw data have been subjected to the CLAS12 event reconstruction software package, we intend to extract differential cross section for all processes with two-body final states, e.g. KY, $N\pi$, $p\eta$, $p\eta'$, and $p\phi$, using the CLAS12 GEMC GEANT-4 Monte Carlo to fully

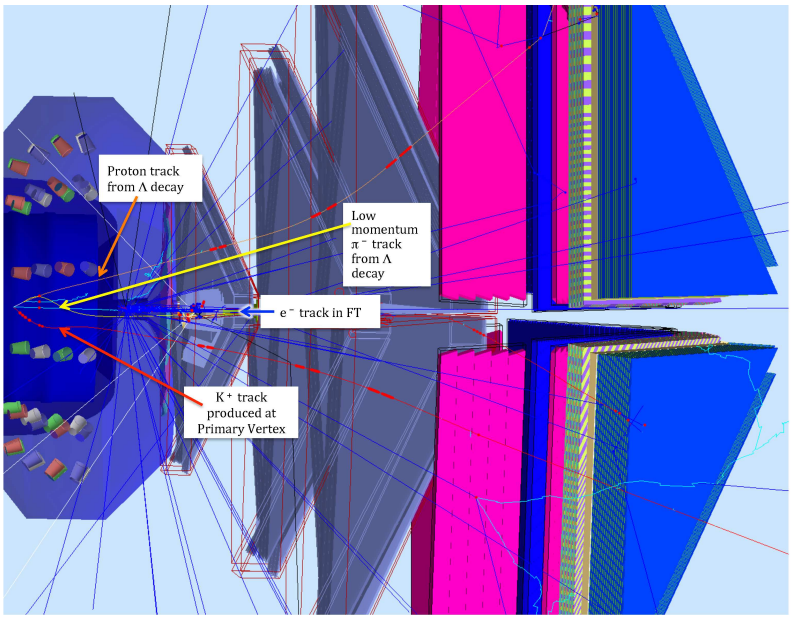

Figure 31: GEMC display of an $ep \to e'K^+\Lambda$ ($\Lambda \to p\pi^-$) event as seen in CLAS12.

understand the acceptances for these processes at the accuracy level required for the partial wave analysis. As for all electroproduction data, the raw cross sections will be subjected to radiative corrections in order to extract the final differential cross sections. The radiative correction procedure for exclusive processes is well established [75], and has been used in all of the analyses of the CLAS electroproduction cross sections. As it has been recently demonstrated [48], radiative corrections are very important for the analysis of exclusive processes in terms of resonance excitations as they affect both the polar and azimuthal angular dependencies. This is particularly important in the extraction of the separated U, LT, and TT structure functions from the differential cross sections involves a ϕ^* moment analysis (see e.g. Refs. [48, 62, 64]).

For the three-body final states, such as $p\pi^+\pi^-$ and $p\eta\pi^0$, in addition to extracting differential and integrated cross sections, we also will consider event-based analysis techniques, where the acceptances will be assigned to each event and acceptance weighted events will be subjected to a maximum-likelihood fitting procedure. This procedures preserves the full correlations among the final state particles.

7.4 Modeling Hybrid Baryon Contributions to KY and $\pi^+\pi^-p$

To prove the feasibility of our ability to observe hybrid baryons, we have studied the effect of implementing the contribution of the lightest hybrid state in the differential cross sections for exclusive $K^+\Lambda$, $K^+\Sigma^0$, and $\pi^+\pi^-p$ electroproduction off the proton. For the hybrid baryon mass range and spin-parity, we have considered Lattice QCD evaluations [6] that predict the lightest hybrid baryons in a mass range from 2.5 GeV to 2.7 GeV with spin-parity either $J^P = \frac{1}{2}^+$ or $J^P = \frac{3}{2}^+$ (see Fig. 1). However, these computations were carried out with a pion mass of 396 MeV. We have corrected the predicted hybrid baryon masses by employing mass shifts for states of both spin-parities towards smaller values, which can be expected when the physical pion mass will be reached. The mass shift for the lowest hybrid baryon

with $J^P = \frac{1}{2}^+$ spin-parity can be estimated by the difference between the LQCD result [6] for the mass of the lightest nucleon of spin-parity $J^P = \frac{1}{2}^+$ and the measured value of the proton mass, Δ_1=0.3 GeV. For the lowest hybrid state with $J^P = \frac{3}{2}^+$, the mass shift can be estimated by the differences between the mass of the lightest LQCD resonance with $J^P = \frac{3}{2}^+$ and the physical mass of the $N(1720)\frac{3}{2}^+$ four star resonance, Δ_2=0.5 GeV.

Therefore, we have modeled the hybrid baryon contributions considering states of spin-parity $J^P = \frac{1}{2}^+$ and $J^P = \frac{3}{2}^+$ in the mass range from 2.1 GeV to 2.3 GeV employing an average mass shift of 0.4 GeV. Eventually we used the central value of 2.2 GeV for the hybrid state mass. According to the RPP14 results [1] on the resonance parameters in the mass range around 2.0 GeV, we adopted for the hybrid baryon total decay width a range from 200 MeV to 300 MeV. For the hybrid branching ratio (BR) to KY we employed a value of 5%. Recent studies of the CLAS data on $\pi^+\pi^-p$ electroproduction [28] demonstrated that many of the nucleon resonances in the mass range above 1.6 GeV decay preferentially to the $N\pi\pi$ final state, with most having branching ratios to the $N\pi\pi$ final state above 40%. We therefore chose for the hybrid baryon branching ratio to the $N\pi\pi$ final state a value of 50%.

The differential cross sections without hybrid contributions (Model A) were computed from the amplitudes of the RPR model [12, 58] for the KY exclusive channels and from the JM model [11, 13, 28, 34, 68, 69] for the $\pi^+\pi^-p$ exclusive channel. Both models contain the contributions from four star resonances and the non-resonant mechanisms added-up coherently:

- in the case of the KY channel we considered as a reference the RPR model referred to as RPR-2011 [12, 76], in which the Reggeized non-resonant amplitudes and the contributions from the established N^* states have been used to describe both KY photo- and electroproduction. The RPR web-site [77] provides the full set of KY amplitudes and photo-/electroproduction observables off the proton.

- in the case of the $\pi^+\pi^-p$ channel, we considered the coherent superposition of 8 meson-baryon channels and direct 2π-production mechanisms described in Section 3.3 with the contributions to the $\pi\Delta$ and ρp meson-baryon channels from all four star resonances with observed decays to the $N\pi\pi$ final state [11, 13, 28, 34, 68, 69]

In the evaluation of the cross sections accounting for the hybrid contribution (Model B), the hybrid resonance amplitude was added coherently to the aforementioned amplitudes of KY and $\pi^+\pi^-p$ electroproduction. The full amplitudes of the KY and $\pi^+\pi^-p$ exclusive channels $\langle\lambda_f|\, T^B\, |\lambda_\gamma\lambda_p\rangle$ in Model B were evaluated as:

$$\langle\lambda_f|\, T^B\, |\lambda_\gamma\lambda_p\rangle = \langle\lambda_f|\, T^A\, |\lambda_\gamma\lambda_p\rangle + F_{conv}\, \langle\lambda_f|\, T^r\, |\lambda_\gamma\lambda_p\rangle\,, \tag{2}$$

where the $\langle\lambda_f|\, T^A\, |\lambda_\gamma\lambda_p\rangle$ matrix element represents the full Model A amplitudes without hybrid contribution, while the hybrid contribution was described by the resonant amplitude $\langle\lambda_f|\, T^r\, |\lambda_\gamma\lambda_p\rangle$. The amplitudes were computed in the helicity representation with the helicities of the initial virtual photon and proton λ_γ and λ_p, and the final state helicity λ_f determined in the CM frame, as well as the four momenta of the final hadrons and the initial virtual photon and proton.

The relations between the model amplitudes and the cross sections for the KY and $\pi^+\pi^-p$ channels can be found in Refs. [12, 58] and Ref. [11], respectively. However, the resonant

amplitudes described below for the hybrid contributions were obtained in the conventions of the JM model that relate the $\pi^+\pi^- p$ amplitudes to the cross sections. Therefore in the case of the KY cross section evaluation within the RPR model, the $\langle\lambda_f|\, T^r\, |\lambda_\gamma\lambda_p\rangle$ resonant contributions from the hybrid should be converted to the convention of the RPR model that relate the RPR model amplitudes to the cross sections. This was achieved by employing the conversion factor F_{conv} in Eq.(2). The F_{conv} conversion factor from the JM model to the RPR model was evaluated by making an identity between the cross sections computed in both models:

$$F_{conv} = \sqrt{4\pi\alpha}, \tag{3}$$

where α=$\frac{1}{137}$. This factor is employed in the computations of the KY differential cross sections within the RPR model, while in the computation of the $\pi^+\pi^- p$ differential cross sections within the framework of the JM model, the factor F_{conv} is equal to unity.

The contributions from the hybrid baryon were parameterized employing the unitarized Breit-Wigner ansatz developed in Ref. [13]. For simplicity here we restrict ourselves to consideration of the Breit-Wigner ansatz for the KY final states treating the final hadrons as stable particles. The description of the Breit-Wigner ansatz used in the simulation of the $\pi^+\pi^- p$ channel accounting for the formation and decays of unstable $\pi\Delta$ and ρp intermediate states can be found in Ref. [13]. As discussed in Ref. [13], for just one contributing resonance, the unitarized Breit-Wigner ansatz can be simplified as:

$$\langle\lambda_f|\, T^r\, |\lambda_\gamma\lambda_p\rangle = \frac{\langle\lambda_f|\, T_{dec}\, |\lambda_R\rangle\, \langle\lambda_R|\, T_{em}\, |\lambda_\gamma\lambda_p\rangle}{M_r^2 - W^2 - i\Gamma_r M_r}. \tag{4}$$

The resonant amplitude represents the product of the $\langle\lambda_R|\, T_{em}\, |\lambda_\gamma\lambda_p\rangle$ and $\langle\lambda_f|\, T_{dec}\, |\lambda_R\rangle$ photoexcitation and hadronic decay amplitudes, respectively, and the Breit-Wigner propagator for the s-channel hybrid resonance of mass M_r and total decay width Γ_r. The hybrid electroexcitation amplitude is fully determined by the four-momenta of the initial photon and proton in the CM frame and their helicities. With the quantization axis Oz directed along the four-momentum of the initial photon, the hybrid spin projection to the Oz axis λ_R, is determined by angular momentum conservation, $\lambda_R = \lambda_\gamma - \lambda_p$.

The photoexcitation $\langle\lambda_R|\, T_{em}\, |\lambda_\gamma\lambda_p\rangle$ and hadronic decay $\langle\lambda_f|\, T_{dec}\, |\lambda_R\rangle$ amplitudes are related to the two resonance photocouplings $A_{1/2}$ and $A_{3/2}$, and the partial hadronic decay widths to the KY final state Γ_{λ_f} of helicity λ_f, where $\lambda_f = -\lambda_Y$.

In order to relate the hybrid hadronic decay amplitude $\langle\lambda_f|\, T_{dec}\, |\lambda_R\rangle$ to the partial hadronic decay widths to the KY final state Γ_{λ_f} of helicity λ_f, we can rotate the quantization axis adopted for the initial-state $|\lambda_R\rangle$ wave function and re-evaluate the matrix element $\langle\lambda_f|\, T_{dec}\, |\lambda_R\rangle$ in the frame with the quantization axis Oz' for the final KY state. The matrix element $\langle\lambda_f|\, T_{dec}\, |\lambda_R\rangle$ after rotation becomes:

$$\langle\lambda_f|\, T_{dec}\, |\lambda_R\rangle = \sum_{\nu'} \langle\lambda_f|T_{dec}|J_r\ \nu'\rangle d^{J_r}_{\lambda_R\nu'}(\cos\theta_K) e^{i\mu\phi_K}. \tag{5}$$

The superposition of the states $|J_r\ \nu'\rangle$ in Eq.(5) with spin J_r and its projection onto the final-state quantization axis ν', is the transformed wave function of the initial-state $|\lambda_R\rangle$ after the aforementioned rotation of the initial-state quantization axis Oz. Lorentz invariance of the resonance hadronic decay amplitudes requires that the operator T_{dec} should be an SU(2)

$\otimes$ O(3) - spin $\otimes$ orbital momentum scalar. Only the term with $\nu' = \lambda_f$ in Eq.(5) remains non-zero in the sum of Eq.(5), as a consequence of the Wigner-Eckart theorem applied to the matrix elements $\langle \lambda_f | T_{dec} | J_r \ \nu' \rangle$ with the scalar T_{dec} operator. The $\langle \lambda_f | T^{J_r}_{dec} | \lambda_f \rangle$ matrix elements in Eq.(5) are determined by the final-state helicity λ_f only, and are independent of the resonance helicities λ_R. Assuming real values for the matrix element $\langle \lambda_f | T_{dec} | \lambda_f \rangle$, we can relate it to the Γ_{λ_f} partial hadronic decay width of the hybrid state to the final KY state of helicity λ_f Γ_{λ_f}. We employ general relations of quantum theory between the resonance decay amplitude $\langle \lambda_f | T_{dec} | \lambda_R \rangle$ of Eq.(5), the two-body state phase space of the resonance decay products $d\Phi_{2b}$ in the conventions of the JM model [13], and the Γ_{λ_f} decay width:

$$\Gamma_{\lambda_f} = \frac{1}{2M_r} \frac{1}{2J_r + 1} \sum_{\lambda_R} \int |\langle \lambda_f | T_{dec} | \lambda_R \rangle|^2 d\Phi_{2b}, \tag{6}$$

with the final-state two-body phase space $d\Phi_{2b}$:

$$d\Phi_{2b} = \frac{1}{4\pi^2} \frac{p_f}{4M_r} \sin\theta d\theta d\phi. \tag{7}$$

Inserting Eqs.(5) and (7) into Eq.(6), and accounting for the d-function normalization,

$$\int d^J_{\mu\,\nu}(\cos\theta) \cdot d^J_{\mu\,\nu}(\cos\theta) \sin\theta d\theta = \frac{2}{2J+1}, \tag{8}$$

we obtain for the $\langle \lambda_f | T_{dec} | \lambda_f \rangle$ amplitudes:

$$\langle \lambda_f | T_{dec} | \lambda_f \rangle = \frac{2\sqrt{2\pi}\sqrt{2J_r+1} M_r \sqrt{\Gamma_{\lambda_f}}}{\sqrt{p^r_f}}. \tag{9}$$

The amplitudes $\langle \lambda_f | T_{dec} | \lambda_f \rangle$ are evaluated at the resonant point $W = M_r$. However, in calculations of the resonant cross sections for $W \neq M_r$, the two-body phase space becomes different than that at the resonant point. The factor $\sqrt{\frac{p^r_f}{p_f}}$, where p^r_f and p_f represent the magnitudes of the three momentum of the K^+ in the CM frame at the resonant point and the current W, respectively, is needed to account for this difference and to evaluate the resonant cross sections and amplitudes for W values away from the resonant point, resulting in the following equation for the hybrid hadronic decay amplitude $\langle \lambda_f | T_{dec} | \lambda_f \rangle$:

$$\langle \lambda_f | T_{dec} | \lambda_f \rangle = \frac{2\sqrt{2\pi}\sqrt{2J_r+1} M_r \sqrt{\Gamma_{\lambda_f}}}{\sqrt{p^r_f}} \sqrt{\frac{p^r_f}{p_f}}. \tag{10}$$

The helicity matrix elements of T_{em} are given in terms of two independent photocouplings, $A_{1/2}$ and $A_{3/2}$, which are related to the matrix elements with net helicity $\lambda_R = \lambda_\gamma - \lambda_p = 1/2,\ 3/2$, respectively. The other two helicity states are related by parity. These photocouplings are unambiguously defined through their relation to the N^* electromagnetic decay width Γ_γ:

$$\Gamma_\gamma = \frac{E^2_{\gamma,r}}{\pi} \frac{2M_N}{(2J_r+1)M_r} \left[\left| A_{1/2} \right|^2 + \left| A_{3/2} \right|^2 \right], \tag{11}$$

where $q_{\gamma,r}$ is the three-momentum modulus of the photon at $W = M_r$ in the CM frame.

The transition amplitudes $\langle \lambda_R \, | T_{em} | \, \lambda_\gamma \lambda_p \rangle$ are related to the $A_{1/2}$ and $A_{3/2}$ photocouplings by imposing the requirement that the BW parametrization [78] of the resonant cross section for a single contributing resonance should be reproduced:

$$\sigma(W) = \frac{\pi}{E_\gamma^2}(2J_r + 1)\frac{M_r^2 \Gamma_i(W)\Gamma_\gamma}{(M_r^2 - W^2)^2 - M_r^2\Gamma_r^2}. \tag{12}$$

In this way we obtain the following relationship between the $\langle \lambda_R \, | T_{em} | \, \lambda_\gamma \lambda_p \rangle$ transition amplitudes and the $\gamma_v N N^*$ electrocouplings:

$$\langle \lambda_R \, | T_{em} | \, \lambda_\gamma \lambda_p \rangle = \frac{W}{M_r}\sqrt{\frac{8 M_N M_r q_{\gamma_r}}{4\pi\alpha}}\sqrt{\frac{q_{\gamma_r}}{q_\gamma}} A_{1/2,3/2}. \tag{13}$$

The factor $4\pi\alpha$ in Eq.(13) reflects the particular relationship between the JM model amplitudes and cross sections, when the absolute value of the electron charge is factorized out of the production amplitudes.

The differential cross sections were computed from the amplitudes of Eq.(2) for the KY electroproduction employing the relations from Refs. [12, 58] and for the $\pi^+\pi^- p$ electroproduction employing the relations from Ref. [11]. In order to examine the feasibility of observing a hybrid baryon signal, we have computed the differential cross sections for the aforementioned exclusive channels in Model A (without hybrid) and Model B (with hybrid). The computations within Model B were carried out with variable values of the hybrid baryon electrocouplings. For the statistical uncertainties expected in the experimental data, we compared the cross sections in Model A and Model B and determined the minimal values of the hybrid baryon electrocouplings above which the difference between the cross sections become statistically significant.

In our approach we compared the differential cross sections with and without the hybrid point-by-point in several bins over Q^2 and within the interval 2.1 GeV $< W <$ 2.3 GeV. In this way, we established the minimal values of the hybrid electroexcitation amplitudes at different Q^2 above which the signal from the hybrid will be statistically significant and therefore can be observed in the data. For comparison of the differential cross sections computed in Models A and B, we are using $\chi^2/d.p.$ as a measure for the evaluation of the statistical significance of the cross section difference. In the extraction of the resonance electrocouplings from $N\pi$ and $\pi^+\pi^- p$ electroproduction data measured with CLAS, the data description within the reaction model was treated as acceptable for $\chi^2/d.p. < 3$. Therefore, we consider the hybrid signal as statistically significant if the comparison of the differential cross sections computed within Models A and B results in $\chi^2/d.p. > 4$. In this way we take into account any systematic uncertainties related to the use of the reaction model of limited accuracy in reproducing the experimental data.

7.5 Threshold Values for Hybrid Baryon Couplings in $\pi^+\pi^- p$

In order to examine the feasibility to observe a signal from a hybrid baryon in exclusive $\pi^+\pi^- p$ electroproduction, we have computed the following four one-fold differential cross sections:

- invariant mass distributions $d\sigma/dM_{\pi^+\pi^-}$ and $d\sigma/dM_{\pi^+ p}$ for two pairs ($\pi^+\pi^-$ and $p\pi^+$) of the final state particles;

- angular distributions $d\sigma/d(-\cos\theta_{\pi^-})$ for the final state π^- in the CM frame;
- angular distributions $d\sigma/d\alpha_{[p'\pi^+][p\pi^-]}$ over the rotational angle α of the plane composed by the three-momenta of the final state p' and π^+ around the direction of the π^- momentum in the CM frame with respect to the plane composed by the three momenta of the initial p and the final π^-.

Each of these cross sections was computed at Q^2=0 GeV^2, 0.65 GeV^2, and 1.30 GeV^2 by integrating the five-fold differential $\pi^+\pi^-p$ cross sections as described in Ref. [28]. The five-fold differential $\pi^+\pi^-p$ cross sections were obtained from the amplitudes of the JM model with (Model A) and without the hybrid state (Model B), employing the relations between the amplitudes and the five-fold differential cross sections from the Appendices of Ref. [11]. The implementation of the hybrid baryon into the full amplitude of the JM model was outlined in Section 7.4. The computations of the one-fold differential cross sections within Model A were carried out for a hybrid baryon of spin-parity $J^P = \frac{1}{2}^+$, with the hadronic parameters described in Section 7.4 and for variable values of the $A_{1/2}(Q^2)$ hybrid electrocouplings in the range from 0 GeV$^{-1/2}$ to 0.150 GeV$^{-1/2}$ with $S_{1/2}(Q^2) = 0$.

The hybrid baryon signal should be seen in the difference of the one-fold differential cross sections computed with and without the hybrid. The statistical significance of the signal is quantified in terms of $\chi^2/d.p.$ estimated as:

$$\chi^2/d.p. = \frac{1}{N_{d.p.}} \sum_{W_i} \sum_{\substack{X=m_{\pi^+\pi^-}, m_{\pi^+p}, \\ \theta_{\pi^-}, \alpha_{\pi^-}}} \frac{\left(\frac{d\sigma_{nohyb}}{dX} - \frac{d\sigma_{hyb}}{dX}\right)^2}{\left(\varepsilon_{hyb}\frac{d\sigma_{hyb}}{dX}\right)^2}. \quad (14)$$

The $\frac{d\sigma_{hyb/nohyb}}{dX}$ values represent the one-fold differential cross sections with and without the hybrid contribution, while dX represent the differentials for the four one-fold differential cross sections listed above. We have assigned statistical uncertainties ε_{hyb} expected with the run conditions described in Section 5 to the differential cross sections of Model A, while the differential cross sections computed in Model B were treated as the fit curves known exactly from the model. Only the expected statistical uncertainties are included into the evaluation of the statistical significance of the one-fold differential cross section differences in Eq.(14). The internal sum runs over all of the quasi-data points of the four one-fold differential cross sections, computed in each bin of W and Q^2 on the grid consisting of 16 (12) bins over the final state hadron invariant masses and 14 (6) bins over the CM angles θ_{π^-} and α_{π^-} for the photoproduction (electroproduction) reaction. The external sum in Eq.(14) runs over all 25-MeV-wide W bins from 2.1 GeV to 2.3 GeV. The total number of the quasi-data points $N_{d.p.}$ involved in the studies at each Q^2 point is equal to 420 for photoproduction and 252 for electroproduction.

The statistical uncertainties of the one-fold differential cross sections with the hybrid state were chosen to be the following: 3% at Q^2 = 1.3 GeV^2, 2% at Q^2 = 0.65 GeV^2, and 1% at Q^2 = 0 GeV^2. The statistical uncertainties at Q^2=1.3 GeV^2 were estimated based on the comparison with the statistical uncertainties of the data from our previous CLAS experiment collected at the bin centered at Q^2=1.3 GeV^2 [47]. The statistical uncertainties of the expected data were estimated accounting for the differences between the integrated luminosity and the virtual photon fluxes of both experiments, the ratio of the efficiencies for

the topology with all three final state hadrons detected (conservative evaluation), and for the differences in the data binning over the kinematic grids. The statistical uncertainties for the data in the other two Q^2 bins were obtained by multiplying the uncertainties at Q^2=1.3 GeV^2 by the root square from the ratio of the fully integrated cross sections at the given Q^2 value to that at Q^2=1.3 GeV^2.

The $\chi^2/d.p.$ values were evaluated independently for the different values of the $A_{1/2}$ electrocouplings in each of the three Q^2 bins. As explained in Section 7.4, we assumed that the hybrid signal will be statistically significant if $\chi^2/d.p > 4$, taking into account the final accuracy of the reaction models in reproducing the experimental data. The minimal absolute values of the hybrid $A_{1/2}(Q^2)$ electrocouplings obtained in this way, above which the signal from the hybrid becomes statistically significant in the data on the four one-fold $\pi^+\pi^- p$ differential cross sections, are listed in Table 5. The electrocoupling values that make the hybrid signal statistically significant are comparable with those for most conventional nucleon resonances. Therefore, the proposed experiment offers a promising prospect for the observation of any new hybrid baryon states in the exclusive $\pi^+\pi^- p$ electroproduction reaction.

Q^2 (GeV^2)	0.	0.65	1.3
$A_{1/2} \times 10^{-3}$ (GeV$^{-1/2}$)	45	37	19

Table 5: Threshold values for the $A_{1/2}$ electrocouplings for a statistically distinguishable hybrid state signal.

Representative examples for the ratio F_x of the difference between the one-fold differential cross sections estimated in Models A and B over the differential cross section from Model A are shown in Figs. 32 and 33 at W=2.19 GeV and Q^2=0 GeV^2 and 0.65 GeV^2. These ratio were obtained with the $A_{1/2}(Q^2)$ hybrid electrocoupling values listed in Table 5. Statistically significant signals from the hybrid baryon are evident in the kinematic dependencies of all four one-fold differential cross sections. The most pronounced signals from the hybrid are expected in the ρ peak in the $d\sigma/dM_{\pi^+\pi^-}$ mass distributions and in the two CM angular distributions. In Fig. 34 we show the Q^2 evolution of the ratio F_x for the CM angular distributions $d\sigma/d(-\cos\theta_{\pi^-})$ (left) and $d\sigma/d\alpha_{[p'\pi^+][p\pi^-]}$ (right). The ratio F_x for both angular distributions increases with Q^2, offering a promising opportunity to explore the Q^2 dependencies of the hybrid resonance in a relatively wide Q^2 range. This feature is of particular importance in order to establish the hybrid nature of any new baryon state based on peculiarities seen in the Q^2 behavior of its electrocouplings.

Finally, we note that all estimates presented above for the feasibility of observing a hybrid signal were conservative. The conditions for hybrid baryon observation in exclusive $\pi^+\pi^- p$ electroproduction can be further improved by:

- collecting the $\pi^+\pi^- p$ events in a topology with only two final state hadrons detected in CLAS12, while the four-momenta of the third hadron is reconstructed from energy-momentum conservation. This topology is preferential for optimizing the counting rates but leads to worse resolution for the final hadron invariant mass W;

- employing a trigger with two positive final state hadrons in coincidence with the scattered electron, allowing us to increase the percentage of $\pi^+\pi^- p$ events in the data

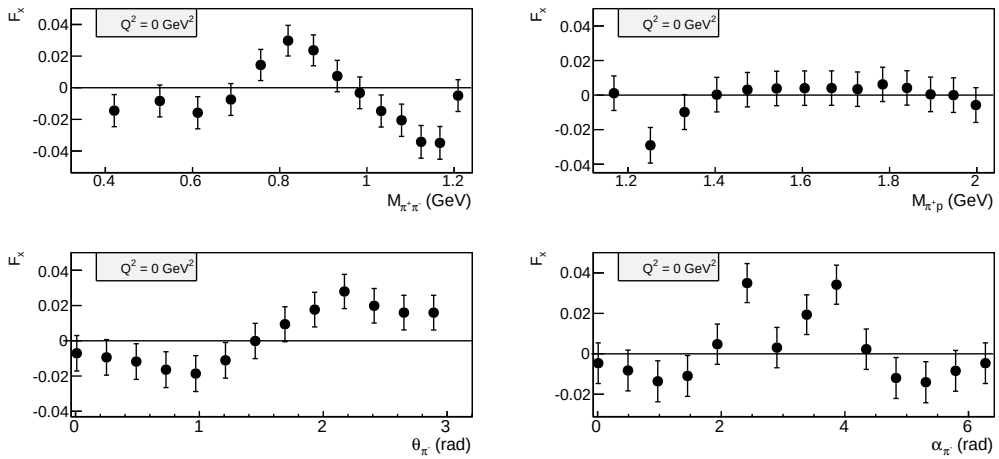

Figure 32: The ratio F_x for the relative differences between the four one-fold differential $\pi^+\pi^- p$ cross sections at Q^2=0 GeV^2 computed with and without a hybrid baryon contribution.

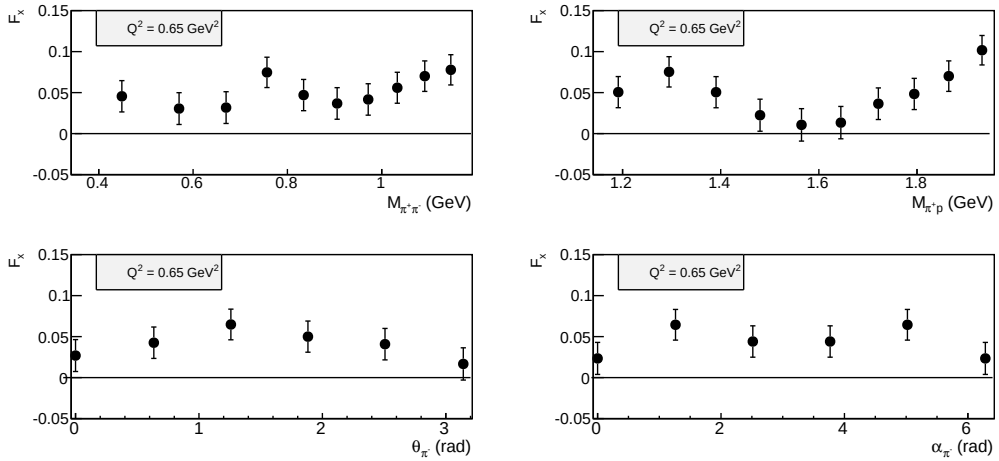

Figure 33: The ratio F_x for the relative differences between the four one-fold differential $\pi^+\pi^- p$ cross sections at Q^2=0.65 GeV^2 computed with and without a hybrid baryon contribution.

sample. However, such a restrictive trigger may give rise to problems for the simultaneous running of several experiments;

- incorporating into the physics analysis the LT, TT, and LT' interference structure functions for the exclusive $\pi^+\pi^- p$ electroproduction.

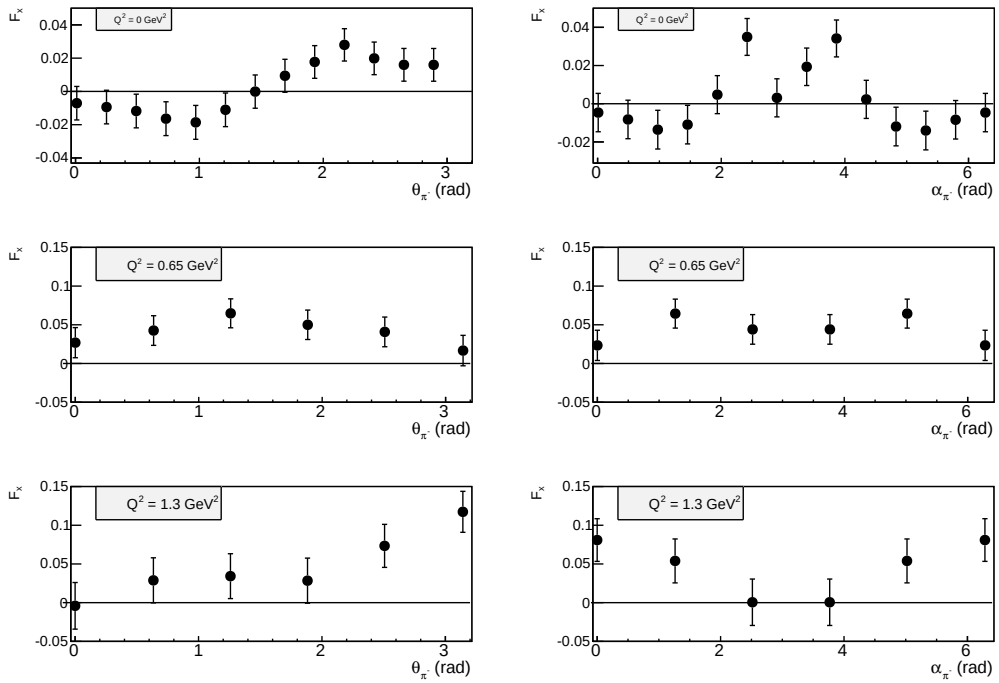

Figure 34: The Q^2 evolution of the ratio F_x for the relative differences between the $d\sigma/d(-\cos\theta_{\pi^-})$ and $d\sigma/d\alpha_{[p'\pi^+][p\pi^-]}$ one-fold differential cross sections computed with and without a hybrid baryon contribution.

7.6 Threshold Values for Hybrid Baryon Couplings in KY

In order to examine the feasibility to observe the signal from a hybrid baryon in exclusive KY electroproduction, we computed the two-fold virtual photon differential cross sections $\frac{d^2\sigma}{d\Omega_K}$, where $d\Omega_K$ is the differential of the solid angle for K^+ emission in the CM frame $d\Omega_K{=}d(-\cos\theta_K)d\phi_K$. These cross sections are computed using the model without the hybrid state included (Model A) and with the hybrid state included (Model B). In both models for evaluation of the amplitudes the RPR model from Ghent was used [12, 58]. For the hybrid resonance parameters, we used a mass of 2.2 GeV, total decay width 0.25 GeV, and a 3% branching fraction for decays to the $K^+\Lambda$ final state. The contributions from hybrids of spin-parities $J^P = \frac{1}{2}^+$ and $J^P = \frac{3}{2}^+$ were simulated. The hybrid amplitude was computed in the convention of the JM model and converted to the Ghent model conventions. The full Model A amplitudes were computed for the RPR model conventions employing Eq.(2). The $K^+\Lambda$ cross sections were computed from the Model A and B amplitudes employing the relations between the amplitudes and cross sections from Refs. [12, 58]. Note that $\frac{d^2\sigma}{d\Omega_K}$

differential cross sections were determined by the contributions from both the unpolarized structure function and the interference LT and TT structure functions. In our studies of the hybrid manifestation, the interference effects between the amplitudes of different photon polarizations were taken into account.

In order to identify the candidate hybrid state, we examined the difference between two-fold differential virtual photon $K^+\Lambda$ cross sections $\frac{d^2\sigma_A}{d\Omega_K}$ and $\frac{d^2\sigma_B}{d\Omega_K}$ computed in Model A (without hybrids) and Model B (with hybrid), respectively. The statistical significance of this difference can be quantified in terms of the following $\chi^2/d.p.$ value:

$$\chi^2 = \frac{1}{N_{d.p.}} \sum_{W,\cos(\theta_K),\phi_K} \frac{\left(\frac{d^2\sigma_A}{d\Omega_K} - \frac{d^2\sigma_B}{d\Omega_K}\right)^2}{\delta^2}. \tag{15}$$

The sum includes 24 bins over both θ_K and ϕ_K in each bin of W and Q^2. The W value in Eq.(15) runs from $M_R - \Gamma_R/2$ to $M_R + \Gamma_R/2$ or from 2.1 GeV to 2.3 GeV with a bin width of 20 MeV. Only statistical contributions were taken into account in the evaluation of the uncertainties δ in Eq.(15):

$$\begin{aligned} \delta^2 &= p^2\left(\frac{d^2\sigma_A}{d\Omega_K}\right) + \frac{d^2\sigma_B}{d\Omega_K}) \\ p &= \frac{\sqrt{N(W,Q^2,\theta_K,\phi_K)}}{N(W,Q^2,\theta_K,\phi_K)}. \end{aligned} \tag{16}$$

Here, the statistical uncertainties δ were estimated as the percentage p from the computed cross sections. The values of p in the four dimensional bin of $(W, Q^2, \theta_K, \phi_K)$ were determined by the number of $K^+\Lambda$ exclusive events $N(W, Q^2, \theta_K, \phi_K)$ collected in the bin. The bin populations were computed starting from the number of total collected $K^+\Lambda$ events estimated for the run conditions described in Section 6.4. The bin populations were determined by using the event generator that employs the RPR model for the description of the event distribution over the reaction phase space. The CLAS12 acceptance was taken into account in the evaluation of the bin populations using FASTMC.

In order to determine the minimal hybrid electrocoupling values providing a statistically significant signal from the new state, we computed the $\chi^2/d.p.$ varying the values of hybrid-candidate electrocouplings for the both spin-parity assignments $J^P = \frac{1}{2}^+$ and $J^P = \frac{3}{2}^+$ in the following way. Each of three couplings $A_{1/2}(Q^2)$, $A_{3/2}(Q^2)$, and $S_{1/2}(Q^2)$ were varied in the range from 0.01 GeV$^{-1/2}$ to 0.03 GeV$^{-1/2}$, while the two others are set equal to zero. With the variable hybrid electrocouplings, the $\chi^2/d.p.$ values were computed independently in 10 Q^2 bins of 0.1 GeV^2 width in a range of photon virtualities from 0.05 GeV^2 to 1.05 GeV^2.

We consider the signal from a candidate hybrid baryon state as statistically significant if $\chi^2/d.p. > 4$. The minimal values of $A_{1/2}$, $A_{3/2}$, and $S_{1/2}$ found in this way are presented in Tables 6 and 7 for E_b=6.6 GeV and 8.8 GeV. It was found that the minimal electrocoupling values have no pronounced dependence on the beam energy.

The minimal electrocoupling values listed in Tables 6 and 7 for the observation of a hybrid baryon turn out to be smaller than the photo-/electrocouplings of most regular nucleon resonances extracted from the photo-[32] and electroproduction data at Q^2 up to 1.0 GeV^2 [4] measured with CLAS. Note that the studies of exclusive photoproduction with CLAS

have already revealed signals of eight new N^* states. Therefore, our estimates of the minimal electrocoupling values needed for hybrid baryon observation suggest very encouraging prospects for a hybrid baryon search in exclusive KY electroproduction.

Q^2, GeV^2	J_R=1/2		J_R=3/2		
	$A_{1/2}$	$S_{1/2}$	$A_{1/2}$	$A_{3/2}$	$S_{1/2}$
0.1	12	12	16	11	10
0.5	17	19	18	19	12
1.0	16	21	16	18	10

Table 6: The minimal values of the electrocouplings for E_b=6.6 GeV and torus current $I = -3375$ A for the resonances with J= 1/2 and 3/2. $A_{1/2}$, $A_{3/2}$, and $S_{1/2}$ are in units of $10^{-3}\times$ GeV$^{-1/2}$. When determining the minimal value of $A_{1/2}$ we varied only $A_{1/2}$, while setting the other electrocouplings to zero. The minimal values of $A_{3/2}$ and $S_{1/2}$ were obtained in the same way.

Q^2, GeV^2	J_R=1/2		J_R=3/2		
	$A_{1/2}$	$S_{1/2}$	$A_{1/2}$	$A_{3/2}$	$S_{1/2}$
0.3	12	12	14	12	9
0.5	19	20	19	21	12
1.0	16	21	16	18	9

Table 7: The minimal values of the electrocouplings for E_b=8.8 GeV and torus current $I = -3375$ A for the resonances with J= 1/2 and 3/2. $A_{1/2}$, $A_{3/2}$, and $S_{1/2}$ are in units of $10^{-3}\times$ GeV$^{-1/2}$. When determining the minimal value of $A_{1/2}$ we varied only $A_{1/2}$, while setting the other electrocouplings to zero. The minimal values of $A_{3/2}$ and $S_{1/2}$ were obtained in the same way.

Figs. 35 and 36 show representative examples of two-fold differential cross sections computed with and without a hybrid baryon contribution. The differential cross sections with hybrid baryons are evaluated for the minimal values of the electrocouplings that make the hybrid signal statistically significant. The hybrid state produces sizable differences in the two-fold differential cross sections at the resonant point W=2.2 GeV at the backward kaon emission angles with respect to the incoming virtual photons in the CM frame. The differences between the differential cross sections computed with/without the hybrid contribution are much larger than the cross sections from the hybrid contribution. This feature suggests pronounced interference effects between the hybrid contribution and the remaining amplitudes. Studies of the unpolarized cross sections and the interference LT and TT structure functions are of particular importance in order to reveal a presence of the hybrid state.

7.7 Hybrid Baryon Search from Legendre Moment Expansion

An analysis using Legendre moments of the separated structure functions $\sigma_U = \sigma_T + \epsilon\sigma_L$, σ_{LT}, and σ_{TT} has shown promise as a technique to search for evidence of a possible hybrid baryon state. The Legendre moments are defined as:

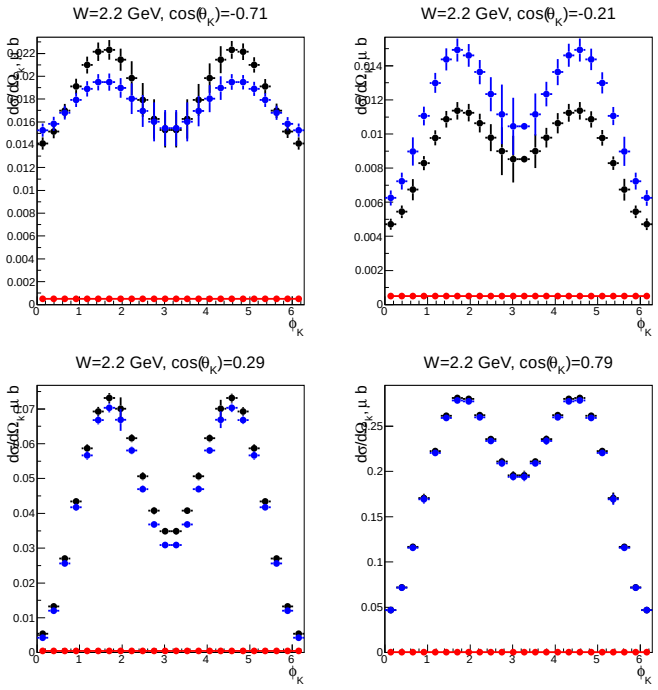

Figure 35: Comparison of the RPR model cross section $d\sigma/d\cos(\theta_K)$ (black points) with the RPR model plus hybrid cross section (blue points) for E_b=8.8 GeV at Q^2=0.3 GeV^2. The cross section of the resonance contribution is shown in red. The spin of the resonance is 1/2 and the $A_{1/2}$ is 12×10^{-3} GeV$^{-1/2}$, corresponding to the minimal $A_{1/2}$ from Table 7. The error bars are statistical only.

$$C_m = \frac{2m+1}{2}\int_{-1}^{1} L_m d\sigma(x)_i dx, \tag{17}$$

where

$$L_m(x) = \sum_{j=0}^{m} a_{mj}x^j \quad \text{with} \quad a_{mj} = (-1)^{(m-j)/2}\frac{1}{2^m}\frac{(m+j)!}{(\frac{m-j}{2})!(\frac{m+j}{2})!j!} \tag{18}$$

are the Legendre polynomials that are functions of $x = \cos\theta_K^*$ with $m-j$ = even. Here, $d\sigma_i(x)$, with $i = T,\ L,\ LT$, and TT, represent the transverse, longitudinal, and interference structure functions that depend on the variables W, Q^2, and θ_K^*.

The Legendre moments may be used to expand the structure functions in terms of the orthogonal Legendre polynomials:

$$\sigma(x)_i = \sum_m P_m(Q^2, W)L_M(\cos\theta_K^*), \tag{19}$$

where the first seven Legendre polynomial functions have the form:

$$\begin{aligned} L_0 &= 1 \\ L_1 &= \cos\theta \\ L_2 &= \frac{1}{2}(3\cos^2\theta - 1) \end{aligned}$$

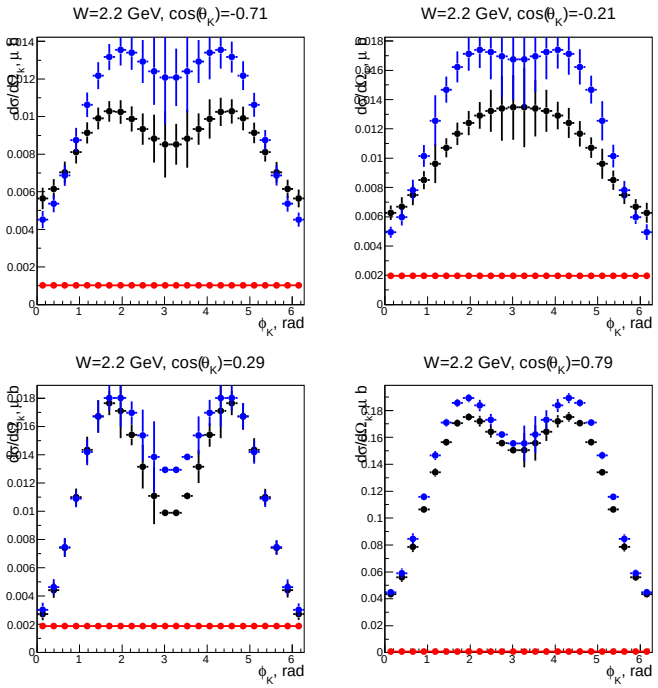

Figure 36: Comparison of the RPR model cross section $d\sigma/d\cos(\theta_K)$ (black points) with the RPR model plus hybrid cross section (blue points) for E_b=8.8 GeV at Q^2=0.3 GeV^2. The cross section of the resonance contribution is shown in red. The spin of the resonance is 3/2 and the $A_{3/2}$ is 18×10^{-3} GeV$^{-1/2}$, corresponding to the minimal $A_{3/2}$ from Table 7. The error bars are statistical only.

$$
\begin{aligned}
L_3 &= \frac{1}{2}(5\cos^3\theta - 3\cos\theta) \\
L_4 &= \frac{1}{8}(35\cos^4\theta - 30\cos^2\theta + 3) \\
L_5 &= \frac{1}{8}(63\cos^5\theta - 70\cos^3\theta + 15\cos\theta) \\
L_6 &= \frac{1}{16}(231\cos^6\theta - 315\cos^4\theta + 105\cos\theta - 5).
\end{aligned} \tag{20}
$$

The expansion of the structure functions in terms of Legendre moments is believed to be an alternative way to probe the sensitivity to a hybrid baryon contribution, since the appearance of a structure in a single Legendre moment at the same value of W for each Q^2 point is likely a signal from a resonance contribution.

As an example, such an approach was carried out for the $K^+\Lambda$ and $K^+\Sigma^0$ electroproduction separated structure functions from CLAS data in Ref. [64]. Fig. 37 shows the first four Legendre moments for σ_U, σ_{LT}, and σ_{TT} for $K^+\Lambda$ at $Q^2 = 1.8$ GeV^2. The fits hint at a possible structure at $W = 1.7$ GeV for C_0 in both the $d\sigma_U$ and $d\sigma_{LT}$, and a possible structure at $W = 1.9$ GeV in both C_2 and C_3 for $d\sigma_U$. Of course, only a full amplitude partial wave analysis will constitute a definite proof for the presence of a resonance, but the study of the Legendre moments of the separate structure functions may provide the first hint of their appearance.

A study of the first seven Legendre moments of the $d\sigma_U$, $d\sigma_{LT}$, and $d\sigma_{TT}$ structure

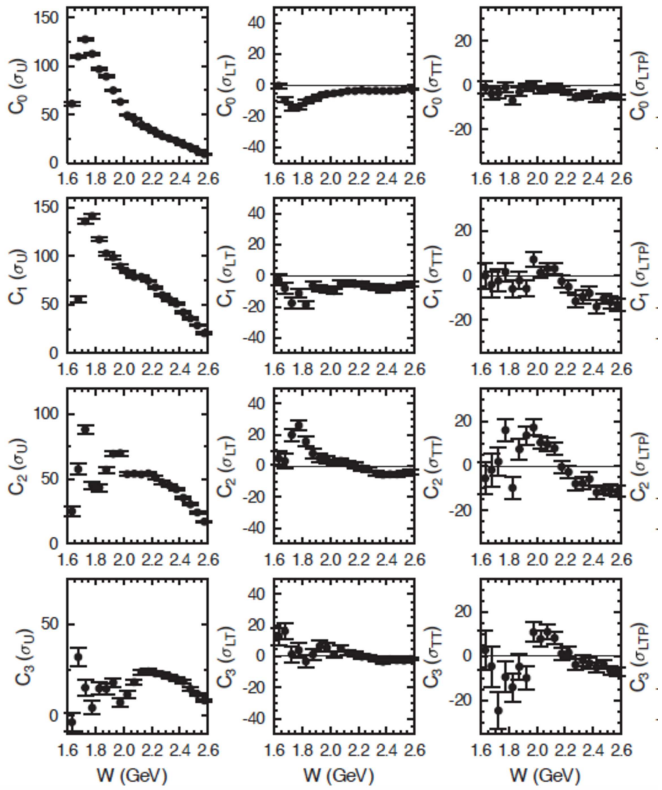

Figure 37: Legendre polynomial fit coefficients for $m = 0 \rightarrow 3$ as a function of W for the $d\sigma_U$ (left), $d\sigma_{LT}$ (middle), and $d\sigma_{TT}$ (right) structure functions for CLAS $K^+\Lambda$ electroproduction data at $Q^2 = 1.8$ GeV^2 [64].

functions has been performed for Models A and B for $K^+\Lambda$ electroproduction, described in the previous section. An example evaluated for both Model A with no hybrid and Model B where a $J^\pi = \frac{1}{2}^+$ hybrid with a fixed electrocoupling of $A_{1/2} = 40$ (10^{-3}) GeV$^{-1/2}$ has been added was considered. Fig. 38 shows the differential cross section for Model B vs. ϕ_K^* for a representative bin at Q^2=1.0 GeV^2, W=2.2 GeV, and $\cos\theta_K^*$=0.90 with the ϕ_K^* moment fits to separate σ_U, σ_{LT}, and σ_{TT}. Figs. 39 and 40 show the separated structure functions $d\sigma_{LT}$ and $d\sigma_{TT}$. It is interesting to note that significant structures appear in most of the Legendre moments at the value of $W = 2.2$ GeV, corresponding to the mass of the added hybrid baryon. The statistical uncertainties, however, become larger than the difference among the two models for the moments of the highest order.

To study the sensitivity of the expected data quality on the resonance contributions in the Legendre moments expansion, the statistical significance of the difference between the Legendre moment evaluation, with and without the inclusion of the hybrid baryon contribution, has been evaluated using the χ^2 definition:

$$\chi^2 = \frac{1}{N.P.} \sum_W \frac{[C_m(Q^2)_A - C_m(Q^2)_B]^2}{\delta^2 C_m(Q^2)}, \tag{21}$$

where the sum runs over W. $C_m(Q^2)_B$ and $C_m(Q^2)_A$ are the values of the Legendre moments with and without the hybrid baryon contribution, respectively, and $\delta C_m(Q^2)$ is the statistical uncertainty of the Legendre moments.

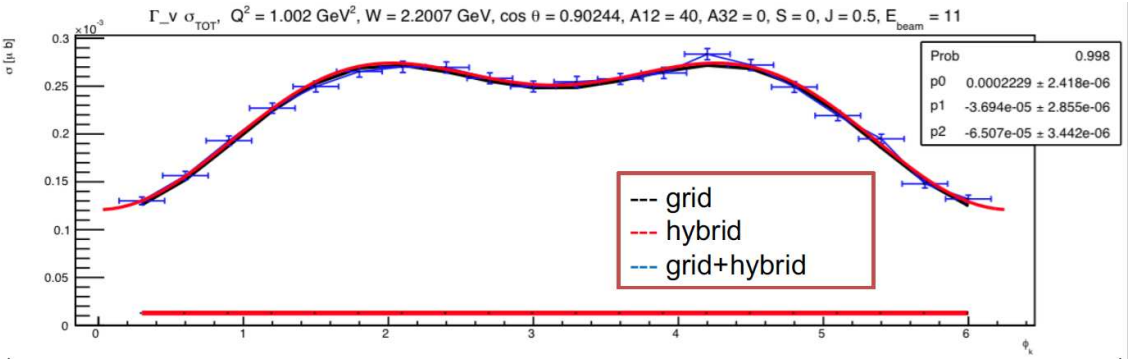

Figure 38: $d\sigma_U$, $d\sigma_{LT}$, and $d\sigma_{TT}$ structure functions for $K^+\Lambda$ electroproduction extracted from the simulated dependence of the differential cross section vs. ϕ_K^* for a representative bin in Q^2, W, and θ_K^*. The cross section $\frac{d^2\sigma}{d\Omega_K^*}$ has been evaluated from Model B where a $J^P = \frac{1}{2}^+$ hybrid baryon of 2.2 GeV mass has been added with electrocoupling strengths $A_{1/2} = 40$ (10^{-3}) GeV$^{-1/2}$ and $S_{1/2} = 0$ GeV$^{-1/2}$. The cross section points have been smeared according to the expected statistical uncertainty.

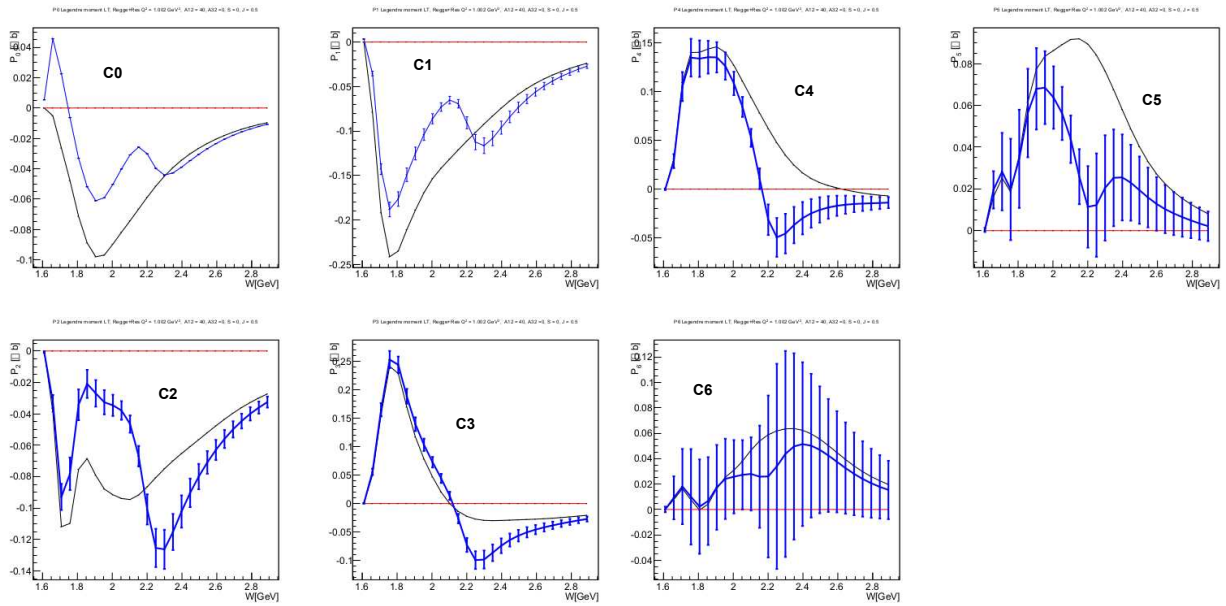

Figure 39: Legendre polynomial fit coefficients for $m = 0 \rightarrow 6$ as a function of W for the $d\sigma_{LT}$ structure functions for $K^+\Lambda$ electroproduction at $Q^2 = 1$ GeV^2, extracted for Model A (black curve) and Model B (blue curve) with an added $J = \frac{1}{2}^+$ hybrid baryon of M=2.2 GeV with electrocoupling strengths $A_{1/2} = 40$ (10^{-3}) GeV$^{-1/2}$ and $S_{1/2} = 0$ GeV$^{-1/2}$.

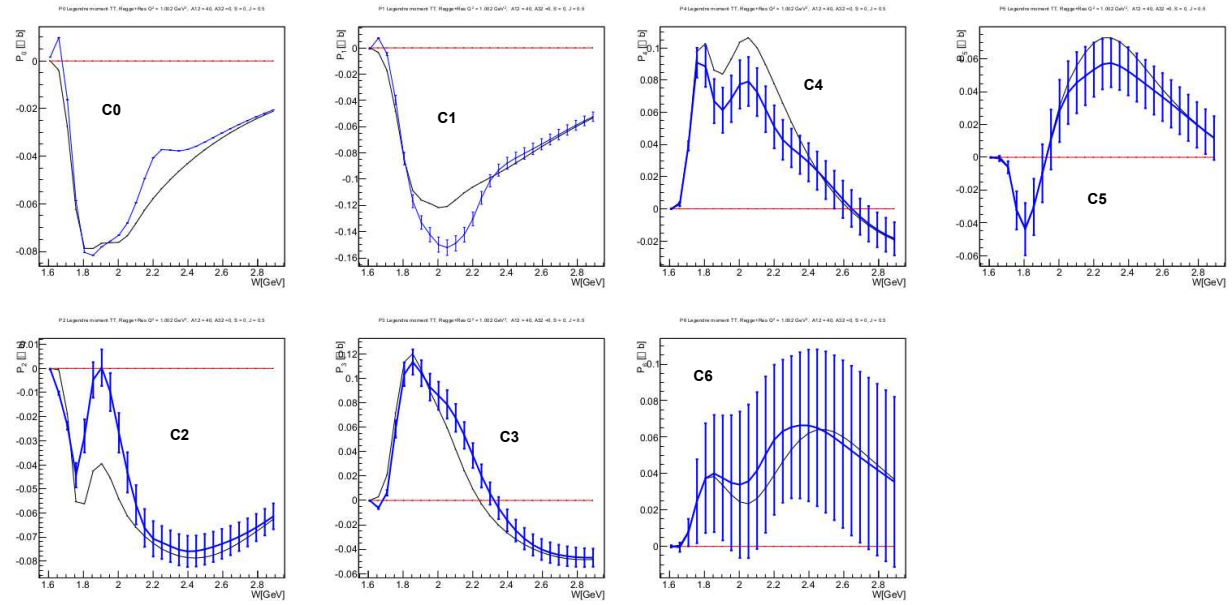

Figure 40: Legendre polynomial fit coefficients for $m = 0 \rightarrow 6$ as a function of W for the $d\sigma_{TT}$ structure functions for $K^+\Lambda$ electroproduction at $Q^2 = 1$ GeV^2, extracted for Model A (black curve) and Model B (blue curve) with an added $J = \frac{1}{2}^+$ hybrid baryon of M=2.2 GeV with electrocoupling strengths $A_{1/2} = 40$ (10^{-3}) GeV$^{-1/2}$ and $S_{1/2} = 0$ GeV$^{-1/2}$.

The χ^2 value has been evaluated for the first seven Legendre moments of the three structure functions $d\sigma_U$, $d\sigma_{LT}$, and $d\sigma_{TT}$ at fixed Q^2 values, fixing the resonance mass at 2.2 GeV, the spin and parity to $J^P = \frac{1}{2}^+$, and varying the $A_{1/2}$ electrocoupling values of the resonance keeping $S_{1/2}$ fixed at 0. The results are shown in Fig. 41 for Q^2=1.0 GeV^2. The threshold values of the $A_{1/2}$ electrocoupling corresponding to a reduced χ^2 value equal to 4, are shown in the legend and are comparable with those found in Table 6 in Section 7.6 for the hybrid baryon coupling threshold from the cross section analysis. The $d\sigma_{LT}$ and $d\sigma_{TT}$ Legendre moments show a higher sensitivity than the unseparated $d\sigma_U$ moments. The minimum detectable values of the electrocoupling strengths are compatible with the values reported by the PDG [1] for the higher masses N^* resonances. Similar conclusions have been obtained in our studies including a $J^P = \frac{3}{2}^+$ hybrid resonance.

7.8 Experimental Sensitivity to Hybrid Resonance States

A search for hybrid baryon states incorporates two major components: a) the identification of the new state that could be considered as a candidate for a hybrid based on its spin-parity and its particular location in the spectrum with respect to the established N^* states (see Section 3) and b) the extraction of its $\gamma_v pN^*$ electrocouplings at different photon virtualities for identification of the hybrid nature of the new state. These objectives will be achieved in the analysis initially by employing advanced reaction models and then eventually within the framework of global, multi-channel partial wave analyses that incorporate advanced coupled-channel approaches as described in Section 3.3.

In this Section we present our studies of the feasibility to identify a new baryon state and to determine its electrocouplings based on the resonance parameter evaluations from the quasi-data simulated within the framework of the Ghent RPR model [12, 58] for the KY

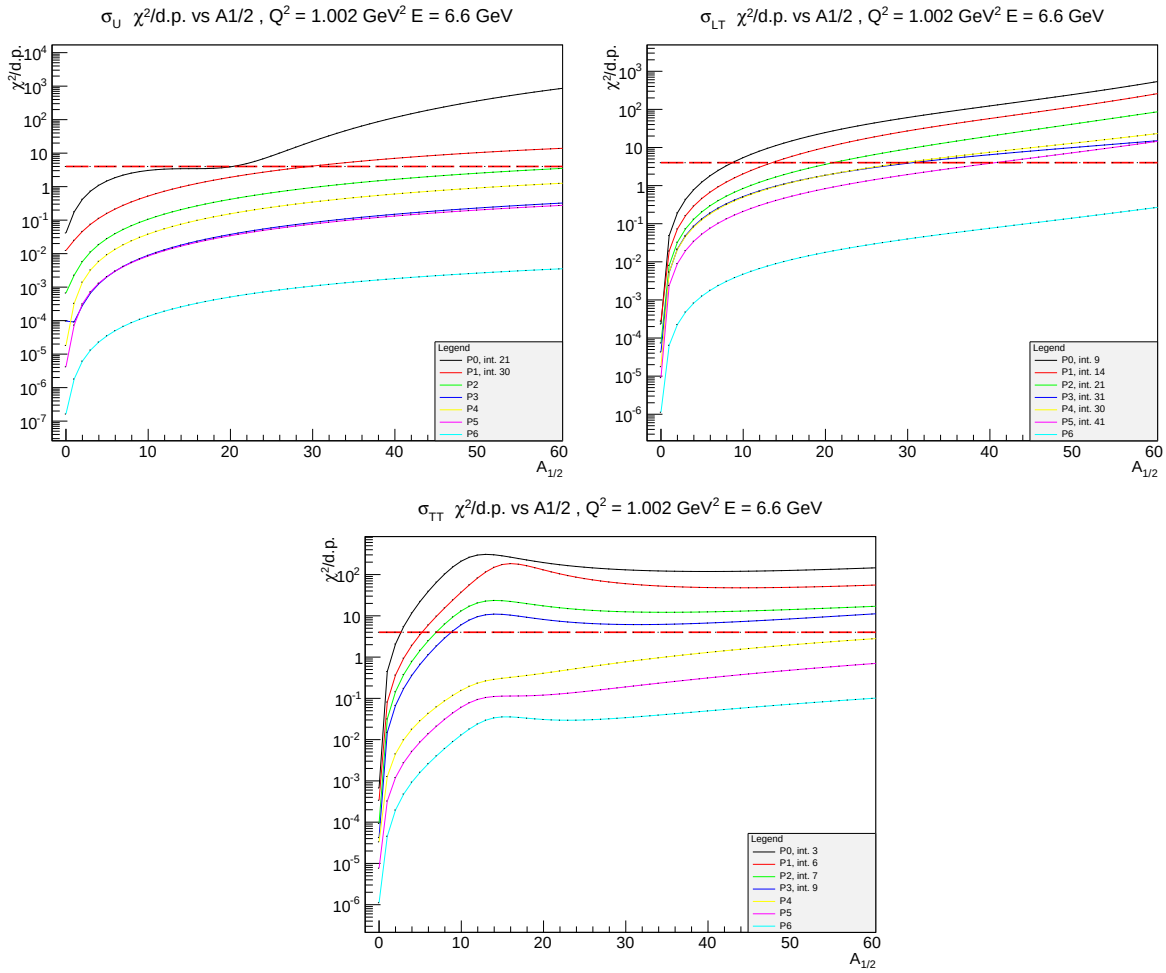

Figure 41: χ^2 values for the Legendre polynomial fit coefficients for $m = 0 \rightarrow 6$ considering the difference between Model A and Model B as a function of $A_{1/2}$ in units of 10^{-3} GeV$^{-1/2}$ keeping $S_{1/2} = 0$ GeV$^{-1/2}$ fixed for the structure functions $d\sigma_U$ (upper left), $d\sigma_{LT}$ (upper right), and $d\sigma_{TT}$ (bottom) for $K^+\Lambda$ electroproduction at Q^2=1 GeV^2. The resonance is assumed to have $J = \frac{1}{2}^+$ and M=2.2 GeV.

channel and the JM model [11, 13] for the $\pi^+\pi^- p$ channel including a hybrid state resonance with known parameters. In order to study the possibility to identify a new baryon state, we employ the approach developed by the Bonn-Gatchina group for the identification of new states [79]. This approach was successfully employed in the analyses of the exclusive CLAS $K^+\Lambda$ photoproduction data [80] that provided the evidence for the new baryon states reported in the recent PDG edition [1]. In this approach the model and the measured observables were confronted in the fit with a running mass for the candidate resonance W_R by computing $\chi^2/d.p$ for each value of W_R. Pronounced minima in $\chi^2/d.p(W)$ observed in the Bonn-Gatchina analyses of the meson photoproduction data allowed them to identify the presence of new baryon states and to determine their masses.

In order to examine our capability to observe a candidate hybrid state in analyses of the KY and $\pi^+\pi^- p$ electroproduction data, we generated quasi-data for the differential cross sections $\frac{d^2\sigma_{exp}}{d\Omega_K}$ for the KY channel, as well as the four one-fold differential cross sections listed

in Section 7.5 for the $\pi^+\pi^-p$ channel. The quasi-data were generated in the kinematic area of our hybrid baryon search, 2.1 GeV $< W <$ 2.3 GeV and 0 GeV^2 $< Q^2 <$ 1.5 GeV^2. The cross sections were computed for different assignments of the hybrid baryon electrocouplings and hadronic decay widths described in Sections 7.5 and 7.6. The quasi-data cross sections were obtained for the hybrid state spin-parities $J^P = \frac{1}{2}^+$ and $J^P = \frac{3}{2}^+$. We then fit these quasi-data by computing the model cross sections taken from the same models as for the quasi-data but replacing the hybrid resonance mass employed in the evaluation of the quasi-data cross sections by running the resonance mass W_R for the fit model cross sections. The $\chi^2/d.p.(W)$ values were obtained as:

$$\chi^2/d.p. = \frac{1}{N_{d.p.}} \sum_{X_i} \frac{\left(\frac{d\sigma_{model}}{dX} - \frac{d\sigma_{exp}}{dX}\right)^2}{\delta^2}. \tag{22}$$

Here, dX represents the appropriate differential for the KY and the $\pi^+\pi^-p$ exclusive cross sections, while the sum runs over all variables in the fit of these cross sections in a single Q^2 bin as described in Sections 7.5 and 7.6, respectively. δ represents the quasi-data cross section uncertainties.

The results obtained for the $K^+\Lambda$ channel are shown in Fig. 42 for the hybrid spin-parity assignments $J^P = \frac{1}{2}^+$ and $J^P = \frac{3}{2}^+$. The corresponding results for the $\pi^+\pi^-p$ channel are shown in Fig. 43. The results are shown for different Q^2 bins in the range of photon virtualities covered in the proposed experiment. In all cases the $\chi^2/d.p.(W_R)$ dependencies show pronounced dips of considerable widths and depth as the W_R mass approaches the true resonance mass. The zero values of $\chi^2/d.p.$ at W_R equal to the generated hybrid mass at 2.2 GeV are related to the fact that we compare model cross sections to the quasi-data evaluated within the *same* model. The observed behavior of $\chi^2/d.p.(W_R)$ strongly suggests the capability to identify the presence of new states from the data of the proposed experiment.

We also explored the data sensitivity to the hybrid spin-parity assignment. We generated quasi-data for the $K^+\Lambda$ channel implementing a hybrid state of spin-parity $J^P = \frac{1}{2}^+$. Instead, the model cross sections for the quasi-data fit were computed with the same parameters of the hybrid as for the quasi-data, but for both spin parities $J^P = \frac{1}{2}^+$ and $J^P = \frac{3}{2}^+$ and with variable resonance mass W_R. The $\chi^2/d.p.(W_R)$ values taken from the quasi-data fit in the models with both spin-parities for the hybrid are shown in Fig. 44. In the situation where the quasi-data for the hybrid resonance of spin-parity $J^P = \frac{1}{2}^+$ are described by the model cross sections computed for another hybrid spin-parity $J^P = \frac{3}{2}^+$ with all other resonance parameters the same, the $\chi^2/d.p.(W_R)$-dependence shows a maximum at W_R equal to the resonance mass. Instead, if we would fit the quasi-data by the model cross sections computed with the "true" spin-parity of the hybrid $J^P = \frac{1}{2}^+$, $\chi^2/d.p.(W_R)$ shows the expected minimum at W_R equal to the resonance mass. Therefore, the data are very sensitive to the spin-parity assignment of the new baryon state, which is an encouraging prospect in establishing the spin-parity of the new baryon state from the data fit.

In order to explore the feasibility of extracting the electrocouplings of a new resonance from the expected data, we examined our capability to disentangle the contributions from the resonance electrocouplings $A_{1/2}(Q^2)$, $A_{3/2}(Q^2)$, and $S_{1/2}(Q^2)$ that describe the resonance electroexcitation for different helicities of the initial photon and proton. For this study we generated quasi-data for the $\pi^+\pi^-p$ channel at Q^2=0.65 GeV^2 for a hybrid state of spin-

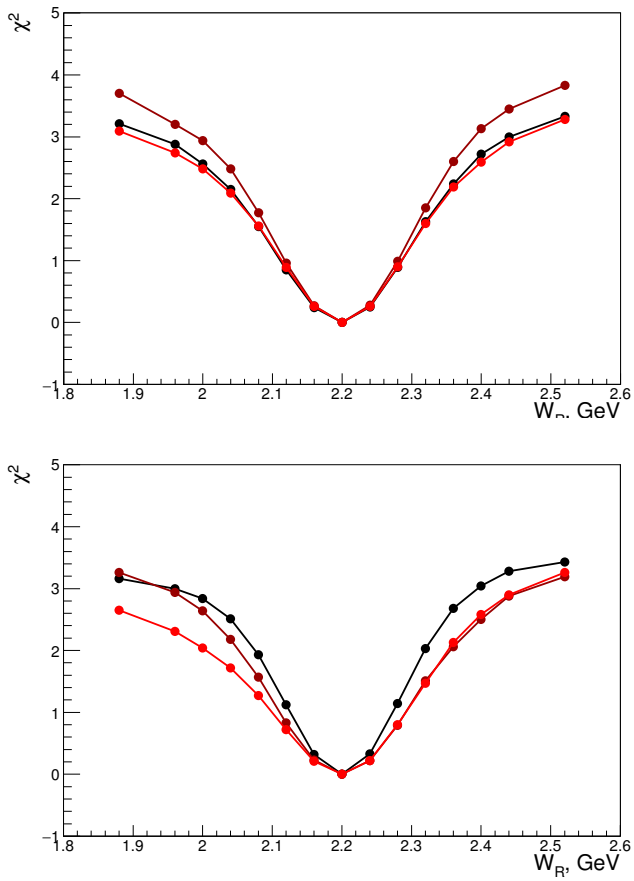

Figure 42: The $\chi^2/d.p.(W_R)$ dependencies evaluated from the comparison between the quasi-data and the model cross sections computed with a running resonance mass W_R for Q^2=0.1 GeV^2 (black), 0.5 GeV^2 (brown), and 1.0 GeV^2 (red) for the $K^+\Lambda$ channel. The results in the top and bottom panels correspond to hybrid state spin-parities $J^P = \frac{1}{2}^+$ and $J^P = \frac{3}{2}^+$, respectively.

parity $J^P = \frac{1}{2}^+$ with $A_{1/2}$ set to the minimal value needed for the observation of the hybrid state in the data (see Table 5), while $S_{1/2}$ was set to zero. The model cross sections used in the quasi-data fit were computed with the same hybrid parameters as were used for the quasi-data generation, but under different assumptions on the hybrid electrocouplings: a) the same electrocouplings as were used in the quasi-data generation and b) $A_{1/2}$ set to zero, while $S_{1/2}$ was set to the value of $A_{1/2}$ used in the quasi-data generation. The results for $\chi^2/d.p.(W_R)$ for both cases are shown in Fig. 45. Employing helicity coupling of the same helicity as for generated quasi-data we have the expected minimum in $\chi^2/d.p.(W_R)$ at the "true" hybrid mass, while the description of the state with a different helicity coupling $S_{1/2}$ produces a W-dependence of $\chi^2/d.p.$ without a pronounced dip. These differences strongly suggest a promising opportunity to disentangle between the $A_{1/2}(Q^2)$ and $S_{1/2}(Q^2)$ electrocouplings.

Similarly, for the studies of the KY channel sensitivity to different helicity electrocouplings, we generated KY quasi-data at Q^2=0.5 GeV^2 for a hybrid of spin-parity $J^P = \frac{3}{2}^+$, assuming $A_{1/2}$ at the minimal values needed for hybrid signal observation (see Table 6), with all others helicity electrocouplings set to zero. We then described the quasi-data by the model cross sections computed under two assumptions for the hybrid state electrocouplings: a) the same hybrid electrocouplings as those used in the quasi-data generation and

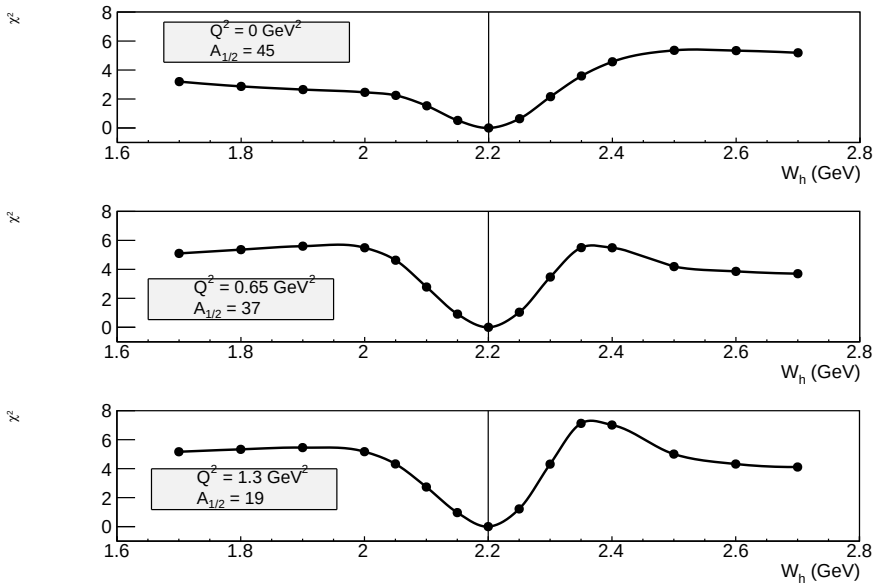

Figure 43: The $\chi^2/d.p.(W_R)$ dependencies for three Q^2 points, 0 GeV^2, 0.65 GeV^2, and 1.3 GeV^2, evaluated from the comparison between the $\pi^+\pi^-p$ quasi-data and model cross sections computed with a running resonance mass W_R for a hybrid spin-parity $J^P = \frac{1}{2}^+$.

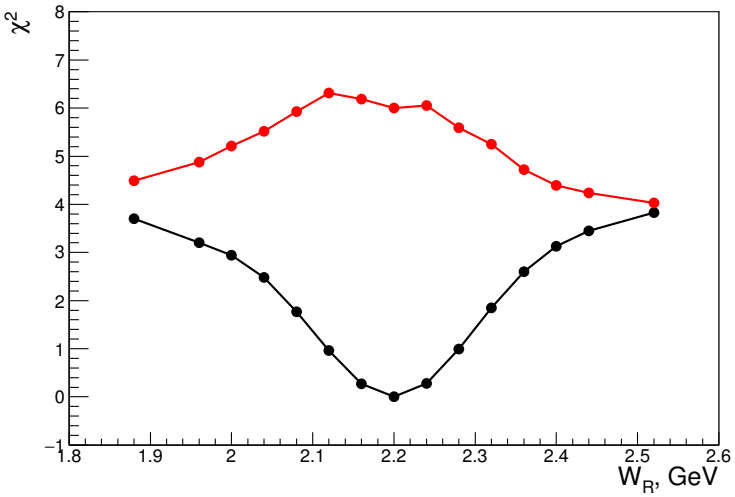

Figure 44: The $\chi^2/d.p.(W_R)$ dependencies evaluated from the comparison between the quasi-data generated for a hybrid state of spin-parity $J^P = \frac{1}{2}^+$ for Q^2=0.5 GeV^2, E_b=6.6 GeV, and model cross sections for the hybrid spin-parity $J^P = \frac{1}{2}^+$ (black) and $J^P = \frac{3}{2}^+$ (red), computed with a running resonance mass W_R.

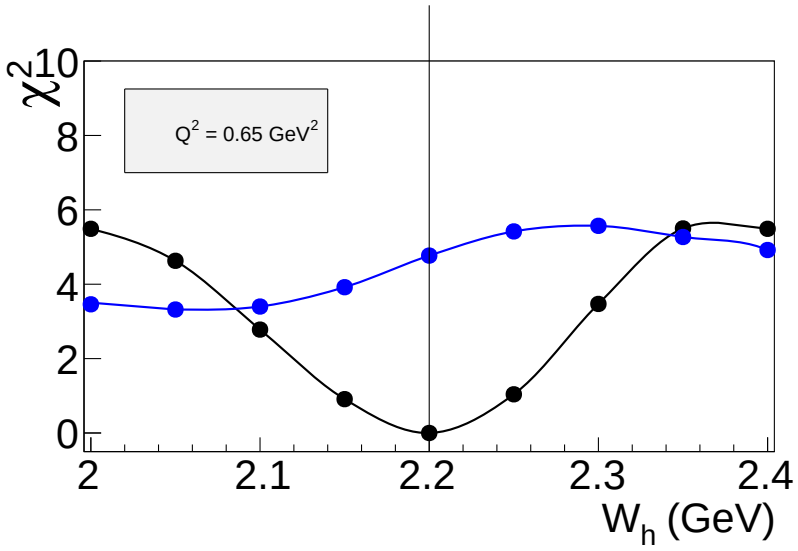

Figure 45: The $\chi^2/d.p.(W_R)$ dependencies evaluated from the comparison between the quasi-data for the $\pi^+\pi^-p$ channel generated for a hybrid state of spin-parity $J^P = \frac{1}{2}^+$ for Q^2=0.65 GeV^2 with $A_{1/2}$ set to the minimal value for the hybrid state observation (see Table 5) and $S_{1/2}$=0. The model cross sections are computed for two assignments for the hybrid helicity electrocouplings: a) the same electrocouplings as used in the quasi-data generation (black) and b) $A_{1/2}$ set to zero and $S_{1/2}$ set to the value of $A_{1/2}$ used in the quasi-data generation (blue).

b) $A_{3/2}$ set to the value of $A_{1/2}$ used for the quasi-data generation with all others helicity electrocouplings set to zero. The results are shown in Fig. 46. Attempts to describe the data employing the hybrid electrocoupling $A_{3/2}$ instead of $A_{1/2}$ result in a maximum in the $\chi^2/d.p.(W_R)$ dependence at the hybrid mass instead of the minimum seen for the correct assignment for the helicity coupling.

Our studies conclusively demonstrated that the data for the KY and $\pi^+\pi^-p$ channels will allow us to disentangle between the contributions from electrocoupling of a new state for different helicities of the initial photon and proton $A_{1/2}(Q^2)$, $S_{1/2}(Q^2)$, and $A_{3/2}(Q^2)$.

In order to obtain initial estimates for the accuracy of the electrocouplings of the new state that could be extracted from the data, we explored the sensitivity of the quasi-data for the $\pi^+\pi^-p$ channel to variations of the hybrid resonance electrocouplings. We generated quasi-data for photon virtualities Q^2= 0 GeV^2, 0.65 GeV^2, and 1.30 GeV^2 for a hybrid state of spin-parity $J^P = \frac{1}{2}^+$ with the hadronic parameters listed in Table 5 of Section 7.5 for the minimal values of $A_{1/2}(Q^2)$ needed for the observation of the state in the data. The model cross sections for the data description were computed with all hybrid parameters set to be the same as were used for the quasi-data generation, with the hybrid mass for the model cross section retained at its "true" value (assuming that the hybrid mass is already determined), but the $A_{1/2}$ electrocouplings varied over a range from 0.5 to 1.5 times the value used for the quasi-data generation. The results for $\chi^2/d.p.(A_{1/2})$ are shown in Fig 47. The $\chi^2/d.p.(A_{1/2})$ dependencies show the minimum at $A_{1/2}$ approaching its "true" value. We see that a departure from the "true" electrocoupling value by 20% causes $\chi^2/d.p.$ to increase by $\approx$0.5. The result of our studies suggests that the hybrid resonance electrocouplings from the

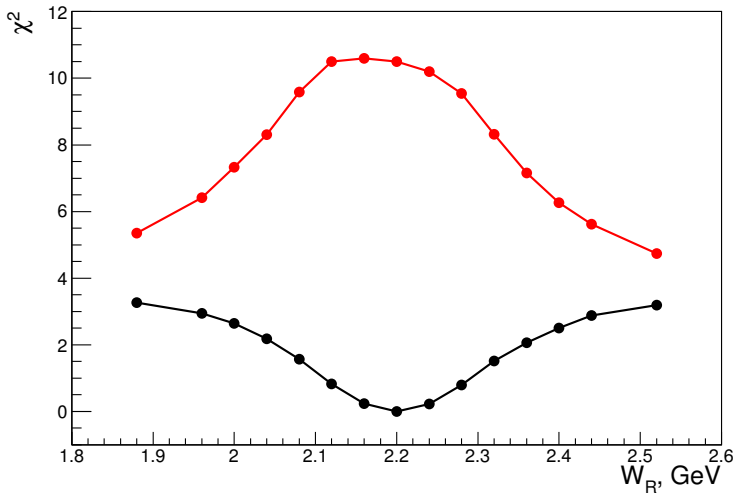

Figure 46: The $\chi^2/d.p.(W_R)$ dependencies evaluated from the comparison between the quasi-data for the $K^+\Lambda$ channel generated for a hybrid state of spin-parity $J^P = \frac{3}{2}^+$ for Q^2=0.5 GeV^2 with $A_{1/2}$ set to the minimal value needed for the hybrid state observation (see Table 6), with all others helicity couplings set to zero. The model cross sections are computed for two assignments for the hybrid helicity electrocouplings: a) the same electrocouplings as used in the quasi-data generation (black) and b) $A_{1/2}$ set to zero and $A_{3/2}$ set to the value of $A_{1/2}$ used in the quasi-data generation (red) with $S1/2$=0.

data for $\pi^+\pi^-p$ electroproduction can be extracted at the level of better than 20% accuracy.

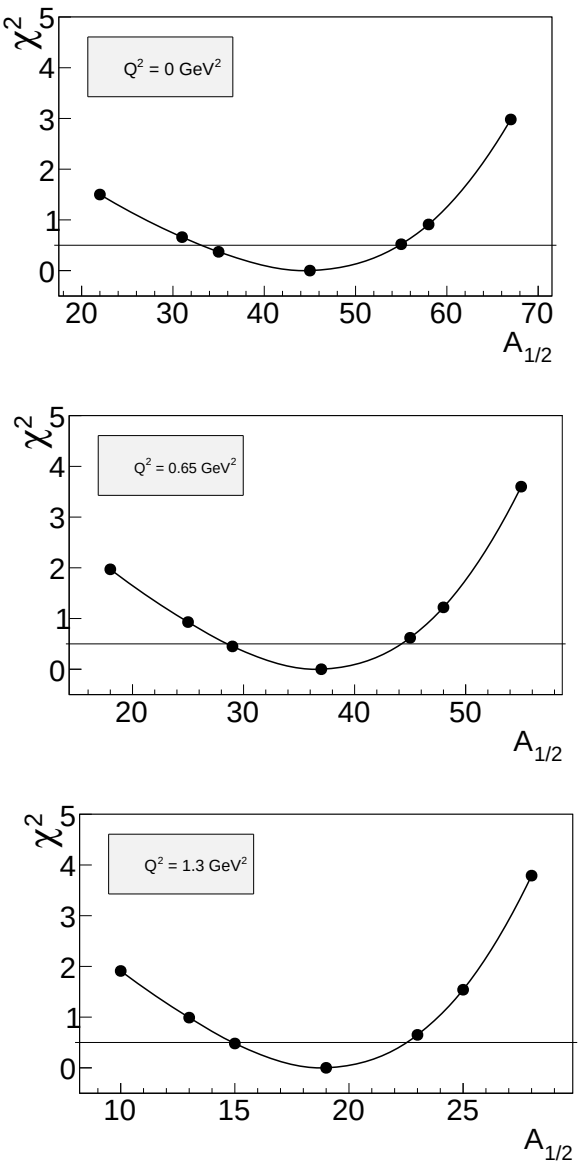

Figure 47: The $\chi^2/d.p.(A_{1/2})$ dependencies evaluated from the comparison between the quasi-data on the $\pi^+\pi^- p$ channel generated for a hybrid state of spin-parity $J^P = \frac{1}{2}^+$ with $A_{1/2}$ equal to the minimal value for the hybrid state observation (see Table 5) and $S_{1/2}$=0. The model cross sections are computed with all hybrid parameters the same as used in the quasi-data generation, but with a running $A_{1/2}$ electrocoupling.

8 Beamtime Estimate

In order to have a reliable estimate of the required beam time we compare the expected statistics of the proposed experiment with the extensive photoproduction data published by the CLAS Collaboration. These precision data have resulted in the discovery of a set of new excited nucleon states in the mass range of 1.85 GeV to 2.2 GeV.

Differential cross section and Λ recoil polarization for the process $\gamma p \to K^+\Lambda$ have been measured extensively by the CLAS Collaboration [81] covering the W range from 1.62 GeV to 2.8 GeV. In the mass range of interest for this proposal, 10-MeV-wide bins in W and 18 bins in polar angle $\cos\theta_K$, covering nearly the full angle range, have been included in the multi-channel analysis by the Bonn-Gatchina group that identified evidence for eight isospin 1/2 nucleon states in the mass range of 1.7 GeV to 2.1 GeV. Fig. 48 shows examples of two W bins at 1.905 GeV and 2.205 GeV to illustrate the statistical precision of the differential cross sections and the Λ recoil polarization data, ranging from 2% at forward angles to 10% at backward angles for the differential cross sections, and with σ_P ranging from 0.02 to 0.1 for the Λ recoil polarization P. With the proposed beam time, we expect similar statistical uncertainties in the proposed experiment for the differential cross section in the lowest Q^2 bin.

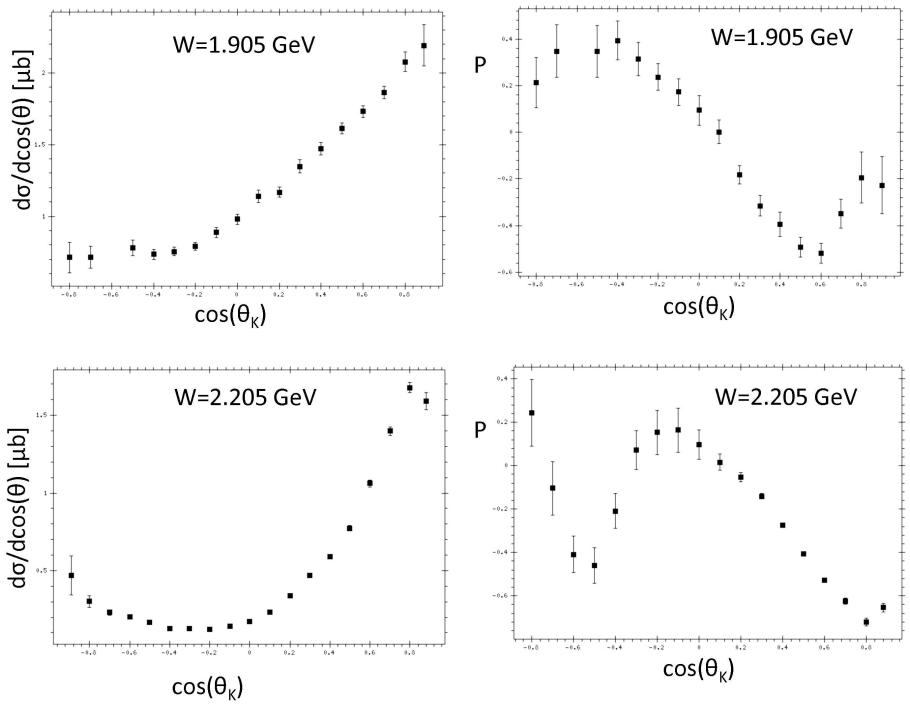

Figure 48: (Left) Differential cross sections and (Right) Λ recoil polarization for two W values covering the mass range from 1.85 GeV to 2.2 GeV, where seven of the newly discovered excited nucleon resonances have been discovered in the Bonn-Gatchina partial wave analysis [35, 36, 37], using the $K^+\Lambda$ data of the CLAS Collaboration [81] (see Fig. 9 in Section 3.3.

We want to emphasize that for the physics analysis we want to take full advantage of the particular feature of electron scattering that the differential cross section contains information on the linear photon beam polarization response function σ_{TT} in Eq.(28), as well as on the

longitudinal-transverse interference term σ_{LT} and the circular beam polarization interference term $\sigma_{LT'}$ (not shown in Eq.(28)). In the proposed electroproduction experiments, the differential cross section will be measured with similar precision as the photoproduction cross section. The simulations shown in Section 5 for the $\pi^+\pi^- p$ final state and in Section 6 for the K^+Y final state, as well as the minimal hybrid baryon electrocoupling studies in Section 7, have been carried out assuming beam times of 30 PAC days for each of the two beam energies, E_b=6.6 GeV and 8.8 GeV. What has, however, not been taken into account in these simulations is the need to separate the three structure functions, σ_U, σ_{LT}, and σ_{TT}, in the differential cross section by a fit to the azimuthal angle dependence $cos\phi$ and $\cos 2\phi$ and the ϕ-independent part of the cross section (see Fig. 38). This will allow for the use of the amplitude interference information in the resonance analysis. Moreover, we have used an oversimplified model with only one unknown baryon resonance included. It is more likely that more than one new resonance will contribute with different J^P and isospin quantum numbers.

An unambiguous analysis with more than one unknown resonance included will require higher statistics to disentangle the different quantum numbers from their interference. For two overlapping and interfering resonances we would have to separate both partial waves and their respective electrocouplings. In order to achieve this with the same sensitivity to their electrocouplings, we expect approximately a factor of two higher statistics will be needed. We therefore ask for 50 days of beam time at 6.6 GeV and 50 days of beam time at 8.8 GeV, both with fully polarized electrons.

The complete hybrid baryon program will require two beam energies, E_b=6.6 GeV and 8.8 GeV, to cover with high statistics the lowest Q^2 range, where the scattered electron is detected in the angle range from $2.5^\circ \leq \theta_e \leq 4.5^\circ$. The optimal run conditions require the torus current to be set at the maximum current with negative polarity, $I = -3375$ A, to maximize the kinematical coverage in the Q^2 vs. W kinematic plane while providing for the highest resolution reconstruction of the final state hadrons. We request new beam time of 100 days that are divided into 50 days at E_b=6.6 GeV and 50 days at E_b=8.8 GeV.

We have shown that the requested beam time would guarantee measurements of the four-fold differential cross sections $\frac{d^4\sigma}{dQ^2 dW d\Omega_K^*}$ of the KY electroprodution reactions, with statistical uncertainties of a few percent. With the same required beam time we have estimated that the minimum detectable electrocoupling strengths of candidate hybrid baryon resonances are of the order of $\approx 20(10^{-3})$ GeV$^{-1/2}$, which is compatible with those for the known higher mass N^* resonances [1]. We will also be able to obtain nine one-fold differential $\pi^+\pi^- p$ electroproduction cross sections with statistics sufficient for observation of a new state with electrocoupling values $\approx 40(10^{-3})$ GeV$^{-1/2}$, which is compatible with the value of the electrocoupling for the candidate baryon state $N'(1720)$ observed in the combined studies of the CLAS $\pi^+\pi^- p$ photo- and electroproduction data [33].

9 Summary

In this proposal we have laid out an extensive program to study the excitation of nucleon resonances in meson electroproduction using electron beam energies of 6.6 GeV and 8.8 GeV. The main focus is on the search for gluonic light-quark baryons in the mass range up to 3 GeV and in the Q^2 range from 0.05 GeV^2 to 2.0 GeV^2. We have estimated the rates for two of

the channels we propose to study, $K^+\Lambda$ ($K^+\Sigma^0$) and $p\pi^+\pi^-$, but all other channels detected in CLAS12 will be subjected to analysis as well. The expected rates are high, thanks to the very forward scattered electrons with a minimum Q^2 of 0.05 GeV^2 that are detected in the Forward Tagger. The data will be subjected to state-of-the-art partial wave analyses that were developed during the past few years for baryon resonance analyses, and have resulted in about 10 new excited baryon states that are now included in the latest edition of the Review of Particle Properties (PDG2014). Beyond the main focus of this proposal on hybrid baryons, a wealth of data will be collected in many different channels that will put meson electroproduction data on par with real photoproduction in terms of production rates and will allow for a vast extension of the ongoing N^* electroexcitation program with CLAS at lower energies. It will also complement the already approved program in Run Group A to study nucleon resonances at the highest Q^2 achievable at 11 GeV beam energy with CLAS12.

A Appendix A - KY Electroproduction

In the electroproduction of KY on the proton a beam of incoming electrons of energy E_e impinges on a fixed proton target of mass M_p, the scattered electrons emerging with energy $E_{e'}$ are detected at the the direction identified by the angles $(\theta_{e'}, \phi_{e'})$ and the kaons produced with momentum $\tilde{p_k} = (E_k, \vec{p_k})$ are measured. The cross section is five-fold differential in the scattered electron energy and direction $dE_{e'}d\Omega_{e'}$ and kaon direction $d\Omega_K$. In the one photon exchange approximation, a virtual photon of momentum $\tilde{q} = \tilde{p_e} - \tilde{p_{e'}} = (\nu, \vec{q})$, is emitted by the scattered electron and absorbed by the proton. The cross section can be expressed by the product of an equivalent flux of virtual photons Γ and the virtual photoproduction of the KY final state as:

$$\frac{d^5\sigma}{dE_{e'}d\Omega_{e'}d\Omega_K} = \Gamma\frac{d^2\sigma}{d\Omega_K^*} \tag{23}$$

where the virtual photoabsorption cross section is expressed in the γ^*p or KY CM reference frame and the photon flux Γ is given by the relation:

$$\Gamma = \frac{\alpha}{2\pi^2}\frac{E_{e'}}{E_e}\frac{W^2 - m_p^2}{Q^2}\frac{1}{1-\epsilon} \tag{24}$$

and depends on the electron scattering process only, in terms of the variables $Q^2 = -\tilde{q^2}$, the photon virtuality, $W = \sqrt{M_p^2 + 2M_p\nu - Q^2}$, the total energy in the γ^*p CM reference frame, and the virtual photon polarization ϵ:

$$\epsilon = \frac{4E_eE_{e'} - Q^2}{2(E_e^2 + E_{e'}^2) + Q^2}. \tag{25}$$

The kinematics of the process is shown in Fig. 49.

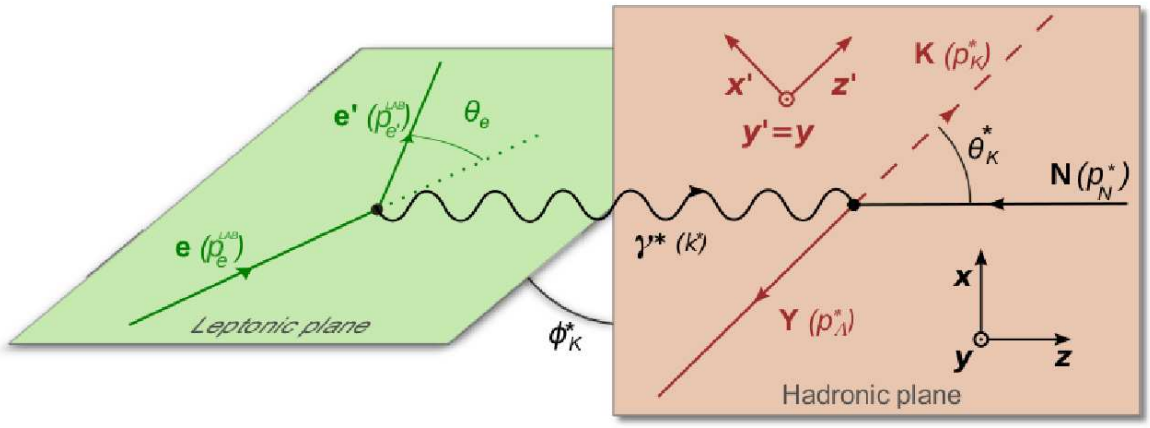

Figure 49: Kinematics of KY electroproduction. The quantities in the leptonic plane are expressed in the laboratory frame. The quantities in the hadronic plane are expressed in the CM frame of the γ^*p or KY system.

After integrating over the azimuthal angle of the scattered electron, the photoabsorption cross section can be expressed in terms of the variables Q^2, W, and the kaon scattering angle in the KY CM frame θ_K^* and the angle between the leptonic and hadronic plane ϕ_K^*. Introducing the appropriate Jacobian, the form of the cross section may be rewritten as:

$$\frac{d^4\sigma}{2\pi dW dQ^2 d\Omega_K^*} = \Gamma_v \frac{d^2\sigma_v}{d\Omega_K^*} \tag{26}$$

where

$$\Gamma_v = \frac{\alpha}{4\pi}\frac{W}{E^2}\frac{W^2 - m_P^2}{Q^2(1-\epsilon)}\frac{1}{m_P^2} \tag{27}$$

is the corresponding flux of virtual photons.

For the case of an unpolarized electron beam, with no target or recoil polarizations, the virtual photon absorption cross section can be written as:

$$\frac{d^2\sigma}{d\Omega_K^*} = \frac{d^2\sigma_T}{d\Omega_K^*} + \epsilon\frac{d^2\sigma_L}{d\Omega_K^*} + \epsilon\frac{d^2\sigma_{TT}}{d\Omega_K^*}\cos 2\phi_K^* + \sqrt{\epsilon(1+\epsilon)}\frac{d^2\sigma_{LT}}{d^2\Omega_K^*}\cos\phi_K^*. \tag{28}$$

where the $\frac{d^2\sigma_i}{d\Omega_K^*}$ are the structure functions that measure the response of the hadronic system. $i = T,\ L,\ TT$, and LT represent the transverse, longitudinal, and interference structure functions and depend on the variables W, Q^2 and θ_K^* only.

In the formalism used in the Ghent model [12], the cross section may be related to the reaction amplitude as:

$$M_{\lambda_\gamma}^{\lambda_p\lambda_f} = \langle \lambda_f \left| T_r \right| \lambda_\gamma \lambda_p \rangle \tag{29}$$

in term of the nine helicity dependent bilinear functions:

$$H_{\lambda\lambda'} = \sum_{\lambda_N\lambda_Y} M_\lambda^{'\lambda_N\lambda_Y}(M_\lambda^{'\lambda_N\lambda_Y})^\dagger \tag{30}$$

where λ and λ' assume all possible values of the virtual photon helicity, $0, \pm 1$.

The transverse, longitudinal, and interference structure functions are defined as:

$$\begin{aligned}
\frac{d^2\sigma_L}{d\Omega_K^*} &= 2\chi\frac{1}{(4\pi)^2}H_{0,0} \\
\frac{d^2\sigma_T}{d\Omega_K^*} &= \chi\frac{1}{(4\pi)^2}(H_{1,1} + H_{-1,-1}) \\
\frac{d^2\sigma_{TT}}{d\Omega_K^*} &= -\chi\frac{1}{(4\pi)^2}(H_{1,-1} + H_{-1,1}) \\
\frac{d^2\sigma_{LT}}{d\Omega_K^*} &= -\chi\frac{1}{(4\pi)^2}(H_{0,1} + H_{1,0} - H_{-1,0} - H_{0,-1})
\end{aligned} \tag{31}$$

where the normalization factor χ assumes the form:

$$\chi = \frac{1}{16Wm_P}\frac{\sqrt{W^4 + (m_K^2 - m_\Lambda^2)^2 - 2W^2(m_K^2 + m_\Lambda^2)}}{2W}\frac{2m_P}{W^2 - m_P^2}. \tag{32}$$

The hybrid resonance amplitudes $M_{\lambda}^{\lambda_N \lambda_Y}$ described in Appendix B and reported in Tables 8 and 9 for spin $\frac{1}{2}$ and $\frac{3}{2}$ resonances, respectively, have been added to the $M_{\lambda}^{\lambda_N \lambda_Y}$ reaction amplitudes from Ref. [12] (KY model A) to form a set of total amplitudes:

$$M_{\lambda}^{\lambda_N \lambda_Y} = M_{\lambda}^{\lambda_N \lambda_Y} + M_{\lambda}^{\lambda_N \lambda_Y}. \tag{33}$$

The resulting calculated cross sections from Eq.(31) have been used as the KY Model B to study the sensitivity of the proposed experiment to the hybrid baryons electrocouplings.

B Appendix B - Hybrid Baryon Excitation Amplitudes

The excitation of a single hybrid resonance in the helicity representation $\langle \lambda_f \left| T_r \right| \lambda_\gamma \lambda_p \rangle$ may be expressed using a relativistic Breit-Wigner (BW) ansatz:

$$M_{\lambda_\gamma}^{\lambda_p \lambda_f} = \langle \lambda_f \left| T_r \right| \lambda_\gamma \lambda_p \rangle = \frac{\langle \lambda_f \left| T_{dec} \right| \lambda_R \rangle \langle \lambda_R \left| T_{em} \right| \lambda_\gamma \lambda_p \rangle}{M_r^2 - W^2 - i \Gamma_r M_r}, \tag{34}$$

where M_r and Γ_r are the resonance mass and total width, respectively; we have assumed both the total and partial decay widths are energy independent.

The matrix elements $\langle \lambda_R \left| T_{em} \right| \lambda_\gamma \lambda_p \rangle$ and $\langle \lambda_f \left| T_{dec} \right| \lambda_R \rangle$ are the electromagnetic production and hadronic decay amplitudes, respectively, of the N^* with helicity $\lambda_R = \lambda_\gamma - \lambda_p$, in which λ_γ and λ_p are the helicities of the photon and proton in the initial state, respectively, and λ_f is the helicity of final-state hadron in the N^* decay.

In the case of the KY final state, the hadronic decay amplitudes $\langle \lambda_f | T_{dec} | \lambda_R \rangle$ are related to the Γ_{λ_f} partial hadronic decay widths of the N^* to the KY final states f of helicity $\lambda_f = \lambda_Y$ by:

$$\langle \lambda_f | T_{dec} | \lambda_R \rangle = \langle \lambda_f | T_{dec}^{J_r} | \lambda_R \rangle d_{\mu\nu}^{J_r}(\cos\theta_K) e^{i\mu\phi_K}, \tag{35}$$

with $\mu = \lambda_R$ and $\nu = -\lambda_Y$, and

$$\langle \lambda_f | T_{dec}^{J_r} | \lambda_R \rangle = \frac{2\sqrt{2\pi}\sqrt{2J_r+1} M_r \sqrt{\Gamma_{\lambda_f}}}{\sqrt{p_i^r}} \sqrt{\frac{p^r}{p}}. \tag{36}$$

Here p^r and p are the magnitudes of the three-momenta of the final state K for the $N^* \to KY$ decay evaluated at $W = M_r$ and at the running W, respectively. The variables θ_K, ϕ_K are the CM frame polar and azimuthal angles for the final kaon, and J_r is the N^* spin.

The final state Λ or Σ^0 baryons can only be in the helicity states $\lambda_f = \pm\frac{1}{2}$. The hadronic decay amplitudes $\langle \lambda_f | T_{dec}^{J_r} | \lambda_R \rangle$ with $\lambda_f = \pm\frac{1}{2}$ are related by P-invariance, which requires that the absolute values for both amplitudes are the same. Therefore, the hybrid state partial decay widths to the $K^+\Lambda$ and $K^+\Sigma^0$ final states Γ_{λ_f} can be estimated as:

$$\Gamma_{\lambda_f} = \frac{1}{2}\Gamma_r 0.03, \tag{37}$$

where the factor of 0.03 reflects the adopted 3% branching ratio for hybrid baryon decays to the KY final state.

The following relationships between the transition amplitudes $\langle \lambda_R \left| T_{em} \right| \lambda_\gamma \lambda_p \rangle$ and the $\gamma_v N N^*$ electrocouplings from Ref. [13] have been used:

$$\langle \lambda_R |\, T_{em}\, | \lambda_\gamma \lambda_p \rangle = \frac{W}{M_r} \sqrt{\frac{8 M_N M_r q_{\gamma_r}}{4\pi\alpha}} \sqrt{\frac{q_{\gamma_r}}{q_\gamma}} A_{1/2,3/2}(Q^2), \tag{38}$$

with

$$|\lambda_\gamma - \lambda_p| = \frac{1}{2}, \frac{3}{2} \tag{39}$$

for transverse photons and

$$\langle \lambda_R |\, T_{em}\, | \lambda_\gamma \lambda_p \rangle = \frac{W}{M_r} \sqrt{\frac{16 M_N M_r q_{\gamma_r}}{4\pi\alpha}} \sqrt{\frac{q_{\gamma_r}}{q_\gamma}} S_{1/2}(Q^2), \tag{40}$$

for longitudinal photons. Here q_γ is the absolute value of the initial photon three-momentum of virtuality $Q^2 > 0$ with $q_\gamma = \sqrt{Q^2 + E_\gamma^2}$ and E_γ the photon energy in the CM frame at the running W, with

$$E_\gamma = \frac{W^2 - Q^2 - M_N^2}{2W}. \tag{41}$$

The $q_{\gamma,r}$ value is then computed from Eq.(41) with $W = M_r$.

We have investigated the effect of adding contributions to the KY and $\pi^+\pi^- p$ reaction amplitudes from hybrid baryon states with spin-parities $J^P = \frac{1}{2}^+$ and $\frac{3}{2}^+$. Electroexcitation of the former state can be described by two electrocouplings $A_{1/2}$ and $S_{1/2}$, while the latter should be described by three electrocouplings, $A_{1/2}$, $S_{1/2}$, and $A_{3/2}$. Information on the expected Q^2 evolution of the aforementioned electrocouplings for hybrid states is, to the best of our knowledge, currently not available. Therefore we have varied the hybrid baryon electrocouplings to determine their minimal absolute values above which the signal from the hybrid baryon can be observed, in the difference between the angular distributions with and without the hybrid baryon contributions. These studies have independently been done at fixed values of Q^2, for different bins in the range proposed by this proposal. It may be noted that, in the very high Q^2 regime, the following relations for the hybrid baryon electrocouplings have been used in literature [23] to model the hybrid baryon signatures:

$$A_{1/2} = A, \quad S_{1/2} = AQ, \quad A_{3/2} = A/Q^2, \tag{42}$$

where $Q = \sqrt{Q^2}$ and A is a common term. However, in the low Q^2 regime, these relations are not valid and we have considered fixed independent values for all three electrocouplings.

Substituting Eq.(35) and Eq.(40) in Eq.(34), one obtains:

$$M_{\lambda_\gamma}^{\lambda_p \lambda_f} = \langle \lambda_f |\, T_r\, | \lambda_\gamma \lambda_p \rangle = \frac{\langle \lambda_f |\, T_{dec}\, | \lambda_\gamma \lambda_R \rangle \langle \lambda_R |\, T_{em}\, | \lambda_\gamma \lambda_p \rangle}{M_r^2 - W^2 - i\Gamma_r M_r} \tag{43}$$

$$= \frac{\langle \lambda_f |\, T_{dec}^{J_r}\, | \lambda_R \rangle}{M_r^2 - W^2 - i\Gamma_r M_r} d^{J_r}_{\mu\nu}(\cos\theta_K^*) e^{i\mu\phi_K^*} \frac{W}{M_r} \sqrt{\frac{c M_N M_r q_{\gamma_r}}{4\pi\alpha}} \sqrt{\frac{q_{\gamma_r}}{q_\gamma}}, \tag{44}$$

with $A_{1/2,3/2}(Q^2)$, $c = 8$ and $S_{1/2}(Q^2)$, $c = 16$. Substituting also Eq.(36), the following expression is obtained:

$$M_{\lambda_\gamma}^{\lambda_p\lambda_f} = \frac{2\sqrt{2\pi}\sqrt{2J_r+1}M_r\sqrt{\Gamma_{\lambda_f}}}{M_r^2 - W^2 - i\Gamma_r M_r} d_{\mu\nu}^{J_r}(\cos\theta_K^*) e^{i\mu\phi_K^*} \frac{W}{M_r\sqrt{p_i}} \sqrt{\frac{cM_N M_r q_{\gamma_r}}{4\pi\alpha}} \sqrt{\frac{q_{\gamma_r}}{q_\gamma}}, \tag{45}$$

with $A_{1/2,3/2}(Q^2),\ c = 8$ and $S_{1/2}(Q^2),\ c = 16$.

At this point it is possible to express $M_{\lambda_\gamma}^{\lambda_p\lambda_Y}$ in terms of a factor that doesn't depend on the λ_p, λ_Y, and λ_γ helicities:

$$F_{J_r} = \frac{2\sqrt{2\pi}\sqrt{2J_r+1}M_r\sqrt{\Gamma_{\lambda_f}}}{M_r^2 - W^2 - i\Gamma_r M_r} \frac{W}{M_r\sqrt{p_i}} \sqrt{\frac{cM_N M_r q_{\gamma_r}}{4\pi\alpha}} \sqrt{\frac{q_{\gamma_r}}{q_\gamma}}, \tag{46}$$

with $A_{1/2}(Q^2) = A,\ c = 8$ and $S_{1/2}(Q^2) = AQ,\ c = 16$, which is multiplied by the terms that introduce the angular dependence upon the K angles in the CM frame:

$$M_{\lambda_\gamma}^{\lambda_p\lambda_f} = \langle\lambda_f|\, T_r\, |\lambda_\gamma\lambda_p\rangle = F_{J_r} d_{\mu\nu}^{J_r}(cos\theta_K^*) e^{i\mu\phi_K^*}, \tag{47}$$

with $\mu = \lambda_R$ and $\nu = -\lambda_Y$. In the formalism used by the Ghent RPR-2011 model [12], the expressions F_{J_r} must be multiplied by a factor $\sqrt{4\pi\alpha}$.

The $d_{\mu\nu}^{J_r}(\cos\theta_K^*)$ coefficients are the Wigner rotation matrix elements, for which the relationship $d_{m',m}^J = (-1)^{m-m'} d_{m,m'}^J = d_{-m,-m'}^J$ is valid. For $J = \frac{1}{2}$ they present the following explicit form:

$$\begin{aligned}
d_{1/2\ 1/2}^{1/2}(\cos\theta_K^*) &= \cos\theta_K^*/2 \\
d_{1/2\ -1/2}^{1/2}(\cos\theta_K^*) &= -\sin\theta_K^*/2 \\
d_{-1/2\ -1/2}^{1/2}(\cos\theta_K^*) &= d_{1/2\ 1/2}^{1/2}(\cos\theta_K^*) = \cos\theta_K^*/2 \\
-d_{-1/2\ 1/2}^{1/2}(\cos\theta_K^*) &= d_{1/2\ -1/2}^{1/2}(\cos\theta_K^*) = -\sin\theta_K^*/2,
\end{aligned} \tag{48}$$

while for $J = \frac{3}{2}$ one has:

$$\begin{aligned}
d_{3/2\ 3/2}^{3/2}(\cos\theta_K^*) &= \frac{1+\cos\theta_K^*}{2}\cos\theta_K^*/2 = d_{-3/2\ -3/2}^{3/2}(\cos\theta_K^*) \\
d_{3/2\ 1/2}^{3/2}(\cos\theta_K^*) &= -\sqrt{3}\frac{1+\cos\theta_K^*}{2}\sin\theta_K^*/2 = -d_{-3/2\ -1/2}^{3/2}(\cos\theta_K^*) \\
d_{3/2\ -1/2}^{3/2}(\cos\theta_K^*) &= \sqrt{3}\frac{1-\cos\theta_K^*}{2}\cos\theta_K^*/2 = (-1)^{-3/2-1/2} d_{-3/2\ 1/2}^{3/2}(\cos\theta_K^*) \\
&= d_{-3/2\ 1/2}^{3/2}(\cos\theta_K^*) \\
d_{3/2\ -3/2}^{3/2}(\cos\theta_K^*) &= -\frac{1-\cos\theta_K^*}{2}\sin\theta_K^*/2 \\
d_{1/2\ 1/2}^{3/2}(\cos\theta_K^*) &= \frac{3\cos\theta_K^*-1}{2}\cos\theta_K^*/2 = d_{-1/2\ -1/2}^{3/2}(\cos\theta_K^*) \\
d_{1/2\ -1/2}^{3/2}(\cos\theta_K^*) &= -\frac{3\cos\theta_K^*+1}{2}\sin\theta_K^*/2 = -d_{-1/2\ 1/2}^{3/2}(\cos\theta_K^*)
\end{aligned} \tag{49}$$

The final expressions for the hybrid baryon excitation amplitudes $M_{\lambda_\gamma}^{\lambda_p \lambda_f}$, are given in Table 8 and Table 9, for $J = \frac{1}{2}$ and $J = \frac{3}{2}$, respectively. No explicit dependence on the ϕ_K angle is introduced.

λ_γ	$\lambda_p = 1/2$ $\lambda_Y = 1/2$	$\lambda_p = 1/2$ $\lambda_Y = -1/2$	$\lambda_p = -1/2$ $\lambda_Y = 1/2$	$\lambda_p = -1/2$ $\lambda_Y = -1/2$
1	$F_{1/2}A_{1/2}(-\sin\theta_K^*/2)$	$F_{1/2}A_{1/2}(\cos\theta_K^*/2)$	0	0
0	$F_{1/2}S_{1/2}(\cos\theta_K^*/2)$	$F_{1/2}S_{1/2}(\sin\theta_K^*/2)$	$F_{1/2}S_{1/2}(-\sin\theta_K^*/2)$	$F_{1/2}S_{1/2}(\cos\theta_K^*/2)$
-1	0	0	$F_{1/2}A_{1/2}(\cos\theta_K^*/2)$	$F_{1/2}A_{1/2}(\sin\theta_K^*/2)$

Table 8: Expressions for $M_{\lambda_\gamma}^{\lambda_p \lambda_Y}$ for $J^P = \frac{1}{2}^+$ for all possible values of λ_P, λ_Y, and λ_γ. The Wigner rotation matrix elements have been inserted.

λ_γ	$\lambda_p = 1/2$ $\lambda_Y = 1/2$	$\lambda_p = 1/2$ $\lambda_Y = -1/2$	$\lambda_p = -1/2$ $\lambda_Y = 1/2$	$\lambda_p = -1/2$ $\lambda_Y = -1/2$
1	$F_{3/2}A_{1/2}d^{3/2}_{1/2\ -1/2}$	$F_{3/2}A_{1/2}d^{3/2}_{1/2\ 1/2}$	$F_{3/2}A_{3/2}d^{3/2}_{3/2\ -1/2}$	$F_{3/2}A_{3/2}d^{3/2}_{3/2\ 1/2}$
0	$F_{3/2}S_{1/2}d^{3/2}_{-1/2\ -1/2}$	$F_{3/2}S_{1/2}d^{3/2}_{-1/2\ 1/2}$	$F_{3/2}S_{1/2}d^{3/2}_{1/2\ -1/2}$	$F_{3/2}S_{1/2}d^{3/2}_{1/2\ 1/2}$
-1	$F_{3/2}A_{3/2}d^{3/2}_{-3/2\ -1/2}$	$F_{3/2}A_{3/2}d^{3/2}_{-3/2\ 1/2}$	$F_{3/2}A_{1/2}d^{3/2}_{-1/2\ -1/2}$	$F_{3/2}A_{1/2}d^{3/2}_{-1/2\ 1/2}$

Table 9: Values of $M_{\lambda_\gamma}^{\lambda_p \lambda_Y}$ for $J^P = \frac{3}{2}^+$ for all the possible values of λ_P, λ_Y, and λ_γ. Note that now the terms with $\mu = 3/2$ are non-zero.

References

[1] K.A. Olive *et al.* [Particle Data Group Collaboration], Chin. Phys. C **38**, 090001 (2014)

[2] I.G. Aznauryan *et al.* [CLAS Collaboration], Phys. Rev. C **78**, 045209 (2008).

[3] T. Barnes and F.E. Close, Phys. Lett. B **123**, 89 (1983); E. Golowich, E. Haqq, and G. Karl, Phys. Rev. D **28**, 160 (1983);C.E. Carlson and T.H. Hansson, Phys. Lett. B **128**, 95 (1983); I. Duck and E. Umland, Phys.Lett. B **128** (1983) 221.

[4] I.G. Aznauryan and V.D. Burkert, Prog. Part. Nucl. Phys. **67**, 1 (2012).

[5] I.G. Aznauryan *et al.* [CLAS Collaboration], Phys. Rev. C **80**, 055203 (2009).

[6] J.J. Dudek and R.G. Edwards, Phys. Rev. D **85**, 054016 (2012).

[7] I.G. Aznauryan *et al.*, Int. J. Mod. Phys. E **22**, 1330015 (2013).

[8] V.I. Mokeev and I.G. Aznauryan, Int. J. Mod. Phys. Conf. Ser. **26**, 1460080 (2014).

[9] V.I. Mokeev, Presentation at the ECT* Workshop, *Nucleon Resonances: From Photoproduction to High Photon Virtualities*, (2015), http:/boson.physics.sc.edu gothe/ect*-15program.html

[10] V.I. Mokeev *et al.*, Phys. Rev. C **93**, 025206 (2016).

[11] V.I. Mokeev *et al.*, Phys. Rev. C **80**, 045212 (2009).

[12] L. De Cruz, J. Ryckebusch, T. Vrancx and P. Vancraeyveld, Phys. Rev. C **86**, 015212 (2012).

[13] V.I. Mokeev *et al.* [CLAS Collaboration], Phys. Rev. C **86**, 035203 (2012)

[14] A. Anisovich *et al.*, Eur. Phys. J. A **48**, 15 (2012).

[15] D. Ronchen *et al.*, Eur. Phys. J. A **50**, 101 (2014).

[16] A.P. Szczepaniak and M.R. Pennington, Phys. Lett. B **737**, 283 (2014).

[17] See http://pdg.lbl.gov/2015/reviews/rpp2015-rev-n-delta-resonances.pdf

[18] JLab Experiment E12-09-003, spokespersons: V.D. Burkert, P. Cole, R. Gothe, K. Joo, V. Mokeev, P. Stoler

[19] JLab Experiment E12-06-108A, spokespersons: D.S. Carman, R. Gothe, V. Mokeev

[20] S. Capstick and P.R. Page, Phys. Rev. C **66**, 065204 (2002); Phys. Rev. D **60**, 111501 (1999).

[21] P.R. Page, Int. J. Mod. Phys. A **20**, 1791 (2005).

[22] C.K. Chow, D. Pirjol and T.M. Yan, Phys. Rev. D **59**, 056002 (1999).

[23] C.E. Carlson and N.C. Mukhopadhyay, Phys. Rev. Lett. **67**, 3745 (1991).

[24] T.T. Takahashi and H. Suganuma, Phys. Rev. Lett. **90**, 182001 (2003).

[25] E. Kou, Phys. Rev. D **63**, 054027 (2001).

[26] I.V. Anikin, V. M. Braun, and N. Offen, Phys. Rev. D **92**, 074044 (2015).

[27] J. Segovia, B. El-Bennich, E. Rojas *et al.*, Phys. Rev. Lett. **115**, 015203 (2015).

[28] V.I. Mokeev *et al.*, Phys. Rev. C **93**, 054016 (2016).

[29] Z.P. Li, Phys. Rev. D **44**, 2841 (1991).

[30] Z.P. Li, V. Burkert and Z.J. Li, Phys. Rev. D **46**, 70 (1992).

[31] S.J. Brodsky and G.R. Farrar, Phys. Rev. Lett. **31**, 1153 (1973); Phys. Rev. D **11**, 1309 (1975); V.A. Matveev, R.M. Muradyan, and A.V. Tavkhelidze, Lett. Nuovo Cimento **7**, 719 (1978).

[32] M. Dugger *et al.*, [CLAS Collaboration], Phys. Rev. C **79**, 065206 (2009).

[33] V.I. Mokeev *et al.*, Eur. Phys. J. Web Conf. **113**, 01013 (2016).

[34] M. Ripani *et al.*, Nucl. Phys. A **672**, 220 (2000).

[35] A.V. Anisovich *et al.*, Eur. Phys. J. A **48**, 15 (2012).

[36] A.V. Anisovich *et al.*, Eur. Phys. J. A **48**, 88 (2012).

[37] A.V. Anisovich *et al.*, Eur. Phys. J. A **49**, 158 (2013).

[38] J.W.C. McNabb *et al.* [CLAS Collaboration], Phys. Rev. C **69**, 042201 (2004).

[39] R. Bradford *et al.* [CLAS Collaboration], Phys. Rev. C **73**, 035202 (2006).

[40] R. Bradford *et al.* [CLAS Collaboration], Phys. Rev. C **75**, 035205 (2007).

[41] M.E. McCracken *et al.* [CLAS Collaboration], Phys. Rev. C **81**, 025201 (2010).

[42] K.H. Glander *et al.* [SAPHIR Collaboration], Eur. Phys. J. A **19**, 251 (2004).

[43] T.C. Jude *et al.* [Crystal Ball Collaboration], Phys. Lett. B **735**, 035205 (2014).

[44] A. Lleres *et al.* [GRAAL Collaboration], Eur. Phys. J. A **31**, 79 (2007).

[45] A. Lleres *et al.* [GRAAL Collaboration], Eur. Phys. J. A **39**, 149 (2009).

[46] M. Ablikim *et al.* [BESIII Collaboration], Phys. Rev. Lett. **110**, 022001 (2013).

[47] M. Ripani *et al.* [CLAS Collaboration], Phys. Rev. Lett. **91**, 022002 (2003)

[48] K. Park *et al.* [CLAS Collaboration], Phys. Rev. C **91**, 045203 (2015).

[49] E. Golovach *et al.*, $\gamma p \to p\pi^+\pi^-$ cross sections from g11a experiment, CLAS Analysis Note (in preparation), (2016).

[50] C.D. Roberts, J. Phys. Conf. Ser. **630**, 012051 (2015).

[51] C.D. Roberts and J. Segovia, arXiv:1603.02722 [nucl-th].

[52] A. Sarantsev, Presentation at the ECT* Workshop, *Nucleon Resonances: From Photoproduction to High Photon Virtualities*, (2015), http:/boson.physics.sc.edu gothe/ect*-15program.html

[53] H. Kamano, T-S. H. Lee, AIP Conf. Proc. **1432**, 74 (2012).

[54] H. Kamano, S. X. Nakamura, T-S. H. Lee, T. Sato, Phys. Rev. C **88**, 035209 (2013).

[55] N. Suzuki, T. Sato, and T-S. H. Lee, Phys. Rev. C **82**, 045206 (2010).

[56] G.V. Fedotov *et al.* [CLAS Collaboration], Phys. Rev. C **79**, 015204 (2009)

[57] Jefferson Laboratory Joint Physics Analysis Center, https://jpac.jlab.org/.

[58] T. Corthals, D.G. Ireland, T. Van Cauteren and J. Ryckebusch, Phys. Rev. C **75**, 045204 (2007).

[59] D.S. Carman *et al.* [CLAS Collaboration], Phys. Rev. Lett. **90**, 131804 (2003).

[60] D.S. Carman *et al.* [CLAS Collaboration], Phys. Rev. C **79**, 065205 (2009).

[61] M. Gabrielyan *et al.* [CLAS Collaboration], Phys. Rev. C **90**, 035202 (2014).

[62] P. Ambrozewicz *et al.* [CLAS Collaboration], Phys. Rev. C **75**, 045203 (2007).

[63] R. Nasseripour *et al.* [CLAS Collaboration], Phys. Rev. C **77**, 065208 (2008).

[64] D.S. Carman *et al.* [CLAS Collaboration], Phys. Rev. C **87**, 025204 (2013).

[65] B.A. Raue and D.S. Carman, Phys. Rev. C **71**, 065209 (2005).

[66] J. Nys, Presentation at the ECT* Workshop, *Nucleon Resonances: From Photoproduction to High Photon Virtualities*, (2015), http:/boson.physics.sc.edu gothe/ect*-15program.html

[67] For details see: https://www.jlab.org/Hall-B/clas12-web/

[68] V.I. Mokeev *et al.*, in "Proc. of the Workshop on the Physics of Excited Nucleon. NSTAR2005", ed. by S. Capstick, V. Crede, P. Eugenio, World Scientific Publishing Co., p. 47.

[69] I.G. Aznauryan, V.D. Burkert, G.V. Fedotov, B.S. Ishkhanov, and V.I. Mokeev, Phys. Rev. C **72**, 045201 (2005).

[70] C. Wu *et al.*, Eur. Phys. J. A **23**, 317 (2005).

[71] [Aachen-Berlin-Bonn-Hamburg-Heidelberg-Munich Collaboration], Phys. Rev. **175**, 1669 (1968).

[72] L.W. Mo and Y.S. Tsai, Mod. Phys. **41**, 205 (1969).

[73] GEMC Documentation,
see https://gemc.jlab.org/gemc/Documentation/Documentation.html

[74] CLAS12 Software Development,
see http://clasweb.jlab.org/clas12offline/docs/software/html/

[75] A. Afanasev, I. Akushevich, V. Burkert, and K. Joo, Phys. Rev. D **66**, 074004 (2002).

[76] T. Vrancx, J. Ryckebusch, and J. Nys, Phys. Rev. C **89**, no. 6, 065202 (2014)

[77] StrangeCalc website: http://rprmodel.ugent.be/calc/

[78] D. Luke and P. Soding, Multiple Pion Photoproduction in the s Channel Resonance Region, Springer Tracts in Modern Physics **59**, (1971).

[79] A.V. Anisovich *et al.*, Phys. Lett. B **711**, 162 (2012).

[80] A.V. Anisovich *et al.*, Eur. Phys. J. A **50**, 129 (2014).

[81] M.E. McCracken *et al.* [CLAS Collaboration], Phys. Rev. C **81**, 025201 (2010).